Understanding How Tape Casting Titanium Diboride Shifts its Processing-Microstructure-Properties Paradigm Toward New Applications

Kaitlyn Shirey

Dissertation submitted to the faculty of the Virginia Polytechnic Institute and State University in partial fulfillment of the requirements for the degree of

Doctor of Philosophy

In

Materials Science and Engineering

Carolina Tallon, Chair

Guo-Quan Lu

Amanda Morris

Rui Qiao

May 26, 2023

Blacksburg, VA

Keywords: colloidal processing, tape casting, ultra-high temperature ceramics, microstructure, porosity, alignment

Understanding How Tape Casting Titanium Diboride Shifts its Processing-Microstructure-Properties Paradigm Toward New Applications

Kaitlyn Shirey

Academic Abstract

The manufacturing of UHTC materials has significantly advanced over recent years, allowing for the development of new microstructures, architectures, shapes, and geometries to explore new properties and applications for these materials beyond aerospace. One of the UHTCs, titanium diboride (TiB_2) exhibits high electrical and thermal conductivity that could satisfy the needs of functional ceramic component applications, like battery cathodes, by tailoring its microstructure and architecture. This thesis represents one of the first detailed studies to understand how the processing-microstructure-properties relationship of TiB_2 can be shifted to explore new applications. In order to do that, TiB_2 has been manufactured with a processing technique never used before, with significant porosity, exploration of which has been very limited for this material. Additionally, this thesis also explores the synthesis and utilization of novel anisotropic particles to further explore this material relationship.

In this work, aqueous tape casting of TiB_2 has been investigated. Zeta potential measurements and suspension rheology were used to understand the role of dispersant, binder and plasticizer in the suspension and their interaction with the surface chemistry of the TiB_2 particles to develop a stable, homogenous suspension, with minimum additive amounts (0-2 wt%). Homogeneous, flexible and strong TiB_2 tapes were prepared using suspensions with 30 vol% solids and characterized to compare different compositions, mixing methods, and thicknesses. The characterization shows the tailoring of the properties as a function of the controlled suspension formulation with minimum amount of additives. Green tapes with 2 wt% dispersant, 1 wt% binder, and 2 wt% plasticizer had similar microstructure to those with half the plasticizer but quintuple the Young's modulus (1.96 GPa). The effect on other relevant properties is also discussed.

Tape casting aligns anisotropic particles along the direction of casting, which can be taken advantage of for increasing fracture toughness directionally or producing aligned pore networks using sacrificial fillers. The relationship between alignment, porosity, and the mechanical properties of titanium diboride has not been studied. In this work, we characterize the porous sintered bodies produced through aqueous tape casting of non-spherical TiB_2 particles of aspect ratio close to 1, as well as composites with an added high aspect ratio particle (2 wt% PCN-222). Synthesis of uniform, spherical ZrC is difficult and generally not cost-effective, as is the case for most ultra-high temperature ceramics. High aspect ratio particles for reinforcement of ceramic

composites are even more difficult to synthesize. Metal organic frameworks (MOF) are crystalline coordination polymers composed of multidentate organic linkers bridging metal nodes to form porous structures. Thermal decomposition of MOFs presents a new and cost-effective route to synthesis of ZrC. In this study, heat treatment at 2000°C of MOF PCN-222 produces zirconium carbide (ZrC) within a highly anisotropic particle. The resulting rod-shaped, glass-like carbon matrix embedded with ZrC crystals is described. These rods have potential as reinforcements for high temperature applications and as a synthetic route for ultra-high temperature ceramics with unique morphologies. It is the first time that this type of transformation from a MOF into a UHTC has been reported.

We have determined through analysis of SEM images that regardless of tape casting speed, about 57% of the TiB_2 particles are aligned with the tape casting direction. The mechanical properties are dominated by the effects of the porosity (38%), but the alignment exhibited here could be further exploited for anisotropic behavior across the sintered tapes. Composites cast with high aspect ratio particles exhibited strong alignment in the casting direction. Further work is required to understand the interplay between alignment and porosity and their effects on material properties.

Understanding How Tape Casting Titanium Diboride Shifts its Processing-Microstructure-Properties Paradigm Toward New Applications

Kaitlyn Shirey

General Audience Abstract

Titanium diboride (TiB_2) is an ultra-high temperature ceramic with a melting point of 3225°C. Many applications for this material require fully dense structural ceramics, such as cutting tools,[1] armor,[2] and high temperature structural supports.[2,3] These applications rely mainly on the high mechanical strength of TiB_2, which is maintained in extreme thermal and chemical environments. The field of knowledge surrounding TiB_2 lacks information about the ways that porosity affects its otherwise well-known properties;[4,5] to bridge this gap could open up applications for functional and porous ceramics such as lithium-air batteries,[6] electrochemical components,[7] semiconductors,[8] and more. This work intends to provide a foundation for this endeavor by developing for the first time a colloidal suspension formulation that allows for the tape casting of TiB_2 and characterizing the resulting porous ceramics.

Among these new potential applications, many require thin ceramics less than 1 mm thick—a result which has been accomplished for other materials via tape casting.[4,9] This is a wet route of producing ceramics that provides the ability to tailor the surface chemistry of the particles, giving greater control over the stability of the suspension (TiB_2 particles suspended in water) and quality of the end product than is afforded by dry processing routes.[10] This also allows for more complex shaping than simple pressing, which ultimately saves costs; by producing the near-net shape in the green body before firing, less machining must be done to the sintered body when it is removed from the high temperature furnace.[11] In tape casting, the suspension is spread over a substrate by a doctor blade to the desired thickness. It is known that tape casting tends to align anisotropic particles along the direction of casting due to a nonuniform velocity imparted by the shear force of the doctor blade spreading the suspension, an advantage which can provide directional properties in the final ceramic.[9] While this process is well known, it has never been applied to the material TiB_2 prior to this work.

In this work, a suspension is formulated to allow for the tape casting of TiB_2 with minimum organic additive content, which is cost-effective and reduces potential for defects. Porosity and alignment in the tape cast specimens are characterized. For comparison, a highly anisotropic or rod-shaped particle (PCN-222, a metal organic framework material) was included in the TiB_2 suspensions for tape casting. This metal organic framework (MOF) has been transformed into a high temperature material after thermal treatment at the sintering temperature of 2000°C, showing that the resulting

particle is made of glass-like carbon embedded with zirconium carbide (ZrC) crystallites. This particle could be used as a reinforcement for ultra-high temperature ceramics, and in this work was shown to align strongly in the tape casting direction.

At the level of porosity (38%) and alignment (57%) in the TiB_2 specimens in this study, porosity dominates the mechanical properties. This relationship is shown to be more complicated than lowering the strength by the same proportion that the density is lowered, and various models for understanding the role of porosity on the elastic modulus are explored.

Dedication

For my parents.

Acknowledgements

Kaitlyn Shirey acknowledges funding for her graduate studies from the following sources: the Institute for Critical Technology and Applied Sciences Doctoral Fellowship, the Pratt Graduate Fellowship, and the Graduate and Professional Studies Office in the College of Engineering at Virginia Tech. Thank you to the Materials Science and Engineering Department for supporting this research.

This work used shared facilities at the Nanoscale Characterization and Fabrication Laboratory, which is funded and managed by Virginia Tech's Institute for Critical Technology and Applied Science. Additional support is provided by the Virginia Tech National Center for Earth and Environmental Nanotechnology Infrastructure (NanoEarth), a member of the National Nanotechnology Coordinated Infrastructure (NNCI), supported by NSF (ECCS 1542100 and ECCS 2025151).

Thanks to the following individuals for training on various equipment: Mr. Stephen McCartney, Dr. Thomas Staley, Dr. Weinan Leng, Dr. Eric Gilmer, Dr. Guo-Quan Lu, Dr. Cailean Pritchard, and Mr. Chris Garza. Thanks to Dr. Jake Yoder for his insight into competitive adsorption of additives in colloidal suspensions.

The author would like to acknowledge her advisor Dr. Carolina Tallon, and the members of the committee, for their support throughout this dissertation work. As if graduate school were not difficult and complicated enough, going through it during a global pandemic has not been easy on any of us. Thanks especially to the committee for rooting for me and being there when I needed you.

Finally, many thanks to Kim Grandstaff. From the time that I was first considering Virginia Tech right through my last semester, you have demystified the process and been an invaluable resource.

Table of Contents

Chapter 1: Review of the State of the Art of Titanium Diboride and Research Objectives

Ultra-high temperature ceramics (UHTCs) are borides, carbides, and nitrides of metal transition elements from groups IV and V known for having melting temperatures exceeding 3000°C. Tolerance of such high temperatures, in addition to their stability in chemically reactive environments and strength under extreme pressure, mechanical wear, and radiation make these materials ideal for applications in extreme environments,[7,12] including thermal protection systems for atmospheric reentry and hypersonic flight vehicles (rocket components, engine turbines, leading edges) [2,3] as well as molten metal containment[3,13] and nuclear fission reactors.[14]

Titanium diboride (TiB_2) embodies many of these classic UHTCs traits, as summarized in Table 1. TiB_2 is known for its thermomechanical properties, including high hardness,[1,7,15] elastic modulus,[1] strength, and abrasion resistance at high temperatures.[1,7,15] It is resistant to oxidation up to 1100°C,[16] and much research focuses on prevention and mitigation of rapid high-temperature oxidation.[2] One of the main limitations, and therefore areas for research, is the difficulty in densifying TiB_2, which is exacerbated by the very high temperature qualities that make it so attractive.[1,17] Due to the covalent bonding of the hexagonal close packed crystal structure, TiB_2 has a low self-diffusion coefficient. While this provides the high melting point and other attractive properties at high temperature, it also means that the sintering temperature must be high, and even then can still require the use of pressure or additives to achieve high density.[1,2] Brittleness and low fracture toughness are also a concern for monolithic components.[15,18,19]

The processing procedures for TiB_2 are not as well-established as those for more well known ceramic materials like silicon carbide (SiC) or alumina (Al_2O_3), so the dependence of property values on microstructures has not been fully established.[20] Research into the variability of properties with respect to density is limited to specimens of high density, above 88% of theoretical, because nearly all state of the art applications for TiB_2 are structural components requiring full density.[20] Evaluating properties at high temperatures and in extreme environments presents unique challenges, and more research must be done to fully characterize the material in those environments.[19,21] In addition, most of the processing techniques for these materials are not very cost-effective, since they rely on high temperature and pressures for their manufacturing as well as using expensive commercial raw materials. Most often TiB_2 is synthesized through high temperature reactions. Note that production of borides is more costly than that of carbides because additional carbon is required to reduce the metal oxide, using almost twice as much energy per kilogram of material produced.[13]

Table 1: Nominal property values of fully dense TiB_2.

Property	Reported values	Reference
Crystal structure	Hexagonal close packed	[3,22]
Melting point	3225 °C	[19,22]
Density	4.52 g/mL	[22]
Molar mass	69.522 g/mol	[23]
Hardness	23.5 GPa	[24]
	15-45 GPa	[25]
	33 GPa	[24]
	25 GPa (room temperature)	[20]
Fracture toughness	6-8 MPa	[25]
	6.2 MPa	[20]
Strength	865-915 MPa	[25]
	400-500 MPa	[20]
Young's modulus	510-575 GPa	[25]
	565 GPa	[20]
Oxidation resistance	1100°C	[22]
	<1200°C	[19]
Thermal conductivity	25-77 W/mK	[26]
	60-120 W/mK	[22]
	96 W/mK	[20]
Thermal expansion coefficient	8.1 $x10^{-6}$ K^{-1}	[25]
	6.4-9.2 $x10^{-6}$ K^{-1}	[20]
Electrical conductivity	1-3 $x10^{7}$ S/m	[22,26]

1.1 Synthesis

The most traditional synthesis routes of TiB_2 involve high temperature (>1400°C) reactions: such as directly melting Ti and B together, or a hydrogen reduction reaction of boron and titanium halides.[3,7,27] Directly melting the constituents together is more suitable to a laboratory scale, as is hydrogen reduction.[13,28,29] The prohibitive cost of pure boron is one of the main reasons these are not used for industrial scale production.[13] Small scale production can also make use of silicothermic and aluminothermic reactions or chemical vapor deposition (CVD).[27,30] The carbothermal, borothermal, magnesiothermal,[7] carbo-borothermal, and boron carbide reduction of TiO_2 and boric oxide (B_2O_3) or boron carbide (B_4C) are more suitable to commercial production of TiB_2.[13,28,31] These synthesis routes have been well known for decades. Carbothermal reduction is the primary route commercially used for most non-oxide ceramic powder synthesis because of

low cost and simple processes.[7,13] By carbothermic reduction of titania (TiO_2) and B_2O_3 in an electric furnace, TiB_2 results from the following reaction:

$$TiO_2 + B_2O_3 + 5C \rightarrow 5CO + TiB_2 \qquad \text{[Equation 1]}^{30}$$

This reaction requires high temperatures, usually above 1400°C.[13] Kang and Kim have produced TiB_2 particles of 100 nm through carbothermal reduction at 1500°C, as opposed to the micron scale.[31]

The need for smaller particle sizes to improve sinterability, and/or the need for high purity and lower operating temperatures has led researchers to investigate less traditional synthetic routes. Among these are plasma produced powders, which can produce small and readily sintered particles[12,17,29] such as mechanochemical synthesis or self-propagating high-temperature synthesis (SHS), which make use of different reduction reactions.[3,24,32] Mechanochemical synthesis is the result of a combustive process occurring during ball milling, where TiB_2 is produced and byproducts can be chemically washed away.[30,33] Ricceri and Matteazzi have reduced production costs by optimizing the ball-to-powder ratio in the magnesium, TiO_2, and B_2O_3 reaction, yielding 50-100 nm particles in as little as 70 min.[30] With titanium chloride ($TiCl_3$) and lithium precursors ($LiBH_4$, LiH), Kim et al. has produced even smaller TiB_2 particles through mechanochemical synthesis, in the range of 15-60 nm.[33]

There are also self-propagating reactions where the heat given off perpetuates the synthesis. SHS can be initiated by electric current or microwave assistance.[32,34] Sundaram et al. have found that in the magnesium thermite reaction (Equation 2) to produce TiB_2, with bulk ignition by an electrically heated wire, self-heating ceases when all reaction products have formed, protecting the resulting TiB_2 powder from oxidation.[24] Microwave assisted SHS, the magnesiothermal reaction, aided by the addition of extra Mg, can yield 150-200 nm TiB_2 particles.[35] Combined with dynamic compaction, TiB_2 produced by SHS can reach greater than 99% theoretical density and high purity, provided starting materials have high purity themselves (>99.5%).[36]

$$5Mg + TiO_2 + B_2O_3 \rightarrow 5MgO + TiB_2 \qquad \text{[Equation 2]}^{24}$$

A solvothermal method proposed by Gu et al. produced 15-40 nm TiB_2 particles in autoclave at temperature as low as 400°C (Equation 3), although they note that the exothermic reaction likely causes the local temperature to temporarily exceed this. In this novel route, formation and crystallization occur at the same time, with some amorphous carbon distributed through the TiB_2 particles.[37] More research is needed to take further advantage of this mild synthesis at low temperature to optimize purity and nano-size of the particles. Synthesis at these lower temperatures would be more cost-effective, and costs could be further reduced by utilizing more inexpensive precursor materials. Overall, the high cost and low versatility of commercially available TiB_2

powder must be balanced with the considerations of synthesis: the cost and potential toxicity of reactants, the versatility in aspect ratio and morphology afforded by synthesis, and the importance of high purity.

$$2B + TiCl_4 + 4Na \xrightarrow[400°C]{Benzene} TiB_2 + 4NaCl \qquad \text{[Equation 3]}^{37}$$

1.2 State of the Art Applications

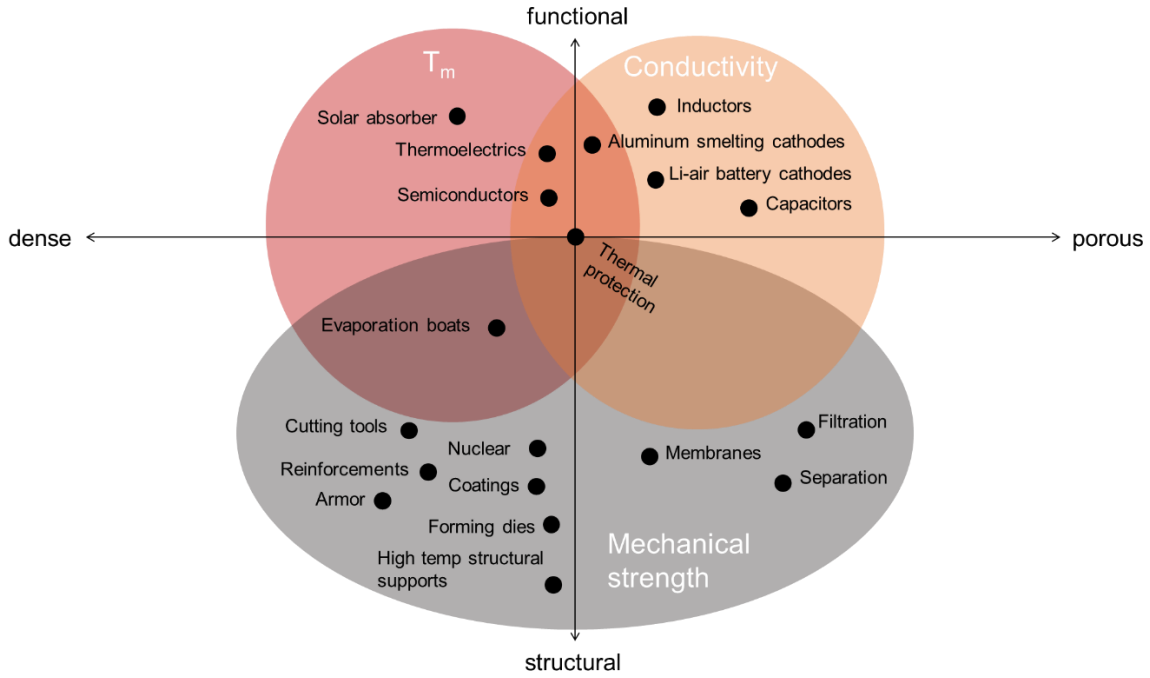

Figure 1: Schematic diagram of the structural and functional applications of TiB_2 as a function of the most relevant property and microstructures (dense versus porous) for that application.

Figure 1 shows a schematic representation of the applications that TiB_2 can be used for, organized by structural versus functional and dense versus porous, highlighting the most relevant property for each application. The most common applications of TiB_2 in the current paradigm lie in the bottom left quadrant of Figure 1: dense, structural materials. In these applications, mechanical strength is often the most important property in choosing a suitable material, and it is appropriate that TiB_2 maintains its mechanical properties in extreme environments. The state-of-the-art applications of TiB_2 include cutting tools,[1,7,24,38–41] armor,[1,2,7,39–44] wear resistant materials,[1,7,15,24,39–41] forming dies,[38] structural components in heat exchangers and engines (specific to titanium carbide (TiC)-TiB_2 system),[38] and electrical switch interfaces.[7] It is often used for reinforcing steel matrix composites and aluminum-based composites.[18] TiB_2 has been used as an additive in many other material systems, including SiC,[13] zirconium diboride (ZrB_2),[12] and B_4C.[45] Hot-pressed TiB_2 has long been known to be superior to other armor materials, oxide and

non-oxide,[1,3,13,17] and some recent examples indicate that even pressureless-sintered TiB_2 would reach the same performance.[17] Spark plasma sintered TiB_2 composites are also of interest as a gradient structure bridged by rod-like TiB crystals, which can eliminate the interfaces between layers, improving anti-penetration performance.[42] Application of TiB_2 coatings on titanium for the automotive industry has been achieved through a thermal boriding process that increases strength, hardness, and wear resistance.[46] This thermal diffusion process has mostly been used to boride iron alloys through a variety of avenues, including pack boriding, paste boriding, gas- and liquid-phase boriding, plasma boriding, and electrochemical boriding. Solid precursors are packed into the work piece before heating, and toxic byproducts are produced in the forms of solid waste and gas emissions. Electrochemical boriding is the newest and most cost-effective method. Boriding titanium in this manner does not produce any harmful byproducts, unlike traditional boriding processes. The pure TiB_2 layer produced is tunable between 1.85-8.5 μm thick.[46] Improvements to the structure and properties of TiB_2 coatings have been investigated by element addition, including both non-metallic and metallic elements.[15] For example, adding nitrogen to form a titanium nitride (TiN) phase in small amounts can improve the hardness of a TiB_2 coating, while adding aluminum improves the high temperature oxidation resistance.[2,15] Inclusion of carbon allows an amorphous B-C phase to form which encapsulates the TiB_2 grains, helping to prevent oxidation and increase mechanical properties.[15]

Molybdenum (Mo) has also benefitted from TiB_2 coatings. Mo is an attractive material for nuclear and aerospace applications but lacks sufficient oxidation resistance. Many materials have been investigated as oxidation resistant coatings, chiefly molybdenum disilicide ($MoSi_2$) based materials. Molybdenum boron silicon alloy (Mo-B-Si) has also been considered but does not have oxidation resistance below 1000°C. TiB_2 is an excellent new candidate for these coatings, as molybdenum has similarly high corrosion resistance and conductivity values, and TiB_2 provides oxidation resistance at low temperatures that Mo-B-Si cannot achieve. Some tools, like carbide cutting tools,[2,16] have utilized TiB_2 as a protective coating before, but not with the specific intention of increasing oxidation resistance. While this literature provides a foundation for improving the adhesion between the coating and the substrate, Huang et al.'s study is the first to address oxidation resistant TiB_2 coatings.[16] They found that CVD can accomplish good adhesion and high hardness of the TiB_2 coating, providing good oxidation resistance until the 720-900°C range is reached, whereupon the B_2O_3 glass oxidation product vaporizes and reduces the protection.[16]

Its thermal conductivity as well as mechanical strength, paired with its non-reactivity with molten copper, zinc, and aluminum, make TiB_2 an ideal crucible material for melting these metals,[3,13] outperforming other non-oxide high temperature ceramics. These qualities are the reason that TiB_2 has for so long been a main component of metallization boats or evaporation boats,[3,13,41] as well as thermocouple sheaths.[3] It is also helpful that TiB_2 produces solid boron upon decay, which prolongs the life of the boat by curbing vaporization.[13]

Most of the state-of-the-art applications discussed in this section typically require nearly full density components. In these dense ceramic bodies, pores are considered an undesirable feature since they may have detrimental effects on their expected performance.[4] These dense TiB_2 components are usually prepared using dry processing methods, including hot pressing or hot isostatic pressing (HIP) to fully densify the material and cold isostatic pressing (CIP) to produce bodies with excellent particle packing and shape accuracy for isometric geometries.[43]

However, dry routes limit near-net shaping capabilities to relatively simple geometries. The high electrical conductivity of this material does make it amenable to electrical-discharge machining (EDM)[44,47] to generate the final shape, but this is a costly step. Thus, achieving the nearest-net shape possible is a key factor determining the choice of processing route.[17] Even so, dry methods are usually preferred over plastic and wet routes because of the risk of oxidation and secondary phase formation when mixing powders with solvents and organic additives, and because of their simplicity and easy combination with hot pressing and HIP for densification.[11]

Densification of TiB_2 is difficult for a few reasons: its high melting temperature (3250°C), and low self-diffusion coefficient, and also the presence of oxygen contamination on particle surfaces that inhibits densification.[1,3,41]

- The high melting point necessitates the use of high temperature (>1800-2300°C) during sintering, but that may lead to exaggerated grain growth that lowers the thermal shock resistance and mechanical properties.[6,20,41] Additionally, the anisotropy of the hexagonal grain structure can cause anisotropic internal stresses which can result in spontaneous microcracking upon cooling.[23,29,40,43]
- The limited self-diffusion that restricts mass transport during sintering is associated with the covalent bonding of TiB_2.[1,23] Even with the application of pressure (30 MPa or more), sintering of pure TiB_2 requires high temperatures around 2000°C[1,6] and relies on the grain boundary diffusion mechanism.[29] Rapid grain growth occurs around 2100°C[29] and is detrimental to mechanical properties. Sintering can be improved either by increasing the total surface energy by using finer particles sizes or by increasing specific surface and grain boundary energy by reducing the oxide layer.[23,29,40,43] For these reasons, sintering aids are an important area of research for reducing temperature and pressure needed to fully densify TiB_2. Sintering aids can belong to a number of categories: oxides, nitrides, borides, carbides, and metals.[48] Generally, sintering aids are included in mass fractions ranging from 1-10%[23] and are comprised of a wide variety of materials chosen to help produce dense bodies, such as chromium (Cr), chromium diboride (CrB_2), carbon (C), nickel (Ni), nickel boride (NiB), and iron (Fe), which help to lower the sintering temperature and increase the speed of densification, although they can also increase the speed of grain growth.[6,49] Iron, nickel, and cobalt are some of the more common materials known to decrease sintering temperature significantly, due to their good wettability with TiB_2. Unfortunately, these metals degrade the unique properties specific to ceramics like

the high melting point, fracture toughness, hardness, and elastic modulus.[1,6] CrB_2 has been shown to subdue grain growth of fine TiB_2 powders during microwave sintering.[6] Non-oxides (SiC, TiC, B_4C) and oxides (Al_2O_3, zirconia (ZrO_2)) alike have been explored as sintering aids, always with the fact in mind that too much of a secondary phase will deplete the desirable properties of the TiB_2.[1]

- The oxide layer that forms on the surface of the starting powder is normally minimized using sintering aids. This restrictive layer of TiO_2 on the surface can be eliminated by the addition of C, SiC, and especially silicon nitride (Si_3N_4), which has many benefits in the hot pressing process: reacting with the oxygen rich layer to suppress grain growth and decreasing sintering temperature.[1] This additive, in small amounts (<5%), increases hardness and strength significantly and only slightly lowers fracture toughness.[1] Other non-metallic additives like $MoSi_2$, titanium disilicide ($TiSi_2$), and aluminum nitride (AlN) can help to remove oxide impurities and thus reduce sintering temperature at the expense of fracture toughness, which can fall to 4 MPa [40,50,51] from its usual 6-8 MPa, while the material without additives should have a fracture toughness between 6-8 MPa.[25] To prevent this issue, recent work includes the use of carbon additives for both oxide reduction and mechanical reinforcement, such as carbon nanotubes, graphite nanoflakes, and graphene nanoplatelets.[52]

Liquid phase sintering has also been explored,[3] but is limited in application because any secondary phase included must have similar high temperature qualities needed for application and the eutectic composition temperature must be well above the temperature needed for the application. The liquid phase encourages grain growth through Otswald ripening by enabling fast mass transport through the melted material.[43] Baumgartner and Steigner have stated that liquid phase sintering cannot produce a fully dense TiB_2 body due to the nature and amount of impurities needed and that previous reports of the successful use of the evaporation-condensation sintering mechanism may have been misunderstood effects of the purity of the powder used.[29] Metallic additives used in liquid phase sintering tend to maintain or enhance the mechanical properties but exacerbate grain growth[40] and reduce the high temperature qualities of the component overall. TiB_2-35 vol% (Fe-Ni) composites reached a relative density of 98% via pressureless sintering and improved fracture toughness and flexural strength.[41] There is no report of secondary borides forming during sintering, which speaks to the efficacy of the use of Fe-Ni.[18] Telle reports that the TiB_2/Ni/Co system does achieve successful densification through liquid phase sintering, but the beginning powders are mechanically alloyed with WC during the ball milling process. During sintering at high temperatures, the Ni/Co in the liquid phase evaporates, leaving a high concentration of tungsten (W), Ti, and B in the melt that can precipitate W_3NiB_3 and $TiWB_2$ that retards grain growth.[43] Non-metallic additives used in liquid phase sintering form the liquid phase or solid solution at the grain boundaries and ultimately lower the mechanical properties.[6]

The most common method of sintering TiB_2 is hot pressing. [39,53] This method is known to achieve relative densities greater than 98%.[1,39,53] Although it is limited to simple geometries that can be uniaxially or isostatically pressed, patents and literature contend that hot pressed TiB_2 retains better qualities than other sintering methods.[53]

Another form of pressure-assisted sintering used for this material is spark plasma sintering (SPS), which utilizes short electrical pulses during consolidation to rapidly heat the sample.[39] This route has the advantages of low temperature, shorter hold time, and faster processing.[3] Balci et al. have shown SPS to fully densify TiB_2 at 1400°C without sintering aids.[3] That said, SPS can lead to lower mechanical properties such as elastic modulus and hardness due to the accelerated densification inducing grain boundary stresses.[6] Alternatives which maintain the good mechanical properties of TiB_2, besides hot pressing, include microwave sintering and pressureless sintering.[6]

Microwave sintering has been used to reach the high temperatures required to fully densify TiB_2 faster without the use of radiative heat.[54,55] Instead, the material absorbs the electromagnetic energy to generate the heat, meaning that the heating is both selective and controlled.[54] This slightly more "environmentally-friendly" route saves money, though it presents unique issues with controlling arcing and optimizing the transfer of microwave energy.[54] It has been suggested that microwave sintering requires special formulas and processes to achieve its maximum potential,[54] which is why Holcombe and Dykes included 3% CrB_2 in their work, proving that microwave sintering could reach 1700-2000°C and densify TiB_2 to 98% theoretical with grains less than 15 μm.[55] As the research advances, fully dense TiB_2 samples have been produced at 1600-1700°C.[6]

Pressureless sintering, without the aid of force for compaction, relies on good particle packing in the green body and high temperatures (1800-2275°C) to densify TiB_2 to greater than 99% theoretical.[29] This method, developed prior to 1985, has not found widespread use for densification of TiB_2 despite clear advantages.[43] By that time, TiB_2 had been highly densified with this method in combination with the use of very pure, sub-micron powders. It can be used with dry or wet processing routes, with temperatures comparable to those of hot pressing.[40,56] Sintering aids or liquid phases, which may be used with any sintering method, can help to compensate for the lack of pressure in this case,[56] with cobalt being a rather successful example.[40] Future research looks to make further use of this valuable sintering method.

1.3 Cutting-edge research in TiB_2

TiB_2 has been a reliable dense structural ceramic component in many industries for decades. While its utility in these proven applications is bound to continue, there are more opportunities for research and development to expand the role of this material. By branching out from monolithic, fully dense TiB_2 bodies, many new applications could make use of this well-known material in novel architectures. Figure 1 illustrates how most applications for TiB_2 are for dense structural

material, relying on mechanical properties. There is a large field of potential applications and properties to explore, by shifting the development toward porous architectures and exploiting its other inherent properties like electrical and thermal conductivity, in the upper and right quadrants of Figure 1. In the following section, the newer applications are detailed.

1.3.1. Nuclear

Monolithic TiB_2 has not found a consolidated commercial use in the nuclear industry but is a candidate material for control rods[57] and radiation shields.[14] Both of these applications require fully dense components with fine grain sizes and no crack or agglomerate defects.[14,57] TiB_2 combines boron's neutron absorption capabilities with the high temperature performance needed in high temperature (1000°C) nuclear reactors.[57,58] A promising composite with B_4C has been shown to resist gamma radiation.[59] Further studies have suggested that the addition of TiB_2 to nuclear materials can improve hardness, strength, and gamma attenuation, making it a good shielding material.[60] A positive correlation between TiB_2 composite shield thickness and neutron absorption has also been established.[14] Overall, TiB_2 shows promise as a potential nuclear material but requires further research into its behavior under radiation and developing more cost-effective sintering techniques.[3,57]

1.3.2 Semiconductor devices

TiB_2 is an attractive candidate material for applications in ultra-large-scale integration (ULSI) of semiconductor devices because of its high electrical conductivity and chemical inertness at elevated temperatures,[8] which for semiconductors tend to be 85°C and below.[61] Low pressure chemical vapor deposition (LPCVD) can produce dense TiB_2 films of 100 nm onto silicon wafers for lithographic patterning.[8] However, the contact resistance is too high for this application, so TiB_2/p-Si diodes require further development.[8] In the meantime, TiB_2 may be used as a solder component. Polymer-derived ceramic solder for electrical connections in very small scale and extreme environments is a contemporary subject of interest.[62] Improved connections between ceramic and semiconductor devices through thermal cycling has fueled research into TiB_2 for microchip applications, and solder join composed of conductive TiB_2 and a B_2O_3-SiO_2-TiO_2-SiCN glass phase have been shown to prevent joint failure due to thermal expansion mismatch between solder and connections.[62]

1.3.3 Thermoelectric applications

Thermoelectric properties of dense TiB_2 are still lacking thorough investigation in the literature.[26] While previously published values for such relevant properties as the Seebeck coefficient, figure of merit (ZT), and thermal conductivity suggest that TiB_2 cannot make a successful thermoelectric material, it has been used in zinc oxide (ZnO) systems to improve thermoelectric properties: increasing power factor by ten times in the temperature range from 300-800 K and increasing the figure of merit by one hundred times at low temperature (300 K) and two times at 800 K. This

improvement is due to the high conductivity of TiB_2 and the approach of coating the TiB_2 particles in ZnO to prevent direct contact between TiB_2, thus mitigating the loss in Seebeck coefficient.[63] Malik et al. investigated the lead selenium (PbSe)/TiB_2 system. The use of a PbSe/TiB_2 composite with PVA is a promising option for better thermoelectric semiconductors. The high electrical conductivity of TiB_2 presents an opportunity to increase the Seebeck coefficient of pristine PbSe from -350 μV/K to -342 μV/K. The power factor increased slightly from 0.1 to 0.12 with the addition of TiB_2, providing the foundation for further research in controlled addition of TiB_2 to understand how much TiB_2 is needed to achieve sufficiently high power factor.[26]

1.3.4 Solar Absorber

Current Concentrating Solar Power (CSP) plants are limited to operating temperatures below 800 K due to limitations of the sunlight receiving materials.[39] Using ceramics as the sunlight receivers or heat exchangers is an attractive option because of the higher melting point compared to the currently used metals, which would increase operating efficiencies.[64] Investigation of TiB_2 as a novel sunlight absorber is of interest for increasing the efficiency and applicability of these plants. The solar absorber material must exhibit a high sunlight absorption and low re-radiation losses.[39] In general, materials in the UHTC family have great potential for this application because of their intrinsic spectral selectivity (1.0-4.0 at 1000 K). TiB_2 has the further advantage of lower density than the other borides. Very little of TiB_2's optical properties have been explored until recent years. Sani et al. reported that the surface roughness of fully dense, hot-pressed TiB_2 is as good or better than ZrB_2 and tantalum diboride (TaB_2) in its ability to trap and absorb photons. Using the reflectance spectrum to calculate the solar absorbance value α shows that TiB_2 (α=0.49) absorbs sunlight better than ZrB_2 (α=0.47) and TaB_2 (α=0.4). TiB_2 has a spectral selectivity between SiC and the other borides, as well as a higher solar absorbance than the borides. This combined with its lower weight compared to zirconium and tantalum borides makes it an excellent candidate for future research into new solar absorber materials.[39]

1.3.5 Electrochemical applications

The ever-increasing pressure to transition to more renewable energy sources and sustainable storage technologies has brought more attention to catalysts for hydrogen evolution reactions (HER). Thus far, platinum has been shown to achieve the highest HER rate, but the availability and cost are prohibitive. The most exciting properties of spin-, drop-, and sputter-coated TiB_2 relevant to this application are high stability, thermal conductivity, strength, and resistance to erosion, as well as low electronic density at the Fermi level.[7,65,66] However, its ability to catalyze HER and oxygen reduction reactions (ORR) has not been widely explored. Lim et al. characterized electrochemistry of TiB_2 before and after treatment with sodium naphthalenide (NaNAFT), an alkali metal compound used for intercalation of other layered materials. They found that untreated TiB_2 produced the fastest heterogeneous electron transfer (HET) rate, while the treated samples performed worse than the currently used glassy carbon material. However, smaller overpotentials

were required for the modified TiB_2 components to armor reach the benchmark current density of -10 mA cm^{-2} in the electrochemical test cell. Specifically, the TiB_2 modified with NaNAFT was the most catalytically active for HER. Even though TiB_2 did not do better than platinum, synthetic adjustments may be the key to adapting this material to greater performance.[7]

Along these lines, oxygen-evolution reactions (OER) also require abundant and low-cost catalysts for electrochemical fuel forming processes. Layered TiB_2 coatings on electrodes are one such earth-abundant catalyst and have exhibited good Faradaic efficiency in acidic medium in Kirshenbaum et al.'s work.[66] Further research into mechanical adhesion to the electrode is needed.[66] TiB_2 coatings on hematite (α-Fe_2O_3) photoanodes for solar water splitting have been shown to significantly accelerate the oxidation kinetics of the reaction for producing hydrogen.[65]

1.3.6 Cathodes

1.3.6.1 Aluminum Smelting Cell cathodes

For many years research into the Hall-Heroult process of smelting alumina into aluminum has focused on finding a better inert cathode material than carbon; improvements to the efficiency of the smelting cell would reduce costs significantly,[53] but there are not many candidate materials that could withstand the extreme operating environment (700-900°C).[11] TiB_2 is wettable by aluminum, the first essential quality for this application, and it also has the high melting point, low solubility in alumina, and high electrical conductivity required, setting it apart from the other refractory ceramics.[11,67–69] Corrosion resistance under high temperature and molten fluoride salt and resistance to cracking are also important.[53] The drawbacks of this material choice are mainly the high cost of processing at high temperature and pressure, although it is the least expensive of the borides wettable by alumina.[11] Low resistance to thermal shock is also a concern[53] and it has been suggested that impurity contamination is the main reason that TiB_2 cathodes were not utilized sooner.[6] Carbides and nitrides have also been considered, but do not possess the necessary conductivity and inertness.[11] TiB_2 cathode materials for this application include composite TiB_2, TiB_2 coatings, and monolithic TiB_2.[53] Tallon and Franks have explored approaches to make use of TiB_2 more affordable without altering the smelting cell or the inherent material properties, namely, by mixing an optimized amount of fine and coarse TiB_2 powders to reduce material cost, and by utilizing colloidal processing techniques to reduce processing costs. The latter also allows for pressureless sintering and near-net shaping of the component, both economic advantages to hot-pressing or hot-isostatic pressing followed by further machining. They found that using only 50% of the more expensive fine powder and 50% coarse powder improved the particle packing of the green bodies. Pressureless sintering at 2100°C did not achieve the goal density of 92% even with the addition of TiC as a sintering aid, but it is suggested that higher sintering temperature could achieve the desired closed porosity. Most importantly, the colloidal approach is shown to be an excellent starting point for reducing costs.[11]

Composite cathodes usually pair TiB_2 with other non-oxide ceramics or with refractory metals.[53] Carbides and borides can improve the mechanical and sintering properties of TiB_2 without significant cost raises.[53] In particular, thermal shock resistance is greatly improved in a TiB_2-TiC composite, although it is at the expense of electrical conductivity.[53] Composites with carbon or graphite perform well in all areas except the mechanical integrity during operation.[53] These carbon-TiB_2 composites exhibit increasing resistance to sodium expansion proportional to TiB_2 content.[67] It has even been suggested to add sodium to the composite cathode to increase resistance to sodium penetration during operation.[53] Notably, sodium expansion in TiB_2 cathodes is still less than in traditional graphite cathodes.[70] While there are many options in the composite realm, none has yet emerged as the preferred material.[53]

TiB_2 coatings on cathodes are of interest for their wear- and corrosion-resistance.[7,24] TiB_2 is an excellent coating material for a carbon substrate due to their similar expansion coefficients. Coatings of about 0.2mm thickness may be applied via CVD, electrochemical deposition, and plasma spraying.[27,53] Electrochemical deposition offers the advantages of smooth coatings even on complex geometries, and low cost.[27] A coated cathode must utilize a dense coating to avoid penetration of the electrolyte and liquid aluminum into pores, which TiB_2 has been shown to do.[53,69] The carbon-bonded and colloidal alumina TiB_2 coatings have shown promise, but the life span of these coatings must still be improved.[53] The TiB_2 inclusion does not change the penetration mechanism, so the graphite base still experiences sodium penetration, but the TiB_2 does slow the rate of penetration, extending the life of the component.[27] TiB_2 coatings on carbon cathodes have not found wide usage industrially yet because of the high cost of heat solidification at 200°C which must occur after coating. Some work has been done to produce a TiB_2 coating cured at ambient temperature to avoid this step; in this case, the combination carbon and TiB_2 coating with an organic resin was applied to the carbon cathode with a trowel in a layer 3-5 mm thick, resulting in good adhesion, strength, thermal shock resistance. It is believed that this coating could improve current efficiency by only 1.48%.[69]

Pawlek argues that the greatest advantage of TiB_2 as a wettable cathode is not the potential to improve Hall-Heroult aluminum electrolysis cells, but to support the new generation of electrolysis cell designs.[68] However, this work focuses on TiB_2 as a composite material to eliminate the difficulties of processing monolithic TiB_2.[68] Composites suffer from reduced corrosion resistance to the electrolyte, but this has not halted the research into TiB_2 coatings deposited by electrophoretic deposition, plasma spraying, and simple slurry application.[68] While research continues, industrial scale testing is rare and much work remains to be done.[68]

1.3.6.2 Lithium-Air Battery Cathodes

With the promise of a theoretical energy density ten times higher than Li-ion batteries, lithium-air (Li-air) battery research focuses on increasing the experimental energy density to the theoretical

values.[71] In this battery, which contains a Li anode and a porous cathode through which air from the open atmosphere may flow in, the largest barrier to improvement is poor cyclability caused by deposition of discharge products in the cathode pore network.[71–75] The cathode material, which is currently the dominating factor in this research,[76] must be thin, stable in the battery environment, and conductive.[71,77] Electrical conductivity needed for this application ranges from 10-200 S/cm.[77] The structural considerations of the battery are more complicated and more disputed. A through-connected pore network must allow flow of air and ions, resulting in a high specific surface area. The tortuosity of the pore network must be low enough to facilitate easy flow[78] but not too low or the cathode may as well be an unguarded opening to the atmosphere;[79] surface area must be sufficient to allow chemical reaction to take place.[74] Tortuosity values must balance the theoretical maximum discharge of a battery with the need for flow, and this may be accomplished through anisotropy in the pore network.[79] In the literature, proposed solutions to the rechargeability of Li-air batteries include a separate electrolyte storage unit,[71] dual-scale porosity, catalyst distribution,[73] and increased size and uniformity of pores.[80] Interestingly, few structural properties of the next generation Li-air battery cathodes are agreed upon in the literature, often including contradictory reports. Table 2 is a summary of many of the discussed properties needed in this type of cathode.

Table 2: Summary of properties and structures needed and/or tested for Li-air battery cathodes.

Property	Value reported	Key Notes	Reference
Pore size	6.6 nm	Pores <10nm easily choked by discharge products	[74]
	14.23 nm	"wide" pore size facilitates better capacity/discharge	[81]
	17-24 nm		[82]
	42.7 nm	Clogged almost entirely on discharge in test cell Unlike micropores, this size pore allows reaction to take place	[74]
	Mesoporous volume	The more mesoporous volume, the higher capacity	[81]
	Interconnected macroporous free volume (>50nm)	Allows air transport	[71]
Pore size distribution	Bimodal	Micropores found to be unhelpful	[74]
	Two different pore structures by layering different carbon structures	Improves oxygen transport Delays clogging Minimizes tortuosity[78]	[73,78]
	Uniformity of pores		[80,83]
BET Surface area	1.45 cm^3/g		[74]
Surface area	824 m^2/g	Gave the highest specific capacity, author attributes specifically to surface area in combination with pore size	[74]
	300-500 m^2/g		[71]
Pore structure	Mesoporous foam	Capacity of battery increased because reaction occurs in hollow cell spaces, not just at ceramic surface	[74]
	"Carbon paper supported carbon nanofoam"		[71]
	Carbon aerogel		[81]
	Tunnel-like channels	Impractical to manufacture at large scale	[78]
Pore wall thickness	4 nm		[74]
Pore shape	Spherical		[74]
	Tunnels or periodic channel array where all porosity is straight channel and distance between channels is "vanishingly small";	Impractical	[78]

	channel diameter = 6um, spacing =17um		
Overall porosity		Highest mesopore volume corresponds to highest capacity	[81,82]
	0.9	Higher porosity improves capacity	[77,81]
	0.75	(used as benchmark)	[77]
Pore volume	2.195 cm^3/g	Greater pore volume gives better discharge capacity	[81]
	1.5-3 cm^3/g		[82]
	3.146 cm^3/g		[82]
Tortuosity	1.8-2.4	Too much tortuosity limits oxygen flow	[77]
	1.5	Higher capacity than cathode with tortuosity =3	[77]
Electrical conductivity	1000-20,000 S/m		[71]
	10 S/m		[77]
Thermal conductivity	1 W/mK		[77]
Cathode thickness		Limited by oxygen diffusion length. Ideal to minimize distance oxygen must travel to react within battery	[71]
	.1-1 mm	Used for small modeling purposes	[77]
	<1 um		[72]

Colloidal processing of TiB_2, and tape casting especially, can achieve many of these benchmarks. See next section (New Microstructures and Architectures) for more information about colloidal processing. Although TiB_2 is heavier and more expensive than the traditional carbon cathode,[75,77] it is highly resistant to chemical wear that may take place within the battery environment. The high melting temperature may also make TiB_2 a good candidate, perhaps to deal with the detrimental byproduct of Li-air battery discharge that clogs the pores and prevents rechargeability, lithium peroxide, which has a melting temperature of 1400°C.[77,84] The thickness of this deposit needed to cause cell death is reported to be 5-10 nm.[77] If heat treatment were to be applied to clean the pore network of the cathode, TiB_2 would far outlast the melting of the precipitants.

1.3.7 Thermal Protection Systems

TiB_2 and the other UHTCs have been of interest for use in thermal protection systems for hypersonic vehicles due to their high melting points and ability to distribute heat and load across

the vehicle airframe in the extreme environment of space and atmospheric reentry. Monolithic UHTCs for leading edges are attractive for resisting the heat flux of atmospheric reentry. Research has begun to turn toward cooling components as well. Active and passive cooling components rely on the ability control thermal conductivity directionally, which can also lead to increased reusability of the vehicles.[5,85] By designing anisotropic porosity either through functionally graded or aligned pore networks, the heat (>3000°C) can be directed away from sensitive components with lower melting temperatures. Aligned pores work by conducting heat along the direction of alignment and insulating in the perpendicular direction.[5] The pores can also be filled with a heat exchanger to provide more active cooling.[86]

1.4 New Microstructures and Architectures

To form more complex shapes and keep costly machining to a minimum, other processing routes can be utilized. Plastic routes offer more microstructural control than dry routes with minimum solvent added. By adding thermoplastic or thermosetting polymers to a slurry, a viscous paste can be formed and the shaping capabilities extended. Extrusion and injection molding can be utilized to form bars, which can be cut into bricks, or complex honeycombs which are used for catalyst supports.[87] A UHTC like TiB_2 may be extruded to form continuous, aligned pores for applications in active cooling, although there has also been research pertaining to achieving such pores through sacrificial fillers.[5] Very little research has addressed these plastic routes for TiB_2 by itself, and more deals with the UHTCs additives to ceramic composites.[88]

Colloidal processing routes offer the ability to control surface chemistry of particles, giving greater control over the stability of suspensions and quality of the overall product than is afforded by dry processing routes.[10,56] One of the most important requirements to achieve a stable suspension is controlling repulsive forces acting between particles to deter agglomeration, flocculation, and sedimentation.[10] When the dominating force between particles is attractive, the particles will agglomerate and settle. Therefore, repulsive forces between particles are required to produce a well-dispersed and stable suspension.[89] The electric double layer (EDL) forms around metal oxide particles in a polar solvent to maintain overall electrical neutrality of the system. The EDL causes a repulsion force between particles, which we rely on to keep the suspension stable. Similarly, steric repulsion caused by adsorbed polymer layers that overlap and compress each other repel particle surfaces from each other.[90]

The particle packing in green bodies is increased compared to dry routes and this has been shown to improve sintering behavior of TiB_2, lower sintering temperature, and in some cases eliminate the need for applied pressure.[11] Colloidal processing encompasses many techniques, including freeze casting, slip casting, and gel casting.[87,91] Pressureless sintering, as described earlier, offers the ability to produce more complex, asymmetric ceramic bodies than hot pressing.

With small particles (<10 μm), TiB_2 can be suspended colloidally and shaped using wet routes.[10,87] The colloidal routes offer the greatest flexibility in shape as well as improved particle packing and microstructural control.[10,91,92] Microstructural control is necessary to produce a wide variety of more complex microstructures, such as porous ceramics, which is not possible with the traditional dry pressing methods—designing the amount, morphology, connectedness, and distribution of the porosity.[93–95] The suspensions being cast must include additives suitable to the method, including dispersant, binders, plasticizers, and wetting agents.[91,92]

TiB_2 has been prepared using most of the common colloidal processing methods: slip casting, freeze casting, and gel casting. Tape casting of pure TiB_2 is notably absent from the literature, although other UHTCs have been made this way,[96–99] and composites including TiB_2 have also been tape cast.[42]

1.4.1 Porosity

Pushing the utility of TiB_2 into the right quadrants of Figure 1 requires learning more about porosity in this material. The need for porous materials that can withstand extreme thermal and chemical environments continues to increase.[4] As described in the previous section, porous UHTCs are of particular interest for thermal protection systems for hypersonic vehicles. Macroporosity (pores >50 nm) can be purposely introduced to ceramics in four main ways: partial sintering, sacrificial fillers, replica templates, and direct foaming.[4] Mesopores (2-50 nm) and micropores (<2 nm) can be introduced through surfactant templating, emulsion templating, sol-gel processing[63] and more. Through use of gradient porosity or continuous aligned pores, this anisotropic thermal behavior can be achieved.[5] The literature is still experiencing a lack of information about porous ceramics, especially having to do with UHTCs, porosity adjustment, and aqueous-based systems.[4]

Thin, porous ceramics are needed for filtration systems, catalyst supports, and electrochemical systems, to name a few applications. Ceramic membranes for filtration and separation can withstand higher temperatures and more extreme pH values than organic membranes. They are used in the textile industry to remove coloring agents, in the food and pharmaceutical industry, and in the recycling of wastewater. The same manufacturing processes are used to produce ceramic catalyst supports.[100] The pore sizes for these various applications must be tunable, especially those that require a gradient of decreasing pore size along the component.[101]

The microstructural parameters relevant to porous ceramics include pore size and shape, distribution, connectivity, and tortuosity.[4,5] Due to the varying needs for these parameters in different applications, processing routes that allow for controlled variation of porosity are important. In the case of TiB_2, partial sintering could be a preferable route for introducing porosity because it takes advantage of the difficulty in densifying this material. In partial sintering, the

necking phase of densification takes place but the heat applied is interrupted before necking and grain growth allow for the pore removal stage.

The thin, planar architecture required for many of the new applications can be achieved through tape casting, a process by which the ceramic suspension is spread over a substrate using a doctor blade. Tape casting is used to fabricate large planes of material tape typically thinner than 1000 μm.[4] Tapes are used in electronic applications such as capacitors, inductors, integrated circuits, and actuators[9], although there are exceptions; in structural ceramics: Al_2O_3 composite and SiC laminates;[96,102] and catalytic oxide membranes for improving selectivity of separation membranes.[103,104] If flexible in the green form, tapes may be folded, rolled, or otherwise molded to more complex shapes. Tapes can also be cut and stacked to form three-dimensional parts, and can produce uniform orientation of high-aspect ratio particles within the tape, which can then be used in such applications as capacitors, inductors, and sensors.[9,105,106] Solid oxide fuel cells have made use of tape cast nickel oxide (NiO) and yttria stabilized zirconia (YSZ) based anode substrates.[107,108] Gradient B_4C structures[98] have also been achieved. Porous tapes are often used for biological applications and for catalyst supports. Silicon oxycarbide microfilters and other thin membranes can be designed with hydrophilicity or hydrophobicity through control of pore size, which can be achieved through choice of fillers or pyrolysis temperatures.[106,109]

Much has been published about tape casting of oxides and non-oxides, but there has been little work done in tape casting UHTCs. Until recently, very few studies on the tape casting of ZrB_2 and B_4C existed.[96,98,99] Aqueous tape casting of ZrB_2 focused on dispersion quality of the powder in water and the amounts of binder and plasticizer needed to tape cast.[99] SiC, on the other hand, has been tape cast in organic solvents for Si/SiC composite layered structures, but the systematic study of aqueous tape casting of SiC is new; recently it has been accomplished and produced green bodies with 53% theoretical density.[97]

1.4.2 Complex Architectures

Additive manufacturing is capable of processing complex geometries faster and with less human interaction than traditional processing methods but is currently more matured for metals and polymers than for ceramics, due to the relatively young age of the technology[110] and the much higher melting points of ceramics.[111] The low self-diffusion coefficient and low laser absorbance of TiB_2 specifically makes it especially difficult to additively manufacture.[112,113] As such, TiB_2 has mostly been additively manufactured only as an additive to such other materials as metal alloys like Inconel and steels.[114–116] Oxide ceramics have been additively manufactured[112] as have some non-oxides (SiC, Si_3N_4) and composites containing borides, but to extend usage to monolithic TiB_2, more research is required.[117] ZrB_2 has been investigated for use in electron beam melting (EBM), a powder bed process by which the electron beam selectively heats the powder in the desired pattern. The resulting consolidation for electron beam power of 500 and 1000 W and

scanning speeds from 500-1000 mm/s was deemed satisfactory, with acceptable surface roughness and minimal cracking due to thermal stresses.[110] This work suggests that additively manufacturing other UHTCs using EBM is feasible. Selective laser sintering (SLS) of ceramics particles encased in polymer shells is also being pursued for a variety of ceramics, including TiB_2, TiC, SiC, ZrB_2, Si_3N_4, B_4C, and TiN. In this case, the polymer shell is used to bind the ceramic particles together in the design imparted by the laser.[111] Binder jet additive manufacturing has also been explored for UHTCs for production of triply periodic minimal surface geometries for heat exchangers in concentrated solar power systems. This complex geometry has only been made feasible for widespread fabrication with the advent of additive manufacturing because extrusion of these structures tends to result in thermal stresses and anisotropic mechanical behavior.[64] Recent work has found that composites of ZrB_2 and $MoSi_2$ fabricated by binder jetting followed by pressureless sintering achieved theoretical densities of 92-98% and that the process may be extended to other UHTCs, without the residual stresses of other methods.[64] SLS of TiC and of TiB_2-B_4C composites has been achieved through in-situ synthesis and sintering.[113] This was accomplished by mixing Ti powders with the other component powders in the powder bed to exploit the better laser absorbance of Ti than Ti-ceramics.[112,113] The exothermic reaction that results in the TiB_2-B_4C composite also benefits this process and produces a 93.8% dense component.[112]

Direct ink writing (DIW) is a wet additive manufacturing process, as opposed to the dry routes involving SLS of dry powder beds. The use of colloidal processing with additive manufacturing provides even more complex shaping abilities along with microstructural control.[10,117,118] DIW can accomplish structural complexity, but manufacturing ceramics in this way is known to cause shrinkage up to 40%, high porosity, cracks, and deformation, which limit its applicability. Research has begun into using inorganic binders to mitigate the disadvantages caused by pyrolysis of organic binders, which are thought to be responsible for much of the shrinkage and crack formation. Success in adjusting the binder for DIW of Al_2O_3 may provide the basis for similar advances in DIW of TiB_2 and other non-oxide ceramics.[119] Furthermore, ZrB_2 has been produced via DIW with purposeful porosity for use as thermal protection systems. This porosity (72-77%) can be achieved by printing particle-stabilized foams or capillary suspensions.[120] B_4C has similarly been prepared via aqueous colloidal processing and DIW with some success, focusing on preparing the colloidal suspension for optimum dispersion to additively manufacturing the complex shapes, resulting in complex shapes with no warpage and density of 82%.[117]

1.5 Research gap and motivation

As discussed in the previous sections, TiB_2 has mostly been limited in applications to dense structural components that take advantage of its good mechanical strength in extreme environments. To expand its utility and explore other applications in the porous and functional realms, more research is needed about how to process this material with designed porosity, how that porosity will affect its properties, and how different architectures might take advantage of its

other valuable properties like high thermal and electrical conductivity or high melting point. This work could be very useful for example in researching new cathode materials for Li-air batteries, which require a connected pore network for diffusion though a thin ceramic body that must maintain chemical stability in the operating environment of the battery. Tape casting of TiB_2 can reach many of the benchmarks for the thickness of the component and porosity required for this application.

Very little has been done to explore porous TiB_2 up to this point, and this material has never been tape cast before, because of the traditional approach of avoiding solvent-based processing methods for this type of ceramics. This dissertation begins by developing the necessary suspension formulation for aqueous tape casting this material.

Tape casting is known to align anisotropic particles along the direction of the moving substrate. This is due to a non-uniform velocity imparted on the particles by the shear force of the doctor blade and the moving substrate. When the long axis of the particle is parallel to the cast direction, the rotational velocity is at a minimum, and when the long axis is perpendicular, the velocity is at a maximum.[9] Subsequent to this alignment, the drying and sintering processes introduce anisotropic shrinkage to the ceramic.[9] Greater shrinkage occurs in the lateral direction because of greater number of particle boundaries.[121] To avoid anisotropic shrinkage, one may opt for the most isotropic particles possible; spherical particles cannot orient, and therefore tapes cast with spherical particles shrink nearly isotropically.[9] In most applications, if the component shrinks more than 15% in any direction, the residual stresses will cause mechanical failure.[9]

However, if the process is controlled, it can lead to new material properties and behavior. For example, the self-shaping of ceramic parts inspired by cellulose fibrils in plants has been achieved by selective alignment of alumina nanoparticles and control of the shrinkage process.[122] The local and anisotropic shrinkage caused by this alignment allows for the production of complex shapes needed for applications like motor blades, wire guides, and microgears.[122,123] Top-down production of these geometries via injection molding or additive manufacturing must be combined with cutting and gluing of green bodies to achieve such pieces as hinges, chains, and encapsulated ceramics. Purposeful anisotropic shrinkage to achieve complex shapes can eliminate the weak interfaces introduced in gluing processes. Warpage is usually avoided in ceramic processing due to the residual stresses it can introduce, which may severely crack and distort the piece. However, researchers have begun taking advantage of controlled warpage through particle alignment to achieve complex macrostructures. Various bending and twisting shapes can be achieved in this way by aligning alumina platelets coated with magnetic nanoparticles using magnetic force and varying the alignment direction between the layers of a component. During sintering, deformation in the intended directions relieves the internal stresses caused by anisotropic shrinkage due to alignment of platelets.[122]

Particle alignment in ceramic materials allows control of the properties in selected directions, often aiding reinforcement mechanisms. Placing a rod or whisker-shaped particle in a ceramic body can also provide toughening mechanisms like crack bridging and pullout.[124–127] Inclusion of SiC whiskers has been shown to more than double the fracture toughness of various ceramics, including Al_2O_3, ZrO_2, mullite, and Si_3N_4.[124] Alignment of these whiskers can also increase densification and homogeneity of the reinforced ceramic.[124]

Combined with such strategies as sacrificial fillers, alignment due to tape casting could be taken advantage of for the formation of aligned pore networks as well. In general, alignment of particles provides anisotropy which can cause greater strength or fracture toughness in one direction vs another, giving greater control in the forming process.

The alignment of the particles in the slurry is independent of the viscosity of the slurry because the changes in shear rate driving the particle motion and the resistance to that motion associated with different viscosities cancel each other out.[9] It has been suggested that increased solids loading increases the amount of alignment[121,128] and that water-soluble binders added proportionally to increasing solids loading tend to segregate normal to the z-direction, which can mitigate the strength of alignment.[121] However, increased solids loading will naturally reduce the amount of shrinkage, so without orientation measurements, it is difficult to conclude only from less anisotropic shrinkage that more alignment has occurred. The main factor in particle orientation is the aspect ratio of the particle, with greater aspect ratio particles tending to orient more strongly in the casting direction.[9,124]

Characterization of the orientation of particles in ceramics is divided into two categories: measuring the strength of crystallographic peaks in XRD or Electron Backscatter Diffraction (EBSD),[121,124,129–134] and using image analysis for physical alignment.[9,121,129,132,135,136] Crystallographic alignment can be further made use of by templated grain growth.[132] Image analysis can use any of three main definitions of alignment: the feret diameter or line joining boundary points that are farthest apart, the major axis of the best fit ellipse, and the axis of minimum second-order moment of the shape.[137] The measured angle with respect to the casting direction may be measured in degrees or radians, and the resulting distribution may be reported as a linear distribution or as a polarogram or von mises distribution.[121,135,138]

Investigation of the porosity and properties of sintered tape cast TiB_2 is the focus of the third chapter of this work. The TiB_2 particles cast here have an aspect ratio of 1.47; TiB_2 is commercially available in very limited morphologies, and as this is the first work of its kind, the easily available powder is the subject of study. Sintered tapes' microstructures are analyzed to quantify the amount of alignment and compare to theoretical predictions. The mechanical properties of sintered tapes are reported and compared to theoretical values for porous ceramics. Addition of a highly

anisotropic particle (the metal organic framework PCN-222) is utilized to further investigate alignment during tape casting.

Whiskers, rods, and other high aspect ratio particles are useful as reinforcements. Even with the most controlled processing, monolithic UHTC materials may not have the required thermomechanical performance in extreme environments, so additives that act as microstructural reinforcements are necessary. High aspect ratio ceramic particle reinforcements have been widely researched to improve fracture toughness and other mechanical properties by deflecting and bridging cracks. The most common material for these reinforcements is carbon or silicon carbide.[125,143–145] The more closely the reinforcement material's properties compare to the bulk material's, the fewer issues are caused by differing reactions to extreme environment conditions. Silicon carbide whiskers are the only widely available whisker, but recently some titanium carbide,[127] zirconium diboride,[126] and ZrC[145] whiskers have been synthesized.

The MOF particle used in this work, PCN-222, decomposes into a glass-like carbon matrix embedded with ZrC during heat treatment. ZrC is another of the UHTCs with a high melting point, attractive for reinforcing other materials in extreme environments, but production of many UHTC components often uses commercially available UHTC powders, which typically have relatively large sizes (dv50 typically between one and tens of microns) and irregular shapes as result of communition processes. There are not many cost-effective synthesis routes currently to produce large amounts of UHTC raw powders. These few synthesis routes commonly rely on carbothermal reduction, typically performed under vacuum in a graphite furnace, between zirconia (ZrO_2) and carbon black (C) particles, which can take over 16 h to complete at temperatures above 1800°C.[141,142]

In the second chapter of this work, we show a novel route for synthesizing high aspect ratio ZrC-based particles through high temperature pyrolysis of highly anisotropic PCN-222. These high aspect ratio particles will be used in tape casting to understand the potential orientation of anisotropic particles during the casting and explore the properties derived from them. The rod-shaped metal organic framework has a Zr cation within a carbon-rich ligand structure. Thermal treatment PCN-222 at 2000°C yields highly pure ZrC nanoparticles encapsulated in carbon rods. The study compares PCN-222 before and after heat treatment. Characterization of the resultant material reveals the presence of ZrC nanoparticles embedded in a glass-like carbon matrix. The resulting particles retain the defined geometry and size features from the original MOF, while showing high crystallinity and purity. These attributes in ZrC are extremely important for a reinforcement for UHTC in extreme applications, and the implications to develop other particle morphologies to further tailor material performance.

TiB_2 suspensions were then prepared with 2wt% of the MOF PCN-222 for tape casting (denoted TiB_2+HAR, high aspect ratio particle). That this addition may be made to the suspension

formulation established in the first chapter is a testament to the robustness of that formulation. The final chapter deals with characterizing the porous, sintered TiB_2 tapes and exploring the inclusion of heat-treated PCN-222 in the suspension. The goal is to understand how the porosity affects the mechanical properties of the tape and how inclusion of an anisotropic particle may take advantage of the alignment which occurs during tape casting.

1.6 Summary

This literature review focused on the established properties of TiB_2 and how they translate both to the well-known applications of the material and the future areas where TiB_2 shows great promise. Chief among these is the lithium-air battery cathode, which along with the rest makes use of the inertness in extreme chemical environments and high melting temperature. As testing methods allow for quantification of properties in hotter and more corrosive environments, TiB_2 may prove even more useful. Further exploration of processing routes like colloidal suspensions and pressureless sintering, as well as new architectures like tape cast and porous TiB_2 will allow for better utilization of the material's high thermal and electrical conductivity in new applications. Generally, a more thorough understanding of the material's drawbacks and ways around them will allow for applications in nuclear, solar, electrochemical, thermoelectric applications and beyond. This dissertation's objectives represent the first step in shifting the processing paradigm of TiB_2 toward these exciting new applications.

1.7 Dissertation Objectives

As discussed in the previous section about research gap and motivation, the specific objectives of this dissertation are the following:

1. Investigate the possibility of developing an aqueous suspension formulation for TiB_2 to produce flexible, uniform tapes with the least number and the lowest amount of additives as possible. In order to do that, surface chemistry and rheology will be studied in detail to correlate with the macroscopic properties of the tape, as a function of the casting parameter. The main contribution to the field includes the establishment of the relationship between processing parameters and the green tape qualities for this type of material and producing TiB_2 tapes for the first time in the literature.
2. Synthesize high aspect ratio particles of UHTCs, via a novel route employing metal organic framework materials (MOF) and carbothermal reaction to transform the organic skeleton surrounding the cation into selected carbides. This synthesis route seeks to obtain particles with same aspect ratio and size as the precursor, to utilize them as second phase as reinforcement in a ceramic matrix, or tailor other properties. The main contribution to science and engineering will be the use of novel precursor for the first time to create type and shapes in UHTC particles that cannot be attained with other synthetic methods. The results could be applied to future MOF structures and chemistries to synthesize TiB_2,

through similar thermal decomposition of MOFs. These high aspect ratio particles will be utilized in the final chapter of this work to understand the means of particle alignment during tape casting.

3. Develop final sintered TiB_2 tapes with controlled porosity and establish the relationship between microstructure and properties for this new type of material. In order to do that, the porosity and the particle/grain alignment of the porous TiB_2 tapes will be quantified. The effect of the microstructure on mechanical properties will be investigated. Because this dissertation work is the first instance of tape casting TiB_2, the characterization of the sintered tapes is an important foundational step. In order to adapt TiB_2 to applications needing porous, functional, and complex-shaped components, the effects of significant interparticle porosity must be understood in relation to the otherwise well-known properties of fully dense TiB_2.

Chapter 2: Experimental Methods

This section of the dissertation covers the experimental methods of all of the following chapters.

2.1 Materials

2.1.1 TiB_2 suspensions

Titanium diboride powder (TiB_2; Grade F, purity ≥ 96%, diameter 3.5 μm, H.C. Starck, Germany) was used as raw material. Dolapix CE 64, which an ethanolaminic salt of citric acid, produced by Zschimmer and Schwarz, Inc. (Germany) was used as dispersant. Polyvinyl alcohol (PVA; Sigma-Aldrich) and polyethylene glycol (PEG; Millipore Sigma) were used as binder and plasticizer, respectively. The solvent for all suspensions was de-ionized water. Ethanol used in two-step mixing method, and potassium chloride (KCl, purity 99.4%), nitric acid (HNO_3, purity 65%), and sodium hydroxide (NaOH, purity 100%) used to dilute and adjust pH of suspensions for zeta potential measurements were purchased from Sigma-Aldrich. The Mylar® carrier substrate (Tape Casting Warehouse, Inc., USA) had a width of 15.2 cm and thickness of 9 mm.

2.1.2 PCN-222

Starting reagents and materials were obtained commercially and used without further purification. Zirconium(IV) oxychloride octahydrate ($ZrOCl_2 \cdot 8H_2O$, ≥99.5%) was purchased from Sigma-Aldrich (St. Louis, MO, USA), *meso*-tetrakis(4-carboxyphenyl)porphyrin (TCPP, >97%) was purchased from Frontier Scientific (Logan, UT, USA), *N*,*N*-dimethylformamide (DMF, ≥99.8%) was purchased from Fisher Scientific (Hampton, NH, USA), and difluoroacetic acid (DFA, 98%) was purchased from Oakwood Chemical (Estill, SC, USA). $ZrOCl_2 \cdot 8H_2O$ (151 mg, 0.469 mmol), TCPP (27 mg, 0.0341 mmol), and DFA (1.664 mL, 26.44 mmol, 775 Eq.) were combined in a 6-dram vial with DMF (14.5 mL) and sonicated until dissolved. The vial was placed in a 120 °C oven for 18 h, and violet PCN-222 crystals were obtained following isolation *via* centrifugation and washed ×3 with DMF and acetone.

PCN-222 samples were thermally treated in a vacuum graphite furnace (Red Devil, R. D. WEBB, Natick, MA) at 2000°C, for 5 min. This heat treatment took place in vacuum up to 1800°C, when the chamber was then backfilled with argon for the rest of the heating and dwell. The heating and cooling rates were 5°C/min.

2.2 Suspension Preparation for Tape Casting

The suspensions studied used solid loadings between 25-40 vol% (60-75 wt%) TiB_2. Dispersant content varied from 0-3 wt% with respect to the TiB_2 powder, and the binder and plasticizer studied were in the range 0-2 wt%. Suspensions were made using two mixing procedures: single-step and two-step mixing. For the single-step mixing process, suspensions were prepared first by dissolving binder in water on a magnetic stir plate set to 80°C and 350 rpm for six hours. Any plasticizer

content was added next, followed by dispersant and TiB_2 powder. To ensure homogenous suspensions, the suspensions were ball milled in a Nalgene bottle with 10 tungsten carbide (WC) balls (9 of .6 cm diameter, 1 of 1.4 cm diameter) on a roller at 60 rpm for 4 hours.

In the two-step mixing process, TiB_2 powder was added to ethanol, followed by the dispersant, and then sonicated. The beaker containing the powder, dispersant, and ethanol was placed in the oven overnight for the ethanol to evaporate. Dissolution of binder in water was carried out as in the single-step mixing method, and the dry TiB_2 powder containing dispersant was then added to the water containing binder. Finally, the plasticizer was added, the suspension was sonicated once more, and finally ball milled with the same 10 tungsten carbide balls on a roller at 60 rpm for 24 hours.

After ball milling, the tungsten carbide balls were removed, and the suspension was degassed in vacuum for 30 minutes. Following this step, the suspension was ready to be poured into the tape casting reservoir. Suspensions are labeled with three numbers representing the wt% of dispersant, binder, and plasticizer used, i.e. (2,1,2) means the suspension contained 2 wt% dispersant, 1 wt% PVA, and 2 wt% PEG.

2.3 Tape Casting

Tapes were cast on a caster (Richard E. Mistler, Inc., Model 08401x02, USA) that has a stationary reservoir and doctor blade, which are both 20.2 cm wide, and the length of the casting bed is 1.83 m. The reservoir is 725 cm^3. A motor moves the Mylar® carrier substrate at 1 cm/s. In addition, the bed temperature was kept at 21°C.

The doctor blade was adjusted by two dials to the desired height (100-500 μm in this work), and the Mylar® sheet attached to the motor was placed underneath the reservoir and blade. To cast, the vacuum was turned on low to pull out evaporating solvent into a fume hood. Suspension was then poured into the reservoir. The Mylar® continued to pull the suspension over the bed until the reservoir is empty, at which point the motor was stopped and the tape left to dry completely in the closed bed, where vacuum evacuated evaporated solvent to the fume hood.

2.4 Sintering

Tapes were sintered in a pressureless graphite vacuum furnace (Red Devil, R.D. Webb, USA). Heating took place at 5 °C/min up to 400 °C, at which point the temperature was held steady for 1 h for the removal of the small amount of organics. Heating continued at 5 °C/min up to 1500 °C, and then the rate lowered to 3 °C/min up to 2000 °C. This maximum temperature was held for 1 h before cooling back down to 1500 °C at 3 °C/min. Above 1800 °C, the furnace was backfilled with argon. The length of the samples in the x, y, and z directions was measured before and after sintering to calculate sample shrinkage.

2.5 Characterization

2.5.1 Suspensions

A Malvern Zetasizer Nano ZS (UK) was used to measure the zeta potential of TiB_2 as a function of pH. The concentration of the diluted suspensions for this measurement was 200 mg/L of TiB_2 in 10^{-2} M KCl. The suspension was sonicated with an ultrasonic horn (Fisherbrand, Model FB705 Sonic Dismembrator, USA) and then separated into six bottles. The pH values were measured with a pH probe (Thermo Scientific, Orion Star™ A221, USA) and adjusted to approximately 2, 4, 6, 8, 10, and 12 using 0.1 M nitric acid (HNO_3) and sodium hydroxide (NaOH) solutions respectively, while stirring on a magnetic plate at around 350 rpm. For each bottle, once the desired pH was reached, it was sonicated again and the pH value was confirmed with a pH probe. The bottles rolled overnight and the pH was measured a final time directly before the zeta potential measurement. The cuvette used in the measurement was a DTS1017 model, and the zeta potential was measured of at least fresh three different samples for each pH value; that is, for each pH, the cuvette was loaded, tested in the DLS, and cleaned three or more times before loading again.

Rheology measurements were performed on an AR-G2 rheometer (TA Instruments, USA). Each suspension contained 40 vol% TiB_2. Testing temperature remained steady at 25°C. About 18 mL of each suspension were tested in the rheometer with cup and bob geometry at steady shear rates from 0.01 to 1000 s^{-1}. No significant evaporation occurred over the course of the test, so a solvent trap was not used. The maximum time waited to collect each data point was 1.5 minutes. Three samples were tested for each suspension formulation, and the representative flow curves are presented.

2.5.2 Tapes

Green density was measured using geometric measurements of square samples. The sintered density was measured through Archimedes' method, and the porosity of the tapes was estimated from the relationship between density and porosity.

In this work, the angle of orientation of the feret diameter is reported as $\cos^2\Theta$ to ease comparisons between grains. Rather than defining alignment as ±45° with the cast direction (0-45°, 135-225°, and 315-360°), using the value of $\cos^2\Theta$ defines alignment in the range of 0.5-1.0, and provides a clear distribution across all possible angles.[139,140] X-ray Diffraction patterns (Bruker, XRD D8, USA) were used to estimate degree of orientation of crystals in the sintered tapes. Comparison of the intensities of the (0 0 0 1) and (0 0 0 2) peaks with the reference pattern for TiB_2 allows for calculation of the Lotgering orientation factor.[146]

The sintered samples were imaged on a scanning electron microscope (SEM; JEOL, IT-500HR). Images were taken of the tops of tapes (Figure 2B), ensuring that the direction of tape casting corresponded to the horizontal axis of the image. These microstructural images were then digitally

analyzed in ImageJ (version: 1.51j8, Wayne Rasband, National Institute of Health, USA). The color channels were split and the threshold adjusted to isolate the grains in the image. Then a watershed filter was applied and the ImageJ Analyze Particles function executed to measure feret angles of all particles larger than 0.01 μm^2; the feret angles were reported as the angle between the longest axis of a grain with the horizontal of the image, therefore the direction of tape casting. At least four images were analyzed for each sample, and approximately 1700 grains per image. Energy dispersive X-ray Spectroscopy (EDS JEOL Inc., Peabody, MA, USA) was conducted on the composites to identify the presence of the high-aspect ratio particles (different composition than the matrix).

The Bruggeman Estimator Mathematica program (ETH Zurich, version v1.0, Switzerland) was used to approximate the tortuosity of samples. By inputting an SEM image of the top surface and side view of the samples, the program allows the user to identify particles or grains using an elliptical selection tool. Once at least 10 have been identified, the program creates a virtual particle population and uses Differential Effective Medium (DEM) approximation to estimate the Bruggeman exponent in three directions based on particle shape and orientation. The Bruggeman Estimator relies on the Bruggeman relation, a simple estimation of the tortuosity (τ) based on porosity (ε) and the Bruggeman exponent (α).

$$\tau = \varepsilon^{-\alpha} \qquad \text{[Equation 4]}^{147}$$

The Bruggeman relation is widely accepted to be an accurate estimation tool.[79,147] By using Differential Effective Medium (DEM) approximation to create a virtual population of pores and grains based on SEM images of the top and cross views of a potential "electrode," the Bruggeman estimator calculates the Bruggeman exponent in the x, y, and z directions. The porosity of a sample can be measured empirically and Equation 4 can then be used to calculate the tortuosity.[148]

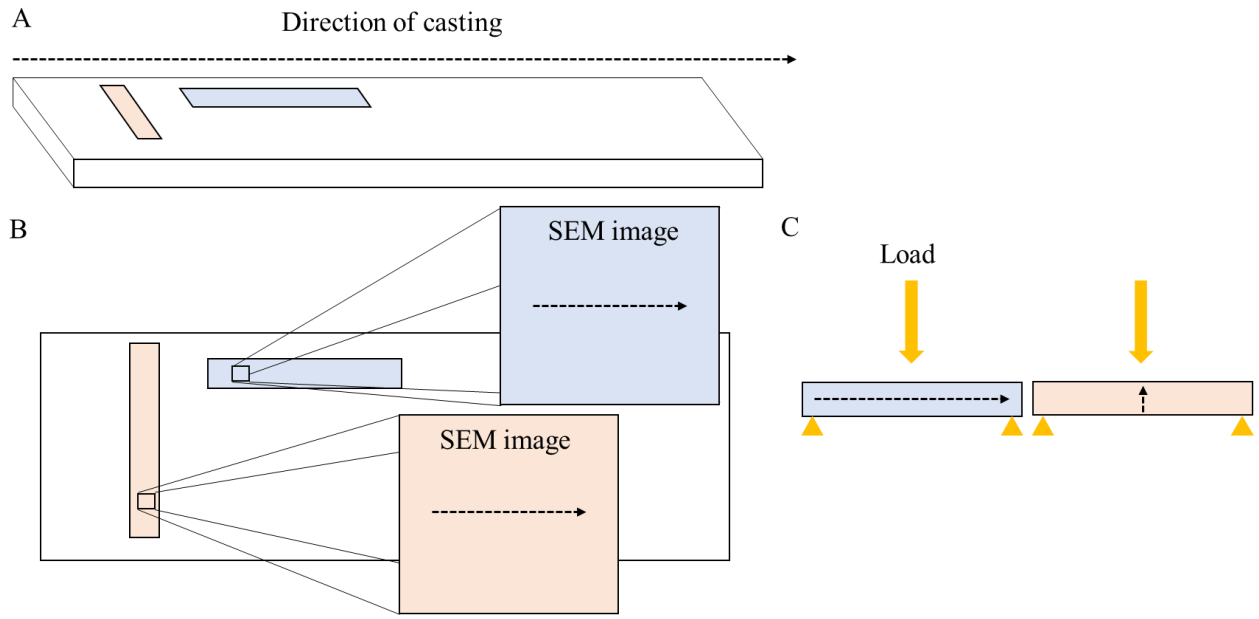

Figure 2: (A) Schematic of tape cast TiB_2 indicating cast direction in relation to SEM images (B) and application of load during 3-point bend testing (C).

Three-point bend tests were performed on the green tapes according to ASTM C1161-18 (Instron, Universal Testing Machine Model 5944, USA) using a 10 N load cell and a speed of 5 mm/min. Samples were cut with a razor to 45 mm long, 4 mm wide rectangles (configuration B), with depths measured with calipers accurate within 0.01 mm. The support spans for this test were 40 mm apart. At least ten samples were tested for each condition.

3-point bend tests of the sintered tapes were performed according to ASTM C1161-18 (Figure 2C). A 500 N load cell was used and the test speed was 5 mm/min. Sintered samples were cut with a razor into rectangles (45 mm long, 4 mm wide; configuration B in ASTM C1161-18), with thickness measured by calipers accurate within 0.01 mm. the support spans for this test were set 40 mm apart.

Fracture toughness was also measured on the 3-point bend apparatus of this equipment, but with 20 mm support spans and 22 mm specimens. The pre-crack was created and measured using Micro Vickers Hardness Tester (Phase II, model no. 900-390, USA). The Vickers diamond indenter was used, the load was 2.94N, and the average depth of the pre-crack was 44µm. The calculation of fracture toughness was performed according to ASTM C1421-18.[149]

2.5.3 PCN-222

Thermal analysis was performed in a differential scanning calorimeter/thermogravimetric analyzer (DSC/TGA, Netzsch, STA 449 C Jupiter, Germany), up to 1400°C in argon atmosphere, at 5°C/min using alumina crucibles.

Particle morphology (before and after heat treatment) was characterized using a LEO Zeiss 1550 field-emission scanning electron microscope (SEM, Carl Zeiss, Oberkochen, Germany). The secondary electron detector, backscatter electron detector, and a combination of both were utilized to produce images. Samples were mounted with carbon paint.

Energy dispersive X-ray spectroscopy analysis was preformed using a JSM-IT500 InTouchScope SEM (EDS, JEOL Inc., Peabody, MA, USA). The heat-treated powdered sample (~5 mg) was dispersed in 1 mL acetone *via* sonication for 30 minutes. One droplet of the suspension (~100 µL) was cast on the sample stage, which was then submitted to the EDS analysis.

Crystallinity and phase purity of PCN-222 (before and after heat treatment) and graphite (for comparison) were determined *via* PXRD measurements on a Rigaku Miniflex diffractometer (Cu Kα radiation $\lambda = 1.5418$ Å). Samples were loaded on to a Rigaku Si510 holder disc and analyzed at a 0.05° resolution 1.0°/min continuous scanning mode over $2\theta = 2-50°$.

High-resolution TEM images of PCN-222 before and after heat treatment were obtained *via* JEOL 2100 TEM (JEOL Inc., Peabody, MA, USA). Powdered sample (~5 mg) was dispersed in 1 mL ethanol by sonication for 30 mins. Then, 20 µL of the suspension was cast on a lacey carbon TEM grid (Electron Microscopy Sciences, Hatfield, PA, USA). The grid was air-dried before submitting to TEM. Diffraction patterns of selected areas were captured using a dedicated diffraction camera built in the system.

Raman spectroscopy was conducted on a WITec 500 alpha confocal Raman microscope (WITec, alpha 500, Germany) equipped with a 10x objective. Frequency calibration was achieved using the 520.5 cm^{-1} of silicon. Laser excitation (~1 mW at the sample) was provided by a 633 nm He–Ne laser. Spectra were obtained as an average of 6 accumulations of 10s each.

X-ray photoelectron spectroscopy (XPS, PHI, Versa Probe III, Chanhassen, MN, USA) measurements were performed on a PHI VersaProbe III scanning XPS microscope equipped with a monochromatic Al K-alpha X-ray source (1486.6 eV). XPS Spectra were acquired over a 100 µm × 100 µm sample area with an emission angle of 45°. Surface charging was compensated by low energy electron flood and low energy Ar + flood. All binding energies were referenced to a carbon peak at 284.3 eV.

Chapter 3: Cost-effective suspension formulation for flexible TiB_2 tapes

The work in this chapter was presented virtually at the 46th International Conference and Expo on Advanced Ceramics and Composites, (S18: Ultra-High Temperature Ceramics):

Shirey, Kaitlyn and Tallon, Carolina. "Cost-effective suspension formulation for flexible TiB_2 tapes." International Conference and Expo on Advanced Ceramics and Composites. Oral Presentation (Virtual). January 25, 2022.

It was published in the International Journal of Applied Ceramic Technology in 2023. Reference:

Shirey, Kaitlyn, and Tallon, Carolina. (2023). "Cost-effective suspension formulation for flexible TiB_2 tapes." International Journal of Applied Ceramic Technology. https://doi.org/10.1111/ijac.14322

3.1 Introduction

Suspensions for tape casting typically consist of ceramic powder, solvent, dispersant, wetting agent, binder, and plasticizer.[96,150] Aqueous solvents are more environmentally friendly and less expensive, drawing more attention away from the fast-drying nonaqueous options,[98] which are commonly favored for their low surface tension and the reduced risk of cracks.[108,151] While choosing an aqueous suspension may limit the materials somewhat because of incompatibility between certain non-oxides and water, there are still many non-oxides and oxides that can be tape cast in aqueous suspensions.

It is best to use as few additives as possible, as all organic components will decompose during pyrolysis of the tape, and lowering the volume of organics removed during this step lowers the potential for defects to form during drying or sintering.[96,99] Fewer additives also guarantees a more cost-effective manufacturing route and easy translation to industrial set-ups. One of the lowest additive contents reported is around 15 vol% of total suspension (6 wt% with respect to solids) for Al_2O_3/Y-TZP tapes,[102] but most tape cast ceramics are reported to contain over 15 wt% additives with respect to solids.[96,98,99] Up to 40 wt% of the suspension (88 wt% with respect to powder) has been reported to be additive content (in a Gd-CeO_2 tape for solid oxide fuel cells),[152] which increases production costs as well as the potential for defects. Density and tensile strength have been evaluated as a function of binder and plasticizer content to identify the balance in maximizing these properties while minimizing additive content.[96]

In this work, titanium diboride suspensions are formulated with as few additives as possible for tape casting to ensure cost-effectiveness while preserving tape quality. This study will analyze the relationship between processing parameters and the quality of TiB_2 tapes. Tapes will be compared microstructurally and mechanically to determine the most effective parameters and compositions.

3.2 Results and Discussion

3.2.1 Effect of additives on interparticle forces

To ensure a well-dispersed suspension, the forces on particle surfaces must be repulsive.[89] The surface potential would be the most accurate measurement of the charges on the surfaces of particles, but because this is too difficult to measure, the zeta potential is normally used instead.[153] The zeta potential is a measurement of the slipping plane of the Stern layer of a charged particle moving in a liquid and is an approximation of the surface potential, giving a relative quantitative representation of the repulsion between particles in suspension.[12,153] Measuring the zeta potential at different pH levels allows for the approximation of the electric charge on the surface of the particles; the larger the magnitude of this force is, the stronger the repulsive forces will be, and the more separated and dispersed the particles will be in suspension.[153] In general, working in acidic suspensions translates into positive charges at particle surfaces, and working on basic suspensions results in negative charges.[90] Figure 3A shows the zeta potential between pH 2-10 for TiB_2 suspensions with varying dispersant content. The isoelectric point (IEP) is the pH level at which the zeta potential is zero, meaning that most of the particle surfaces have equal amount of positive and negative charges charge.[10] The IEP of TiB_2 powder is approximately at pH 3.5. TiB_2 is reported in literature to have an IEP of 4.5,[154] but the difference in the source of the powder and any potential impurities or surface species ratio, like oxides on the particle surfaces, can cause this difference in IEP. As with other non-oxides, the surface of TiB_2 has a small percentage of titanium oxide (TiO_2), reported by the manufacturer to be less than 2.5%, and it is likely that it is on the surface of the particles. This amount determines the electric double layer (and therefore the zeta potential results) and how the dispersant adsorbs on the surface.

The selected dispersant provides electrosteric stabilization, a combination of electric and steric, to the TiB_2 particles. Dolapix is an anionic dispersant, meaning that the functional groups change to anionic groups in water, and the IEP shifts to the left from pH 3.5 to 2.5.[155] This shift of the IEP also confirms that the dispersant is specifically adsorbing on the surface of the particles.

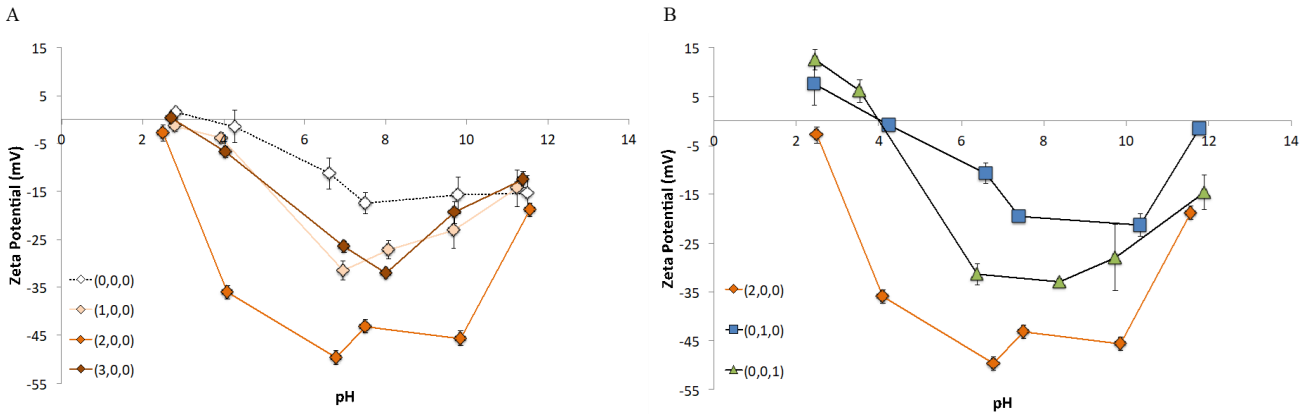

Figure 3: Zeta potential of TiB_2 suspensions containing (A) varying dispersant content; (B) each additive.

The (1,0,0) sample has a lower zeta potential than that without any dispersant, but 1 wt% is not enough to maximize the repulsive forces acting on the particles. The dispersant is specifically adsorbing on the particle surfaces, but there is not enough dispersant to fully saturate them. At 3 wt% dispersant, the zeta potential is almost the same as the (0,0,0) sample, meaning that with too much dispersant, the repulsive forces are reduced significantly from the (2,0,0) case. This is possibly because there is more dispersant present than there is surface area for it to attach on particles' surfaces, and the free dispersant is weakening the repulsion of the attached fraction.

The lowest zeta potential value occurs at approximately pH 6 for the sample containing 2 wt% dispersant. Through the pH range 6-8, the 2 wt% dispersant sample has a zeta potential almost 20 mV lower than the 0, 1, and 3 wt% samples. The IEP does not shift further with increasing dispersant content. These results are in good agreement with literature, where it was described that dispersant content affects electronegativity of particles surfaces without further changing the IEP.[154] Based on these results, all tapes were prepared with suspensions with just 2 wt% dispersant.

Similar zeta potential measurements were taken to determine whether the binder (PVA) or plasticizer (PEG) specifically adsorb on the surface of the particles and affected the IEP or compete with the dispersant adsorption onto the particle surface. As shown in Figure 3B, the IEP remains almost exactly at pH 4 when PVA or PEG are added, meaning that each additive does adsorb to the particle surface. Therefore, the binder and plasticizer are competing with the dispersant to adsorb on the available surfaces, which necessitates the two-step mixing method discussed later.

The inclusion of PVA does not change the magnitude of the zeta potential significantly, but PEG increases this magnitude by up to 20 mV. The measurement indicates that PEG seems to successfully adsorb onto the particle surfaces. The IEP does not shift with addition of PEG, but the zeta potential gets significantly lower because the PEG is a large molecule, offering greater steric

repulsion and greater negative charge to repel other particles. It is promising that even 1 wt% PEG has such a significant effect on the zeta potential because the goal is to produce enough repulsive forces with as few additives as possible. Varying the binder and plasticizer content from 1-2 wt% means that the total amount of additives used from this point forward is 4-6 wt% with respect to the TiB_2 powder, which is far below what is reported in the literature for most other UHTC tapes. The percentages of the different additives that specifically adsorb onto the surface of the particles are dependent on the type and size of TiB_2 powder used.

3.2.2 Effect of additives on rheological behavior

The suspension stability formulated with these additives was assessed using rheological measurements. Rheological information also provides information about dispersion quality. Shear thinning behavior is ideal for tape casting because it allows the suspension to flow while being spread onto the substrate (when the shear increases), but immediately after casting suppresses further uncontrolled flow of suspension (when the shear decreases or is removed) as well as sedimentation of the ceramic particles.[96,98,106] A high viscosity is typically indicative of the presence of aggregates, showing that the particles are not individually dispersed and are resisting flow,[89] while low viscosity promotes a uniformly smooth tape surface and homogeneity of the particle packing.[96,99] Figure 4A shows viscosity as a function of shear rate for each additive. The dotted vertical line represents the shear force experienced by the suspension during the process of tape casting conditions, estimated as the substrate velocity divided by the blade gap height[155] (40 s^{-1}). The formulation (0,1,0) is not shown, because a suspension formulated with PVA and no dispersant formed a putty-like mass which is unable to flow for rheological testing or tape casting. The suspension with no additives has significantly lower viscosity than the others, with some slipping behavior at high shear rates. While a suspension with no additives has much lower viscosity at the critical shear rate, the additives are required to guarantee the functioning of the tape casting process: at such a low viscosity, the suspension has too low a viscosity to form a uniform tape; the pressure of the suspension in the reservoir pushes it out under the doctor blade faster than the shear forces of the substrate moving under the doctor blade can shape them, rendering the control of the substrate velocity useless.

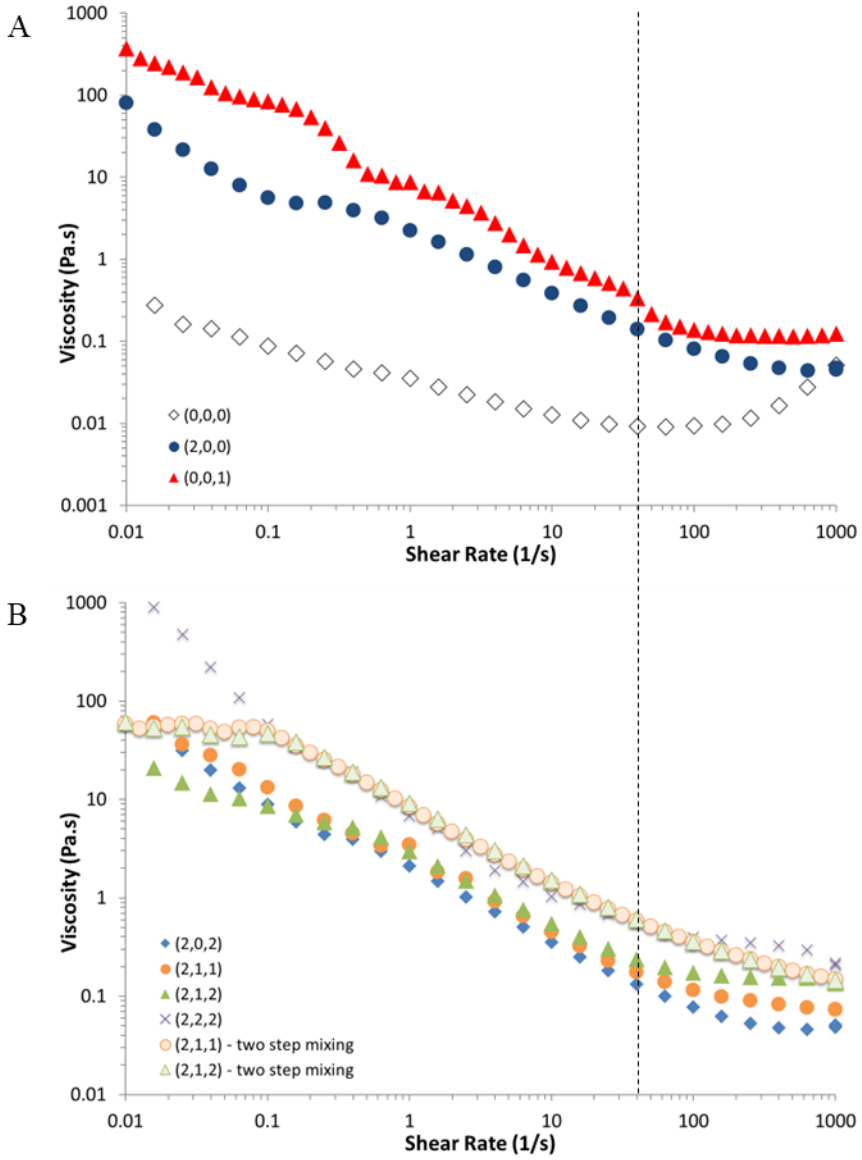

Figure 4: Rheology of (A) each additive individually. Note that (0,1,0) is not present because without dispersant, the binder makes the suspension too thick to pour; (B) combinations of additives used for tapes. Dotted lines indicate the shear force produced under the tape casting speed used in this study.

To determine the best suspension composition and the boundaries for creating a viable tape, many different combinations of dispersant, binder, and plasticizer were tested; the most representative and promising results are discussed here. Including more than one additive in the suspension has a synergistic effect, as shown in Figure 4B. Suspensions formulated as (2,0,2) is represents a lower boundary for the viscosity at high shear rate, at which the suspension evacuates the reservoir faster than the carrier substrate can pull it under the doctor blade. In this case, there is no control over the thickness of the tape. Similarly, (2,2,2) is included to define the upper boundary, where the tape produced at this velocity is too thick, does not spread properly because it gets stuck in the reservoir,

and makes a tape with visible aggregates on the surface. The remaining samples shown lie between these two extremes: compositions (2,1,1) and (2,1,2), including both the single- and two-step mixing processes. Suspensions with 2 or 3 additives have lower and more homogeneous viscosity than those with only 1. Because of the interactions between additives, a two-step mixing method is introduced at this stage. The two-step mixing method ensures that there is no competition between additives to adsorb to the particles' surfaces by allowing dispersant to specifically adsorb to the particle surface first, then binder and plasticizer to enter the suspension separately, maximizing suspension stability and homogeneity. Figure 4B shows that those suspensions mixed in two steps exhibit very similar rheological behavior, showing that regardless of the amount of plasticizer, the dispersion quality remains constant. Studies of various material systems report suspension viscosities around 2-4 Pa.s at shear rates near 100 s^{-1}.[96,105,155] The viscosity of the TiB_2 suspensions in this study are an order of magnitude lower, between 0.08-0.4 Pa.s for the same shear rate and have significantly lower additive content; other authors have reported additive contents of 6 wt% with respect to solids to 40 wt% with respect to total suspension. The raw data reported in these papers was to convert their additive content to weight percent with respect to powder. The tapes in this paper contain 4-6 wt% additives with respect to the powder vs 6-88 wt% with respect to powder[96,102,105,155]. Tape casting of zirconium diboride was accomplished with 18-25 % based on powder volume (vs 16.25 vol% in this work).[99]

A tape is generally considered successful based on uniformity, flexibility and mechanical integrity, and its ability to be removed from the substrate on which it was cast. The uniformity involves surface devoid of bubbles, cracks, and agglomerates with a smooth overall appearance. Because a tape must be capable of being handled, either by a gloved hand or tweezers, the tapes must be removable from the substrate. Rolling the tapes to visually assess the flexibility and identifying the peeling behavior from the Mylar® provided the information needed about whether samples could be removed from the substrate in significantly large pieces for further study. The suspension composition, preparation, and homogeneity are known to be dominating factors in ensuring these qualities in the final tape. For example, if the additives like binders or plasticizers are not fully incorporated with the suspension, they may appear as bumps on the surface of the cast tape. Table 3 summarizes these qualitative attributes of all the relevant tapes in this work as a function of several parameters associated with the suspension formulation and casting: mixing method, solid concentration, and blade height.

Table 3: Qualitative comparison between tapes with different processing parameters.

Parameters		PVA content (wt%)	PEG content (wt%)	Qualitative assessment	Sample label
Mixing method constants • 2 wt% dispersant • 25 vol% TiB_2 • 250 μm blade height	Single-step mixing	0	2	Casts into very non-uniform shape. Does not roll at all. Peels easily but is very brittle	
		1	1	Rolls but cannot peel off pieces without breaking into flakes	
		1	2	Rolls but cannot peel off pieces without breaking into flakes	
		2	2	Too viscous to cast a tape	
	Two-step mixing	1	1	Front half stiff: rest of it rolls. Rolling facilitates peeling but too much rolling cracks it	
		1	2	Front half stiff; rolling causes some cracking. Does not roll easily but peels easily	
Solid concentration constants • 2 wt% dispersant • Two-step mixing • 250 μm blade height	30 vol%	1	1	Front half stiff but peels easily. Pieces that peel off do roll	T1
		1	2	Rolls well. Peels very easily.	T2
	40 vol%	1	1	Rolls very easily along entire length but not as easy to peel as 30 vol%	
		1	2	Rolls well and is very flexible. Cannot peel at all	
Blade height constants • 2 wt% dispersant • Two-step mixing • 30 vol% TiB_2	100 μm	1	1	Rolls well but pieces do not peel easily	
		1	2	Rolls but cannot peel off pieces without breaking into large flakes	
	500 μm	1	1	Rolling causes much cracking. Pieces do not peel across width of tape	
		1	2	Stiff; cannot roll. Can easily peel in one large piece	

3.2.3 Effect of casting parameters

In the single-step method, that competitive adsorption between the dispersant and binder weakened the effectiveness of both additives in the suspension. There were more likely to be agglomerates in these samples regardless of additive content, while the viscosity did depend on additive content. Tapes with 1 wt% binder were able to roll without cracking but were not able to peel from the substrate at all without breaking up into small flakes. These samples were effectively useless.

For suspensions made with the two-step method, there was no variation in viscosity at the same shear rate even with different compositions. Removing competitive adsorption allowed suspensions to maintain stability regardless of varying additive content. Even though the slightly higher viscosity values at high shear rate compared to the single-step mixed suspensions suggests that the two-step mixing method produces less stable suspensions, the tapes created are of better quality. Tapes cast with the two-step mixing method, all other parameters kept constant, had much stiffer end products. While they did not roll as readily as the single-step mixed tapes, the tapes were able to be peeled into large pieces without damaging them.

Investigation of solid concentration on the quality of the tapes showed that increasing to 30 vol% TiB_2 improved the rolling ability compared to the 25 vol% samples. Those with 1 wt% plasticizer still had some stiffness, but the pieces which peeled off the Mylar® were flexible. Doubling the plasticizer to 2 wt% allowed for excellent rolling and peeling qualities. The largest solid concentration explored in this study, 40 vol% TiB_2 proved too high; though the rolling ability continued to improve, the peeling ability degraded at such a high concentration. Overall, rolling improves with higher solid concentration, and peeling ability deteriorates. This may be because at lower concentration, there are fewer particles to bear the load that bending or rolling imposes on the tape. At higher concentration, there is more binder and plasticizer in comparison with the solvent, and the additives may not be as homogenously distributed, making the plasticizer less effective in aiding the peeling process. The samples with 30 vol% TiB_2 strike a balance that allows for usable tapes regardless of the plasticizer amount.

Setting the blade height at 100 μm, tapes roll easily without damaging, but are not solid enough to peel without breaking the pieces. Conversely, at 500 μm, samples are stiffer and rolling is more likely to cause cracks in the tape. However, these tapes are much easier to peel from the substrate in large pieces, although they may be stiff. The tapes cast at 250 μm are both more flexible and more durable compared to the other blade heights; they are both able to roll at least a little, and can be peeled without completely breaking down. Typically, tapes are cast with blade gaps up to 1000 μm[152] but most reports list the blade gap between 150-500 μm, and furthermore do not adjust additive content for different blade gaps. Shrinkage is known to be greater for tapes with lower solids loading, but in the literature there does not appear to be a correlation between additive

content and tape thickness.[96,105,155] The tapes studied in this paper do tend to be thicker with 1 wt% plasticizer than 2 wt% (Table 4).

Table 4: Tapes cast from suspensions using two-step mixing method, formulated with 2 wt% dolapix, 1 wt% PVA, 30 vol% TIB2, cast at 250 um, with different plasticizer amount.

Tape	T1	T2
PEG content (wt%)	1	2
Average green density, measured geometrically (% theoretical)	50±1.2	47±0.9
Average thickness (μm)	375 ± 46	325 ± 64
Average strain at failure (%)	0.76 ± .19	.37 ± .03
Average flexural strength (MPa)	3.02 ± 1.7	7.22 ± 1.5
Average Young's Modulus (GPa)	.39 ± .18	1.96 ± .42

Based on these results, the tapes further studied in this paper utilize the two-step mixing method, contain 30 vol% TiB_2, 2 wt% dispersant, 1 wt% PVA, and are cast at 250 μm, and two amounts of plasticizer, labelled T1 (1% plasticizer) and T2 (2% plasticizer). The uniformity of the tapes viewed with the naked eye show no visible agglomerates or rough regions (Figure 5). The smooth surfaces indicate that the suspensions used had the proper shear-thinning behavior. Examples of the ability of the tapes to roll and peel are also pictured. The success of these tapes is due in part to the good particle packing and homogeneity of the green bodies. Figure 6 shows SEM images of T1, the microstructure of which is representative of T2 as well. There are no defects visible at high magnification. The green densities of both tapes are 50 and 47% of the theoretical density for T1 and T2, respectively (Table 4), which is to be expected of a green body prepared with 30 vol% suspension and no additional consolidation mechanism force.[123] In the literature, 33 vol% solids loading produced 45% dense Gd-CeO_2 green sheets,[152] and most other published values match this trend, with green densities typically falling under 60% theoretical.[99,102,152,156,157] ZrB_2 green tapes with up to 48% density were produced with 45 vol% suspensions.[99] In general, the higher the solids loading, the higher the green density of the tapes.

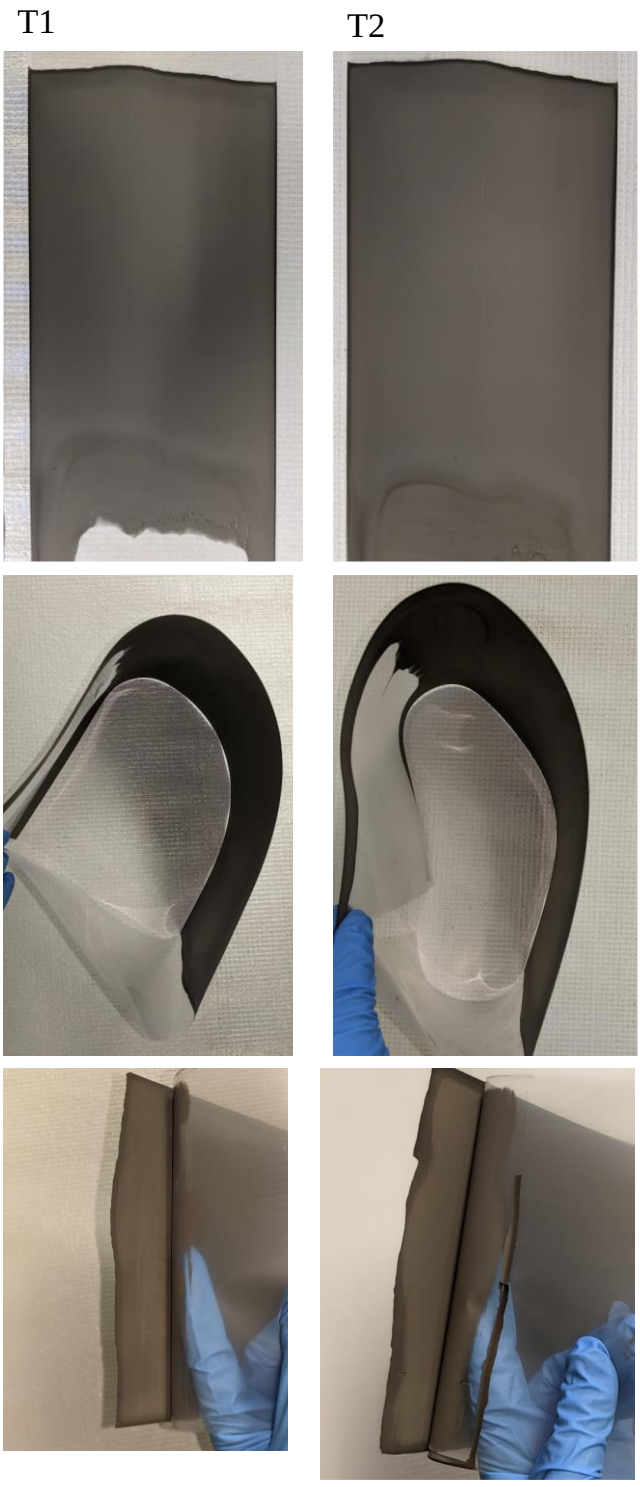

Figure 5: Photographs of successful T1 and T2 tapes formulated with minimum additives after casting and drying, shown rolling and peeling from the substrate. Tapes are 15.2 cm wide and approximately 30 cm long.

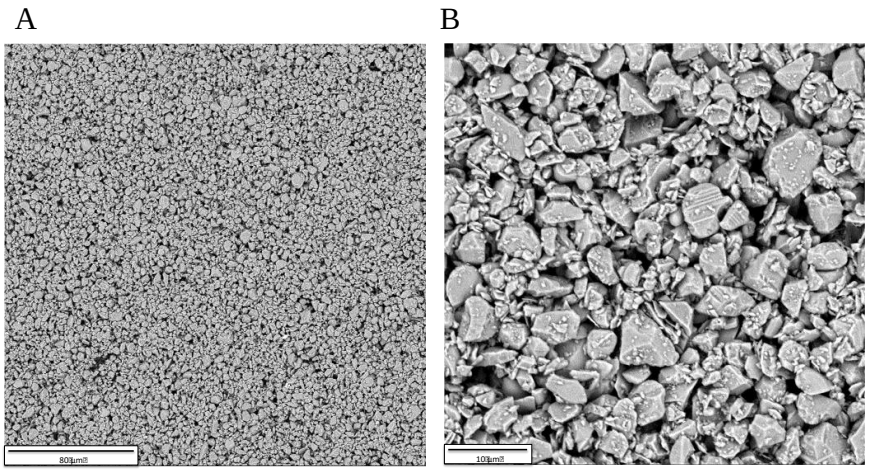

Figure 6: Representative SEM images of green tape T2 at (A) low and (B) high magnification. These images are representative of the particle packing and homogeneity of all green tapes studied.

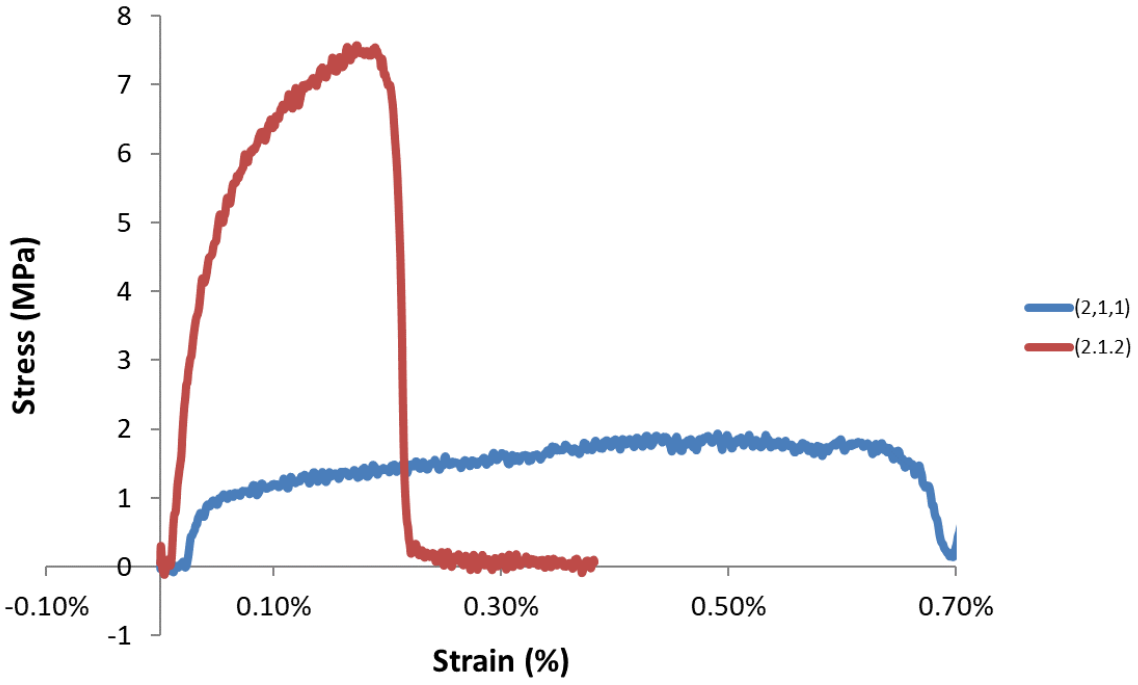

Figure 7: Representative stress strain curves for three-point bending tests for T1 and T2 tapes, for each of which ten samples were tested.

3.2.4 Effect of plasticizer content on mechanical properties

Several specimens of green T1 and T2 were mechanically tested. The results of the three-point bending tests on these two samples can be seen in the representative stress strain curves (Figure

7). The average stress and strain at fracture for each sample (Table 4) show that T2 has the greater strength and strain allowance. Young's Modulus for T2 averages at 1.96 GPa, while for T1 it is only about 0.39 GPa. The increased plasticizer content in T2 provides greater resistance to permanent deformation, exhibited in the significantly higher Young's Modulus. Mechanical data for green tapes is not as readily available in the open literature as for sintered tapes. Alumina green tapes (14 wt% additives, blade gap 400 μm) have been reported to have Young's Modulus of 40 MPa.[157] Green YAG-Nd:YAG tapes were in the range of 160-500 MPa, depending on additive content (40-50 vol% additives, tape thickness 100 μm).[156] For comparison, T2 has 16.25 vol% additives calculated in the same way as in Belon et al.'s work. To the best of the authors' knowledge at the time of this study, no reports of single layer UHTC green tape mechanical properties could be found in the open literature.

The process and suspension formulation described in this study is competitive with other ceramic green tape formulations and contains lower additive content. The nearest reported value is 6 wt% with respect to powder[102] (vs 5 wt%), and most reports list additive content of at least 15 wt%. The significantly lower amount of additives accounts for the much lower Young's modulus of the TiB_2 tapes. At this minimum additive content, the tapes are easily handled and can be further studied for their use in filtration and flow-through applications, as discussed in the introduction. In particular, battery electrodes require through-connected porosity for the completion of charge and discharge processes. Active components must diffuse through the pore network, which must be tunable in size and can be quite complex, involving mutliple pore scales and directional tortuosity.[73,78] Multiple electrochemical and transport processes occur within the pore network, making the microstructure of the electrodes of the utmost importance.[81] TiB_2 tapes with designable pore networks for ion diffusion could be the next generation of Li-ion or Li-air battery electrodes. Producing such ceramic bodies with minimum additive content could help keep costs down and reduce the risk of defects to improve reliability. Furthermore, formulating suspensions as described in this paper, by optimizing the interparticle forces and ensuring shear-thinning behavior, should be robust enough to adapt for the use of sintering aids or other materials, if dense components were to be pursued.

3.3 Conclusions

Successful TiB_2 tapes have been produced using aqueous suspensions with minimum amount of additives, 5 wt% with respect to the powder. Compositions including varying additive content were investigated to ensure highly repulsive interparticle forces, shear thinning behavior, and uniform microstructures. The two-step mixing method was integral to preventing competitive adsorption of additives and allowing for a stable, well-dispersed suspension. The optimal dispersant and binder content were 2 and 1 wt%, respectively. Tapes cast with 30 vol% TiB_2, a 250 μm blade height, and at a speed of 1 cm/s had good reproducibility, uniformity, and the ability to roll and peel from the Mylar® without disintegrating or severely cracking. To determine the optimal

plasticizer content, 3 point bending tests determined the Young's modulus of the green tapes. T2, containing 2 wt% PEG, had quintuple the Young's modulus (1.96 GPa) compared to T1, containing half the amount of plasticizer. Potential applications for porous TiB_2 tapes include battery electrodes, thermal protection systems, and catalyst supports.

Chapter 4: Preparation of ZrC embedded carbon rods via thermal decomposition of metal organic frameworks

The work described in this chapter has been presented at the Materials Science and Technology Conference:

Shirey, Kaitlyn, Bonnett, Brittany, Yang, Xiaozhou, Morris, Amanda, and Tallon, Carolina. "Preparation of ZrC embedded glass-like carbon rods via thermal dcomposition of metal organic frameworks." Materials Science and Technology Conference. Columbus, Ohio. Oral Presentation. October 20, 2021.

It was also published in Materialia in 2023. Reference:

Shirey, K., Bonnett, B., Yang, X., Morris, A., and Tallon, C. (2023). Preparation of ZrC embedded carbon rods via thermal decomposition of metal organic frameworks. Materialia, 28, 101716. https://doi.org/10.1016/j.mtla.2023.101716.

4.1 Attributions

This chapter is part of a research collaboration with Dr. Amanda Morris and two of her group members (Dr. Brittany Bonnett and Mr. Xiaozhou Yang), in the Department of Chemistry at Virginia Tech. Dr. Brittany Bonnett and Xiaozhou Yang completed the synthesis of the PCN-222 MOFs used in this work and wrote the corresponding section. Kaitlyn Shirey conducted all the experiments to transform the PCN-222 into ZrC-carbon material. Dr. Bonnett conducted the PXRD, and Kaitlyn Shirey did the interpretation of this data. Mr. Yang was responsible for the EDS mapping, TEM imaging, and TEM diffraction, along with Elizabeth Cantando and Sheryl Singerling of the Nanoscale Characterization and Fabrication Lab (NCFL). Most of the data interpretation from these techniques was done by Kaitlyn Shirey with assistance from the members of the NCFL. Dr. Weinan Leng performed the Raman spectroscopy, Dr. Xu Feng and Dr. Kristin Knight performed XPS, and these individuals assisted with data interpretation for their respective techniques.

4.2 Introduction

The UHTCs are difficult to synthesize, especially in complex particle shapes. While there are some reports of carbothermal reduction producing ZrC particles as low as 1400°C, Jain *et al.* confirmed the presence of oxygen in the crystal lattice at this temperature in the form of zirconia and zirconium oxycarbons.[142] Sacks *et al.* showed that heat treatment of precursors at 1800°C produced ZrC with less than 0.1 weight % oxygen. The particles were estimated to be about 57 nm, assuming dense, non-contacting, mono-sized spheres.[158] However, Cetinkaya *et al.* claimed that even this

temperature produces coarse, low purity ZrC particles.[159] high processing temperatures are required to ensure a pure final product.[159]

Unfortunately, ceramic nanowires and whisker-shaped particles incur even greater production costs than spherical morphologies, and the size of these particles is reported to be difficult to control in mass production.[160] The production of ZrC particles with high aspect ratios has been investigated by thermal evaporation (diameter 1.3-2.9 μm, length 260-580 μm),[161] chemical vapor deposition (diameter 1-3 μm, length 20-150 μm)[162], and microwave hydrothermal processing (diameter .1-2 μm, length 5-30 μm)[163] but none has emerged as the preferred route of production due to the need for catalysts.[161] Catalysts inhibit the final product's applicability to high temperature environments because the catalyst remaining in the final product is highly reactive. Overall, these routes have shown mass production of the nano-sized ZrC with high aspect ratio to be very challenging.[160]

Synthesis of UHTC particles using metal organic frameworks (MOFs) presents an opportunity for more simple production of high aspect ratio ZrC particles in a potentially more cost-effective process. MOFs are crystalline coordination polymers composed of multidentate organic linkers bridging metal nodes to form one-, two-, or three-dimensional porous structures.[164–167] These materials are marked by high surfaces areas, good chemical and thermal stability, and tunable particle size and geometry.[168] The robust nature and multifunctional characteristics of MOFs have placed them on the forefront of many applied research fields, including gas separation and storage,[169–172] biomedical applications,[173–175] catalysis,[176–178] light harvesting,[179–181] and carbon dioxide capture,[182–185] among others.[186,187] MOF-derived carbon nanostructures have many applications, including catalysis, electrochemical energy storage, Li-ion battery anode materials, and supercapacitors.[188–195] [50,51] This study utilizes PCN-222 (chemical formula $Zr_6(\mu_3\text{-}O)_8(OH)_8(TCPP)_2$, where TCPP = *meso*-tetrakis(4-carboxyphenyl)porphyrin)), a rod-shaped MOF containing Zr (diameter ~1 μm, length 5-10 μm).

In this work, the MOF PCN-222 is heat treated and the resulting high aspect ratio particle is characterized.

4.3 Results and Discussion

PCN-222, a zirconium-based porphyrinic metal-organic framework, is marked by its anisotropic growth pattern and its 37 Å mesopores flanked by 13 Å micropores. The Zr_6O_8 nodes are linked in an 8-connected fashion *via* coordination with *meso*-tetrakis(4-carboxyphenyl)porphyrin (TCPP) ligands (Figure 8). During solvothermal synthesis of PCN-222, difluoroacetic acid (DFA) is used as a modulator, which is a monocarboxylic acid that competitively binds to the Zr_6O_8 nodes to slow down particle growth and promote crystallinity. A porous 3-dimensional framework results,

with anisotropic growth and channels aligned down the *c*-axis. XPS analysis indicates no evidence of chlorine present after synthesis.

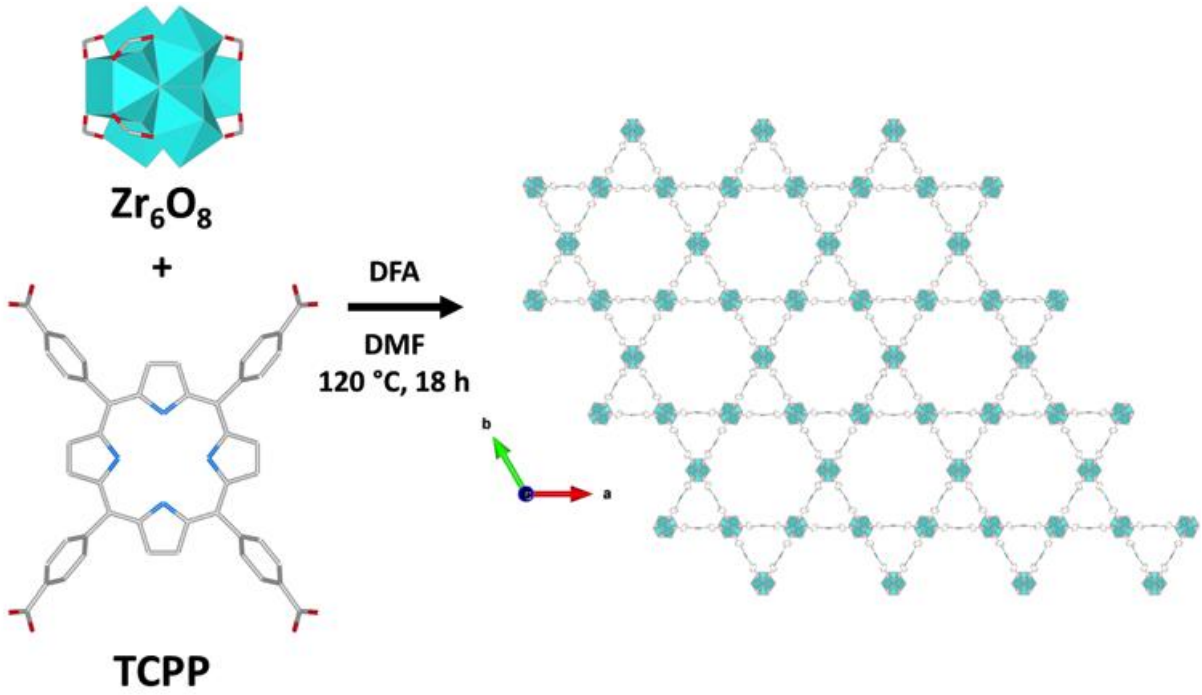

Figure 8: Synthetic schematic of PCN-222. A Zr_6O_8 node is combined with a TCPP ligand with difluoroacetic acid (DFA) modulator in DMF solvent for 18 h at 120 °C to form a three-dimensional MOF network.

Thermogravimetric analysis was performed on PCN-222 from room temperature to 1400 °C (Figure 9). From room temperature to 270°C the loss of solvent encapsulated in the MOF pores during synthesis is observed. Decompositions at 327 and 470 °C are attributed to dihydroxylation of the Zr_6 node and TCPP degradation, respectively.[196,197] Above 500 °C, the organic components of the original MOF have burned out. Beyond this temperature most of the reactions occurring are inorganic in nature, such as the reaction between Zr and C and the subsequent phase transformation. Complete carbothermal reduction of ZrO_2 and C into ZrC can occur as low as 1400°C,[198] just before which the TGA shows an additional slight mass loss indicative of the transformation. The powder's original red color becomes dark gray after heat treatment, confirming the phase change.

The overall mass loss after 1400°C treatment was similar to the mass loss noted after the 2000°C treatment, indicating that no further reactions took place in the powder, just changes of phase, crystallinity, and stoichiometry.[199]

According to the C-Zr the phase diagram published by Guillermet,[200] heating the sample with an atomic fraction of C greater than .39 should result in a ZrC_x phase accompanied by some form of

carbon.[201] ZrC_x is stable at a wide range of x values, from 0.63-0.98,[202] with oxygen and nitrogen impurities filling vacancies.[203] The greater the temperature during heat treatment, the fewer of these impurities that remain.[199] Organic components of the original MOF, which have not fully burned out, could be present in heat-treated PCN-222, but the high temperature of the heat treatment likely results in stoichiometric or near-stoichiometric ZrC.[199]

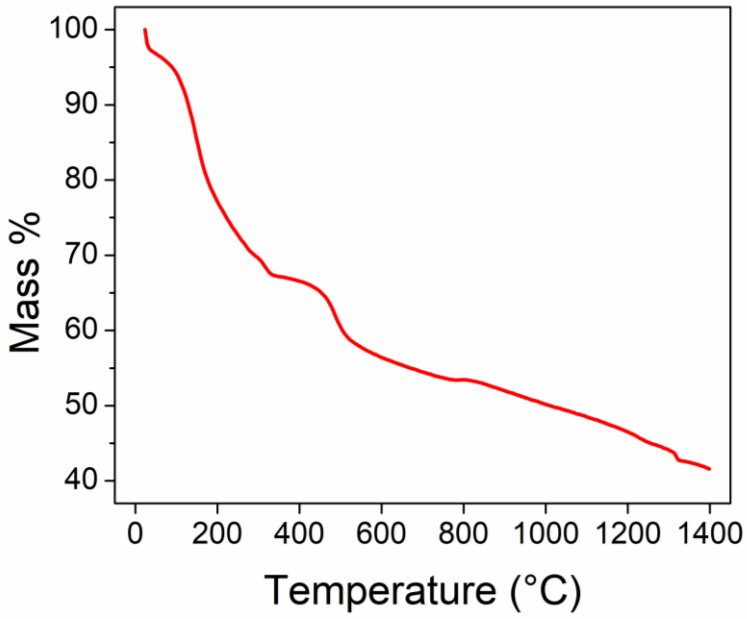

Figure 9: Thermogravimetric analysis of PCN-222 from 25-1400°C.

Powder X-ray diffraction (PXRD) of heat-treated PCN-222 shows a complete loss of reflections of the original PCN-222 structure (Figure 10). Characteristic peaks for ZrC are observed (pattern number 00-001-1050; Panalytical X'Pert Highscore version 2.2a). Peaks corresponding to monoclinic, tetragonal, and cubic zirconia are notably absent. There is a small broader peak around 26° that could be assigned to graphite; however, the heat-treated sample does not exhibit the characteristic graphite peak at 49°, indicating that any residual carbon is of another polymorph.

Before heat treatment at 2000°C, PCN-222 particles have a rod-like shape (Figure 11A). The rods maintain their size and shape after heat treatment, but are marked with bright spots, indicating the separation into two different phases (Figure 11B), in good agreement with the phase diagram for Zr-C.[200] To investigate the nature of these bright spots, images were taken using exclusively the secondary electron detector (SED) and then the backscatter detector (BSD) to confirm that these spots are not topological features. The SED shows contrast according to the height of the sample relative to the detector, and the spots are very faint in Figure 11C. The BSD shows contrast according to atomic weight and shows the bright spots much more distinctly in Figure 11D, meaning that the spots are heavier than the surrounding matrix, and are likely to be ZrC crystals.

Energy dispersive spectroscopy (EDS) mapping of the heat-treated samples indicate that the bright spots contain exclusively carbon, zirconium, and oxygen (Figure 12). Comparison of the maps in Figure 12A-B reveals that the dark regions in the carbon map correspond to bright areas in the zirconium map. Spot analysis of a representative heat-treated PCN-222 particle measured primarily carbon (60%), followed by zirconium (24%) and oxygen (10%). While oxygen is distributed evenly over the sample, this is not consistent with ZrO_2. There is no indication of oxidation in the XRD or TEM diffraction. Fleeting amounts of nitrogen (3.5%) and fluorine (2.7%) arise from contamination when handling the sample. The EDS map in Figure 12D shows Zr is clearly present in the areas of dark crystallites of the TEM image in Figure 12C.

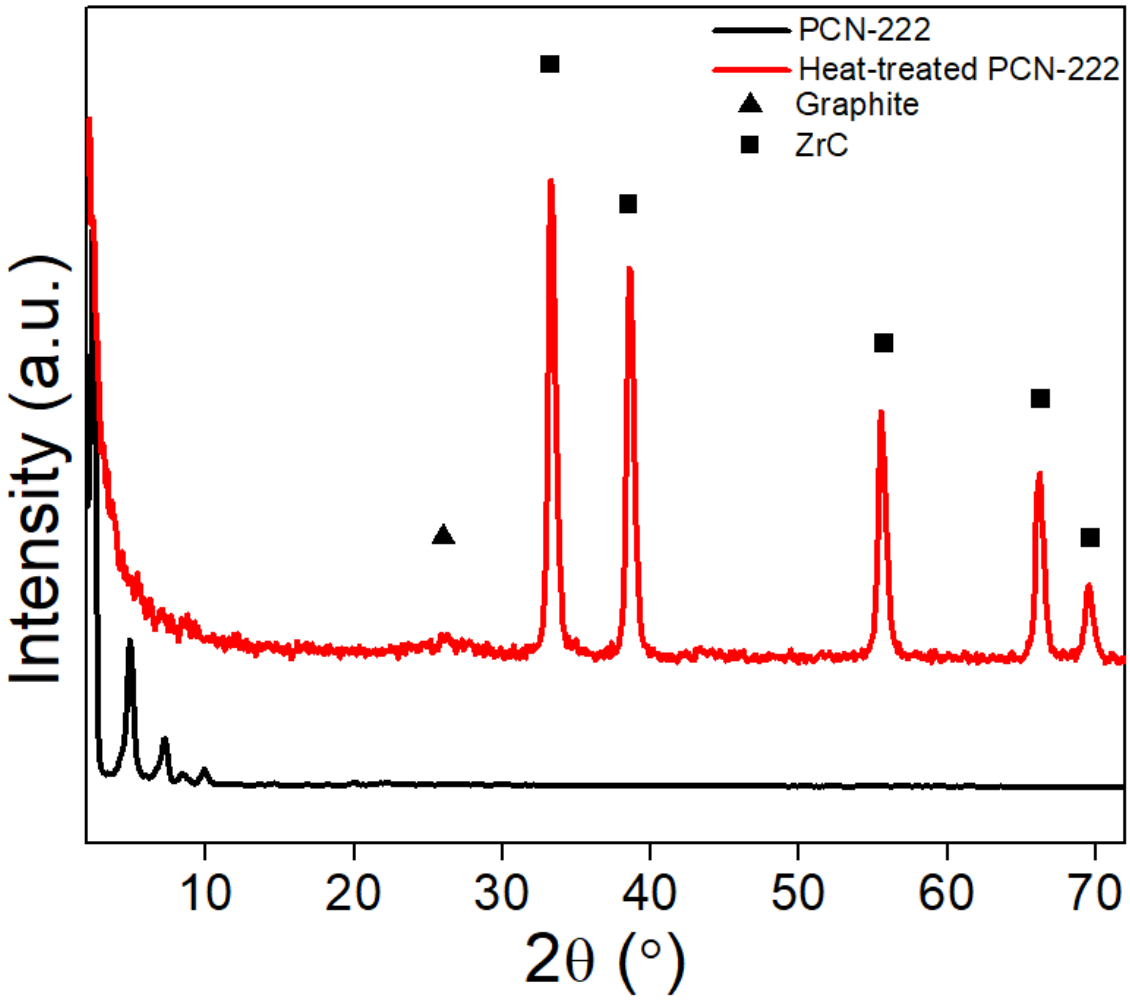

Figure 10: PXRD patterns of PCN-222 as synthesized (black), heat-treated PCN-222 (red), and the reference peaks for graphite and ZrC (pattern number 00-001-1050; Panalytical X'Pert Highscore version 2.2a; JCPDS no. 65-0973[204,205]).

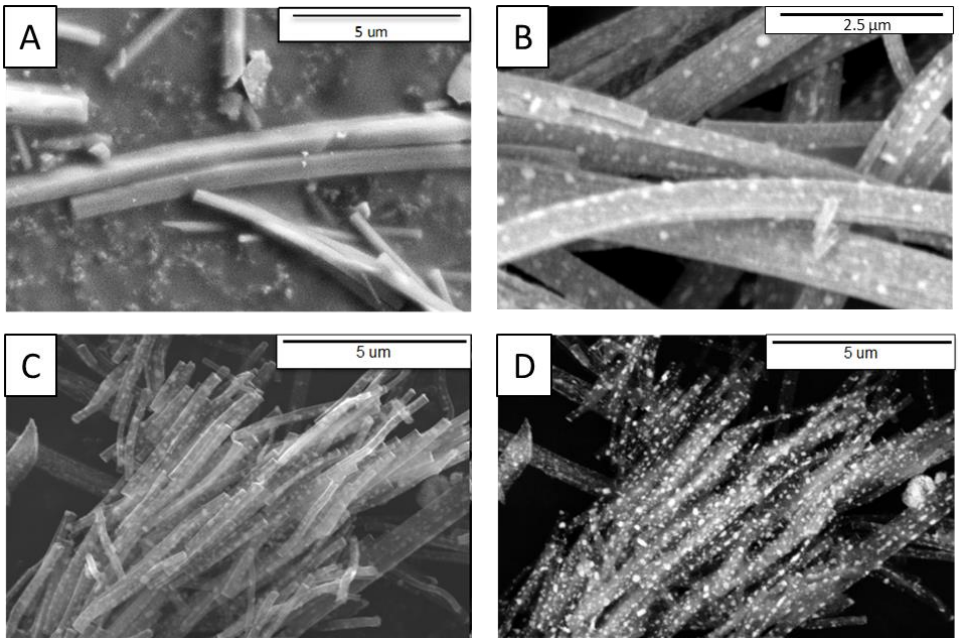

Figure 11: Scanning electron microscope (SEM) images of PCN-222. (A) before heat treatment; (B) after heat treatment, collected with combination SED and BSD; (C) after heat treatment, collected with SED; (C) after heat treatment, collected with BSD.

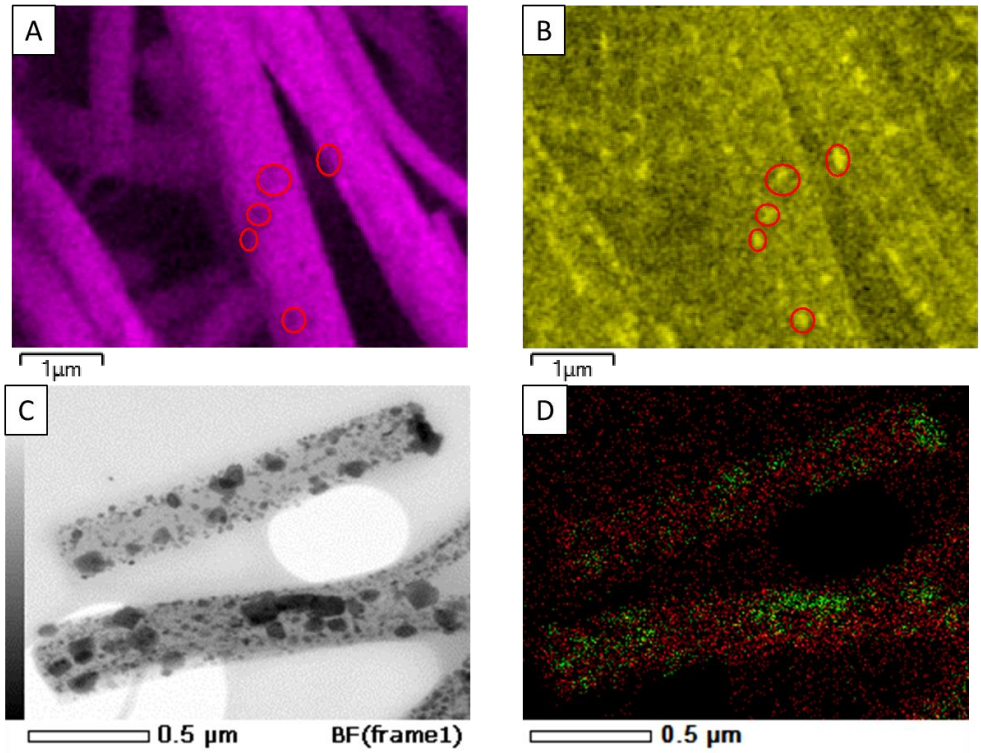

Figure 12: SEM EDS of heat-treated PCN-222. Red circles indicate dark spots on the carbon map (A) corresponding to bright spots on the zirconium map (B). (C) is an additional TEM image, with EDS map (D) showing carbon in red and zirconium in green.

Transmission electron microscope (TEM) images (Figure 13A-C) confirm that PCN-222 powders are smooth rods before heat treatment. The small particles visible in Figure 13A-C are fragments of PCN-222. TEM diffraction did not show any distinct pattern within the dark, blurred space of (Figure 13D). However, PXRD did show a distinct pattern corresponding to this MOF (Figure 10), and other MOFs have exhibited diffraction patterns in TEM.[206] The differences could be associated with sample volumes analyzed or the spot sizes of the techniques.

The omission of the crystalline structure identified in the PXRD pattern is likely because TEM diffraction centers on a much smaller spot size, while PXRD can analyze a wider area. After heat treatment, the hypothesized ZrC crystals visible in SEM and EDS can be seen clearly in the TEM images (Figure 13E-G). The planes of the ZrC crystal are visible in Figure 13E. The ZrC particles are clearly dispersed within the lighter gray matrix. Selected area electron diffraction collected on a crystallite exhibited defined rings consistent with ZrC (Figure 13H). The ZrC (111) plane is present at the highest intensity, along with rings representing the (200), (220),and (311) planes of ZrC.[207] This is consistent with the XRD results and with the phase diagram. However, there were not any specific features that could be attributed to crystalline carbon, i.e., graphite or any other carbon polymorph.

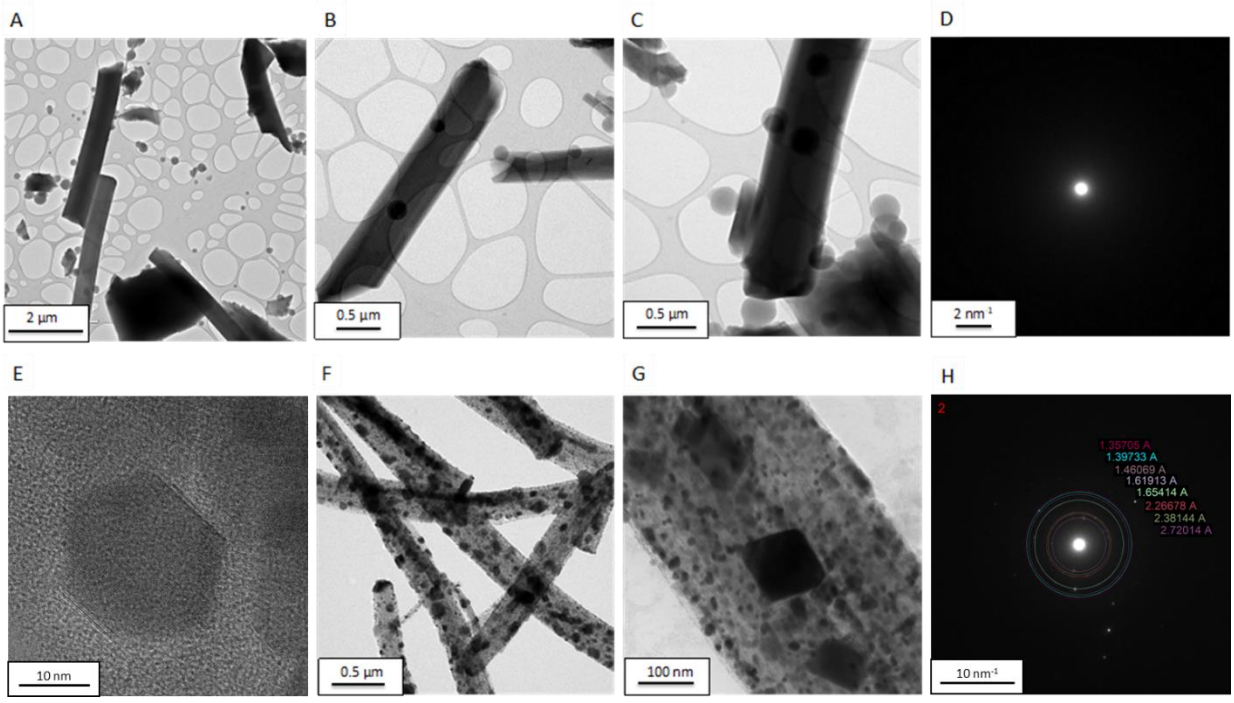

Figure 13: (A)-(C) TEM images of PCN-222, (D) TEM diffraction pattern of PCN-222, (E)-(G) TEM images of heat-treated PCN-222, (H) TEM diffraction c of heat-treated PCN-222.

Raman spectroscopy was used to provide insight into what carbon-based material constitutes the gray-coloured matrix surrounding the ZrC crystals and identify what type of C-bonding is present. The Raman spectrum in Figure 14 shows three peaks consistent with the characteristic sp^2 bonding

of graphite. The D peak is considered the "disorder induced" peak[208] and the 2D peak is associated only with "graphitic clusters" as shown by Koval *et al.* in their study of glassy carbon membranes.[209] The pattern for perfectly ordered graphite would only show one peak (G); pristine graphite requires a higher formation temperature than used in this study.[202,210] These results suggest graphitic character to the bonding present in heat-treated PCN-222's carbon.

The Raman spectrum rules out amorphous carbon, which would not show a 2D peak at all.[209] Neither the PXRD pattern nor the diffraction pattern of Figure 13H indicate graphite's presence. These results may appear to contradict each other. Raman spectroscopy and TEM diffraction measure the molecular bonding and crystal structure, respectively. The C phase in heat-treated PCN-222 contains graphite-like bonding but not a graphitic structure, pointing to the presence of glass-like carbon, in which regions of sp^2 bonded carbon resembling graphite are connected by regions of sp^3 bonds.[211,212] The known properties of glass-like carbon include high strength, thermal conductivity, and thermal shock resistance.[213] The structure continues to be studied and has been described by various models as strained and curved graphite layers, a tangle of graphite ribbons, or a porous shell.[214]

The small mass loss in the TGA at 1300°C (Figure 9) could be attributed to the formation temperature of glass-like carbon and to the required "slow" heating rate.[210–212] The carbon taking part in this reaction likely comes from both the MOF precursor and the graphitic environment of the furnace (graphite crucible, insulation foam, retort, heating elements).[202] In traditional synthesis of glass-like carbon, polymer precursors are heated to at least 600°C[215] until the carbon matrices shrink and encase many pores.[210] This is what we hypothesize is happening with the organic structure surrounding the zirconium cation in the original MOF.

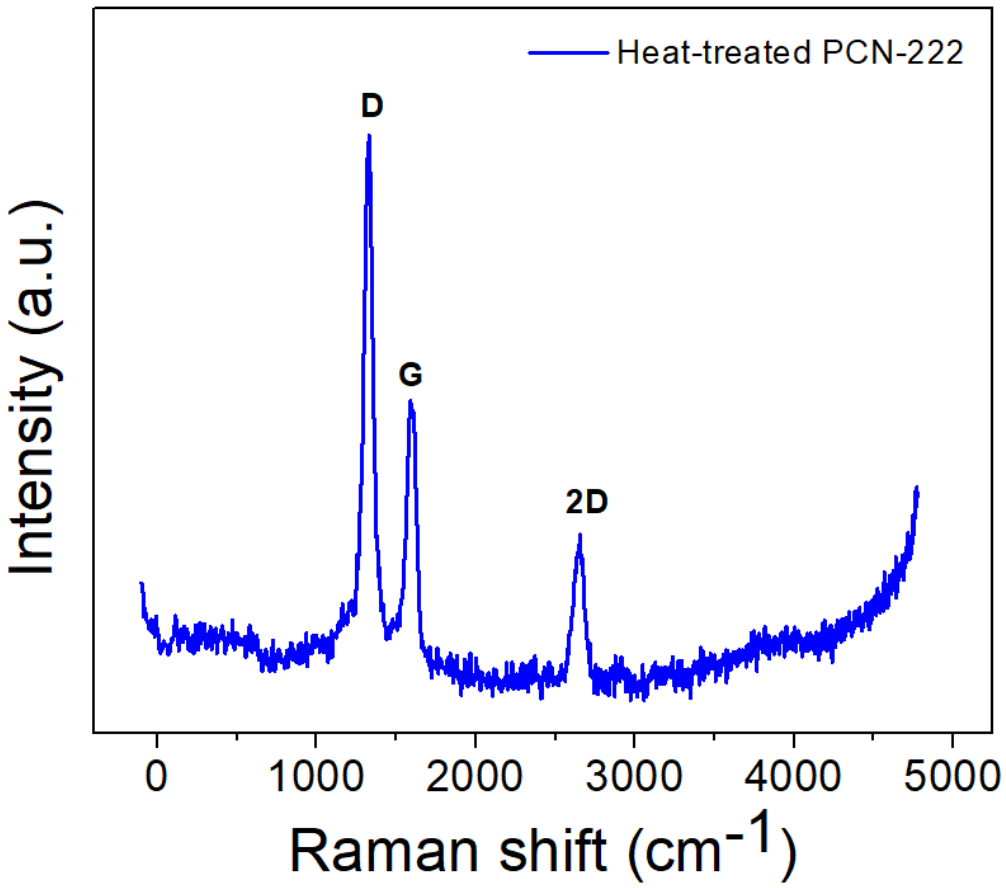

Figure 14: Raman spectrum of heat-treated PCN-222 and locations of graphite's D, G, and 2D Raman peaks.

Glass-like carbon is known to have mostly sp^2 bonds,[216] which explains why we might misidentify the C phase as graphite based on the Raman spectrum (Figure 14). X-ray photoelectron spectroscopy (XPS) shown in Figure 15A-C further describes the type of bonding between the C atoms, indicating predominantly sp^2 carbon bonds for this sample.[217] Further understanding of carbon bonding configurations comes through determination of the D parameter, which is a unique identifier that takes into account the separate contributions of sp^2 and sp^3 bonding in C samples with mixed bond composition, as expected to be the case here.[217] Determination of the D parameter is made by measuring the distance D in eV between the absolute maximum and absolute minimum of the first derivative of the C_KLL Auger peak induced by X-ray (Figure 15C),[217] where KLL refers to an Auger emission arising from the filling of the C 1s hole (K shell) by an electron from the L shell coupled with the ejection of an electron from an L shell.[218] It is known that the D parameter can range from 14.2 eV for diamond (100% sp^3 carbon) to 22.5 eV for graphite (100% sp^2 carbon).The D parameter of any carbon-based material can be placed on a linear approximation between those two extremes (diamond and graphite) based on the percentage of sp^2 bonds (Figure 15D). The D parameter for heat-treated PCN-222 is 20.5eV, placing it at about 92% sp^2 bonds (Figure 15D). The remaining bonds are likely sp^3 bonds that connect the many short-range ordered

regions of sp^2 bonded glass-like carbon. It is because of the small size and random orientation of these regions, the TEM diffraction does not indicate a graphitic signal. The presence of this glass-like carbon explains why the XRD showed a small broad peak of a carbon-based material that was not graphite. The data collected in this study supports the presence of glass-like carbon as the phase surrounding ZrC in heat-treated PCN-222.

There are several reasons that this particle is a candidate for reinforcements of UHTCs in extreme environments. XRD patterns exhibit no signals from unreacted MOF, indicating the high degree of conversion. A particle containing both ZrC and glass-like carbon with this level of purity is sure to maintain the excellent high temperature resistance of the consituent materials. The high aspect ratio is a halmark of reinforcement materials for its ability to deflect and bridge cracks. This along with the high strength, corrosion resistance, and matching coefficients of thermal expansion make these particles attractive as reinforcements for UHTCs, and the described route of synthesis is simpler than those reported in the literature and involves a straightforward transformation.

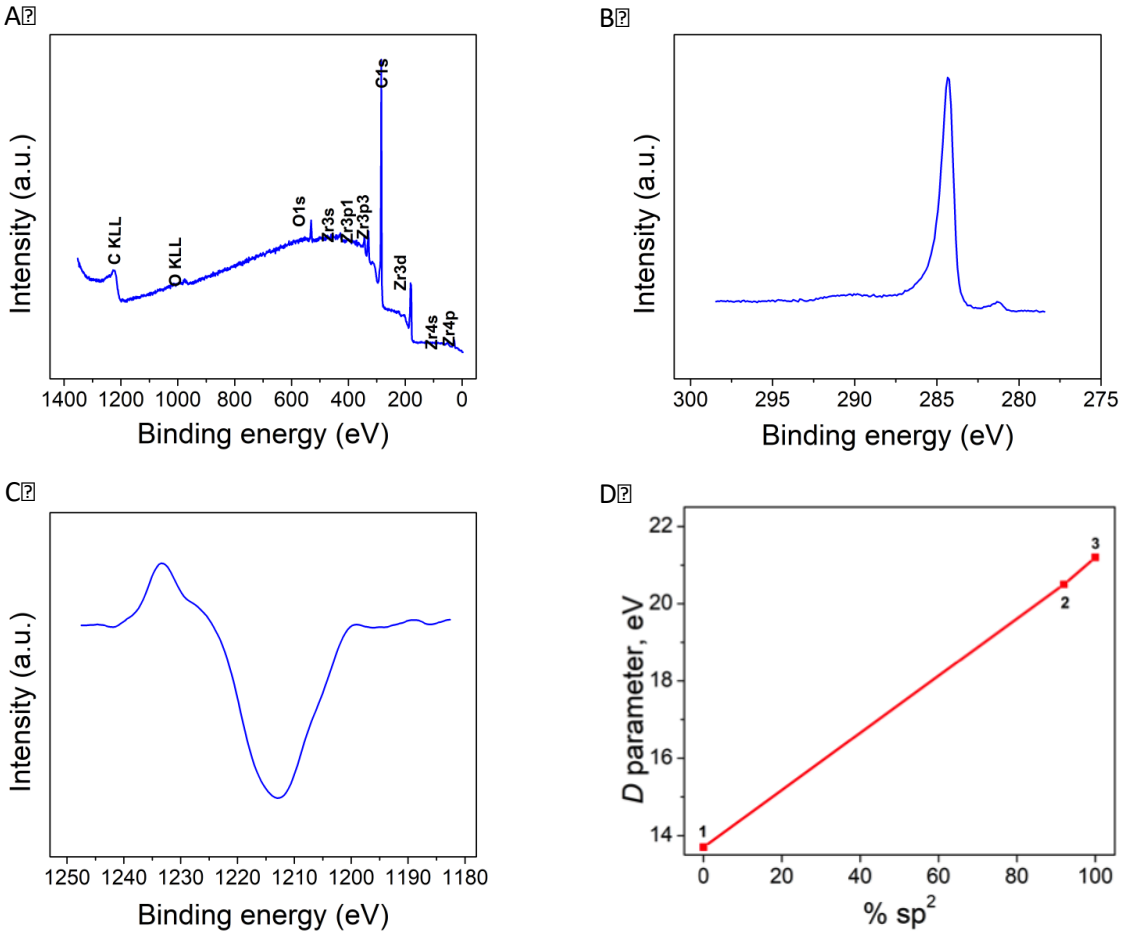

Figure 15: (A) Overall XPS results of heat-treated PCN-222; (B) The C 1s spectrum with primary peak at 284.3 eV and small ZrC peak at 281.3 e, and broad shake-up feature arising from π - π* transition

(290.8 eV),; (C) First derivative of the Auger C KLL spectrum, from which the D parameter is calculated at 20.5 eV; (D) Linear approximation of the D parameter between diamond (1) and graphite (3) based on percentage of sp2 bonds, with PCN-222 (2) placed on the line according to XPS results.

4.4 Conclusion

High temperature thermal treatment of PCN-222 yields ZrC_x crystallites embedded in a carbon matrix. The identity of the carbon matrix was determined to be that of glass-like carbon, featuring small regions of sp^2 bonded carbon connected through sp^3 bonds. Glass-like carbon explains the signals received indicating graphite bonding as well as the absence of graphite structure identification in TEM diffraction. EDS, PXRD, and TEM diffraction confirmed ZrC's presence. XPS has shown that these particles contain 92% sp^2 bonds, while multiple characterization techniques have suggested the presence of graphite. We have shown that following heating to 2000°C, heat-treated PCN-222 contains glass-like carbon as well as ZrC. Given the excellent high temperature characteristics of ZrC and the high aspect ratio of these particles, they have potential as reinforcements for UHTCs that would offer mechanical toughening mechanisms of crack deflection in extreme environment. These particles will be used in the next and final chapter of this dissertation to explore the means of particle alignment during tape casting.

Chapter 5: Understanding grain and particle alignment in sintered, porous TiB_2 tapes

Some of the work in this chapter was presented at the following conferences:

Shirey, Kaitlyn and Tallon, Carolina. "The role of porosity on pressureless-sintered TiB_2 tapes." Ultra-High Temperature Materials for Extreme Environments Conference. Snowbird, Utah. Poster presentation. June 5-8, 2022.

Shirey, Kaitlyn and Tallon, Carolina. "Proof of alignment in tape cast, sintered, porous TiB_2." Nanoscale Characterization and Fabrication Lab Open House. March 15, 2023.

This work is going to be submitted for publication in the Journal of the American Ceramic Society in May 2023.

5.1 Introduction

The incorporation of controlled porosity lowers mechanical strength and thermal and electrical conductivity values. The extent to which a certain amount of porosity should lower each of these is dependent on the material system and the architecture of the grain and pore networks. Many attempting to describe this change in properties rely on minimum solid area model,[219,220] but the minimum solid area is difficult to determine for complex pore networks.[221] The complexity of the pore network cannot be understated. The assumption of spherical pores is insufficient to describe varying shapes, size distributions, connectivity, and anisotropy.[220]

The effect of the pore network created by partial sintering on the mechanical properties of sintered tapes are reported and compared to some of the most used models for predicting Young's Modulus based on porosity. The porosity's role in the presence of particle alignment is also explored. This study seeks to characterize the sintered, porous TiB_2 tapes developed earlier and describe how the architecture of the grains and pores affects the mechanical and thermal properties.

The alignment achieved with the commercially available TiB_2 particles is investigated and deeper understanding is reached by inclusion of the MOF PCN-222, in samples labelled TiB_2+HAR (high aspect ratio particles). This work provides the foundation for future work involving anisotropic additives for purposeful alignment.

5.2 Results and Discussion

The relative density of TiB_2 tapes increases from 50% in green to 62% after sintering at 2000°C for an hour. That corresponds to 38% porosity. Partial sintering was utilized to create the interconnected porous network with significant porosity (>30% for the potential applications

identified in the introduction). This partial sintering ends in the initial stage of densification, where necks have begun to form between grains. The density increases slightly but there remains much interparticle porosity. The shrinkage is isotropic, at about 5-6% in each direction. The homogenous microstructure and near-spherical particle shape (starting particle aspect ratio 1.47) is maintained after sintering (grain aspect ratio 1.50), as shown in SEM images in Figure 16A-B of samples cast at 1.0 cm/s. The homogeneity of the microstructure is representative of samples cast at all speeds. By adjusting the threshold of the image to isolate grains and applying a watershed filter (Figure 16C-E), and using the Analyze Particles function in ImageJ, the feret angles have been collected for samples cast at three different speeds (0.11cm/s, 0.55 cm/s, and 1.0 cm/s).

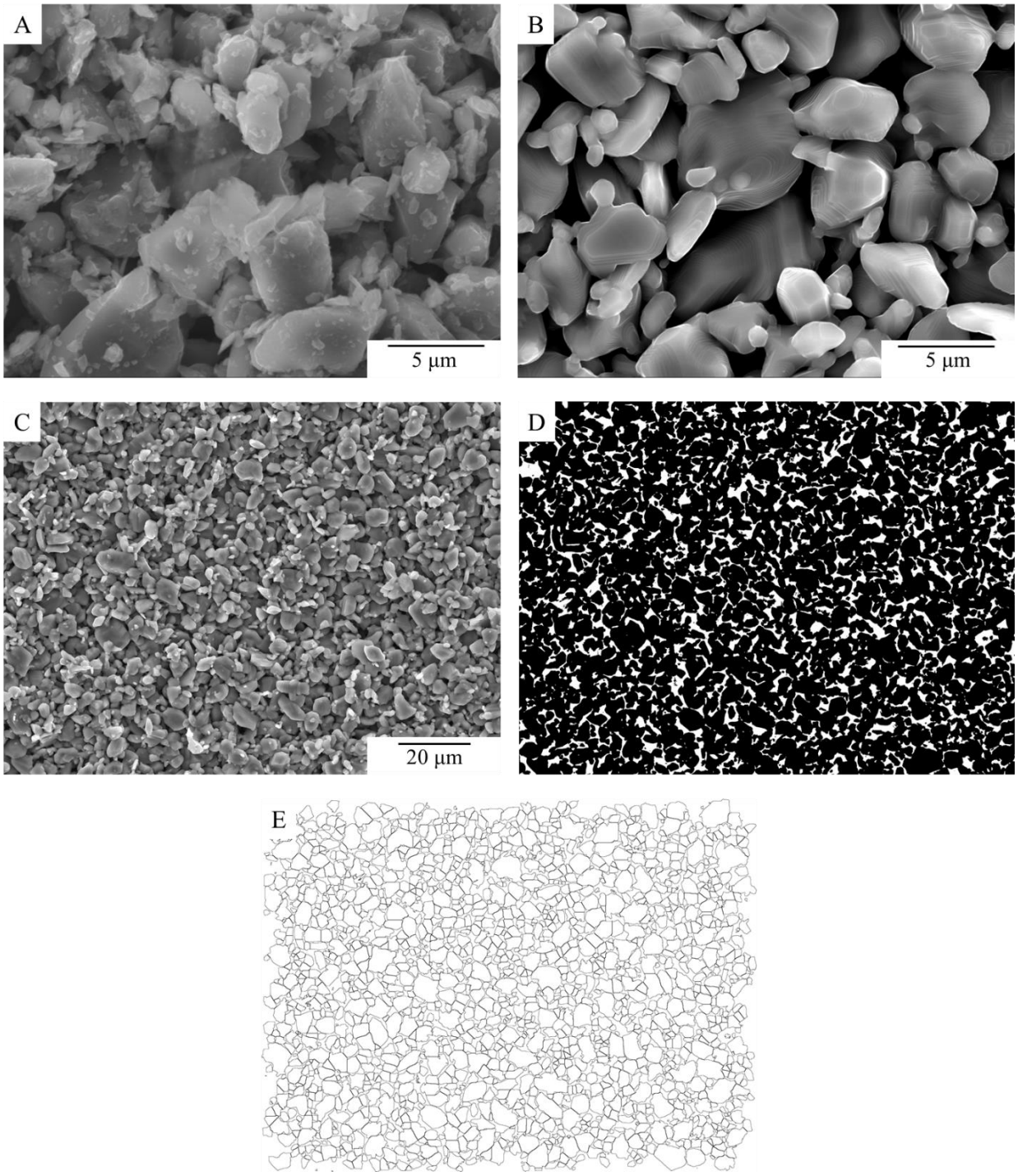

Figure 16: A) SEM image of green TiB_2 tape cast at 1.0 cm/s. B) Sintered TiB_2 tape. Horizontal axis of image corresponds to casting direction. C) Sintered TiB_2 tape at lower magnification. D) The same SEM image in (C) after adjusting the threshold to isolate grains and applying a watershed filter. D) The output image after analyzing particles and drawing bare outlines of those measured.

Figure 17A presents a histogram showing the probability of a grain being aligned at $\cos^2(\Theta)$, where Θ is the feret angle measured in ImageJ with respect to the casting direction. Using the value

$\cos^2(\Theta)$ simplifies the reporting of the angle of orientation; were the results presented in degrees, four grains with the same relative alignment with the casting direction could be reported with four different angles (as an example, 30°, 120°, 210°, and 300° all represent the same angle with respect to casting). By taking the cosine and squaring it, these four values are reduced to one single positive value. Random orientation would give an average value of $\cos^2(\Theta) = 1/3$, alignment perpendicular to the angle of interest 0, and parallel 1.

While there is variation among the population, there is no clear preferential angle of alignment for any condition tested. The distribution is almost a normal distribution for every speed tested. 56.6% of the grains are aligned within 45° of the casting direction. For comparison, random orientation of the grains would be reported as 50% aligned within 45° of the casting direction. Regardless of the speed of casting, there is the barest preference to orient in the casting direction.

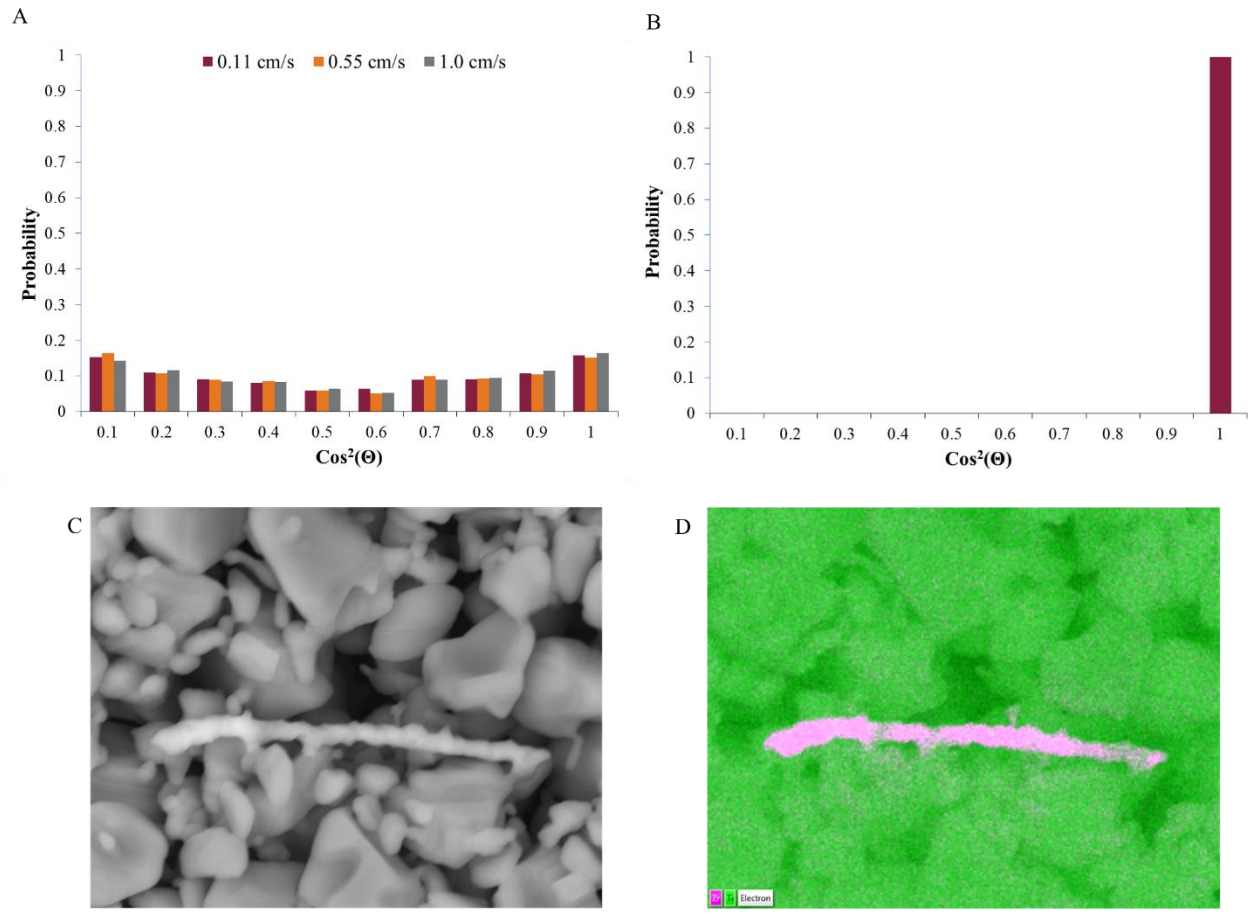

Figure 17: A) Histogram of the probability of alignment at a given value of Cos2(Θ) for each casting speed studied. B) Histogram of the probability of HAR particles alignment. C) SEM image of PCN-222 particle in the sintered TiB_2 tape. D) EDS map of the PCN-222 particle showing that the rod shape contains Zr (pink) whereas the surrounding particles contain Ti (green).

The XRD pattern (Figure 18) shows TiB_2 as expected. The XRD pattern was utilized to estimate crystallographic alignment. By comparing measured intensities of the (0 0 0 1) and (0 0 0 2) peaks to those in the reference pattern for a known, non-oriented TiB_2 sample,[146] it is estimated that the sintered TiB_2 tape has 6% crystallographic alignment. This shows that there is a difference between grain alignment and crystallographic alignment. While the grains of the tape are clearly oriented in the same direction, the crystals contained within the grains are randomly oriented. This XRD analysis was not conducted on the TiB_2+HAR tapes because the low amount of HAR particles after sintering is below the detection limit of XRD.

TiB_2 suspensions were also tape cast and sintered with 2 wt% metal organic framework PCN-222, which has an aspect ratio of about 5-10. EDS maps of these particles were taken to ensure that the rod-shaped particle in question was the sintered PCN-222 (Figure 17D). The EDS map shows a clear Zr signal in the rod shape compared to the Ti based matrix around it, confirming the transformation of PCN-222 into ZrC and glass-like carbon and that the particles are distributed into the matrix, not agglomerated. All of the PCN-222 identified in SEM images after sintering were aligned along the casting direction (Figure 17B).

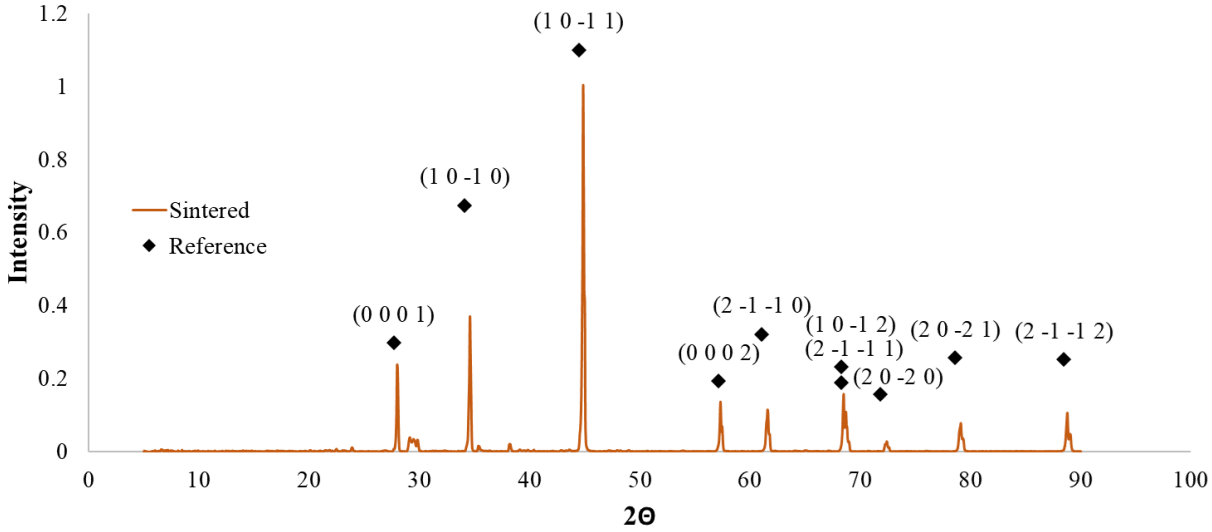

Figure 18: XRD pattern comparing the sintered TiB_2 specimen to a reference pattern.

As mentioned in the introduction, tape casting causes alignment of anisotropic particles in the direction of casting.[9] This is due to the shear force imparted by the doctor blade during casting. Anisotropic particles experience continuous but nonuniform rotation, encouraging the longest axis to point in the direction of casting. While not all particles may be perfectly aligned, the more anisotropic particles experience greater preference toward alignment.[9] This has been studied as the origin of anisotropic shrinkage in tape cast ceramics; alignment along the casting direction causes a greater degree of shrinkage in the lateral direction.[9] The main factor in particle orientation is the

aspect ratio of the particle, with greater aspect ratio particles tending to orient more strongly in the casting direction.[9,124]

Most publications assert that the amount of alignment which occurs during tape casting is independent of the casting parameters, such as speed and blade gap height.[9] Instead, particle shape is the determining factor; As long as the shear force outweighs the hydrostatic pressure pushing suspension out of the reservoir, the parameters of casting like speed and doctor blade shape do not affect the amount of alignment.[9,121,132,133,222] High velocity, low blade gap, large blade thicknesses, and low reservoir filling heights ensure this.[9] Typical casting conditions include velocity between 2-50 mm/s, gap height between 0.25-2 mm, and reservoir height less than 30 mm.[132,133,223] When the hydrostatic pressure-induced flow competes with the shear-induced flow, the casting parameters do affect the ratio between the two forces and therefore the amount of grain alignment. Maintaining negligible hydrostatic pressure-induced flow is also important for maintaining the uniformity of the tape thickness.[224] Dividing the flow into narrower channels with an array of razor blades or pins has been shown to increase the amount of alignment, indicated by 30% greater intensity in the XRD peak of the SiC whiskers.[144] it has also been found that higher viscosity shear-thinning suspensions exhibit higher quality alignment because after the shear rate reaches zero, the particles cease rotation.[132] Further, narrow casting heights (<200 μm) reduce alignment quality because edge effects in the shear rate profile interrupt the rotation of particles.[132]

The extent of alignment can be predicted based on the aspect ratio of the particles in the suspension using Jeffrey's Orbit (Equation 5), a solution to the Navier-Stokes equation.[9,225] The orientation angle Φ is a function of time t, which depends on aspect ratio r and shear rate γ.

$$\phi(t) = \arctan\left(r \cdot tan\frac{\gamma \cdot t}{r+\frac{1}{r}}\right) \qquad \text{[Equation 5]}^{9}$$

The aspect ratio of raw TiB_2 powder used in this study is 1.47 in this study corresponds to a theoretical alignment amount of 63% under the assumptions of laminar flow and negligible particle-particle interactions.[9,225]

To understand more about the mechanisms of alignment, we turn to a phenomenological study of the forces experienced by a particle during tape casting (Figure 19). At position x_0, a particle in the tape casting reservoir experiences a number of forces before the casting process even begins. Electrosteric repulsion acts in all directions in a stable suspension, maintaining dispersion quality. Gravity acts on the particle, but due to sufficient dispersion, Brownian motion dominates, keeping the particle from settling to the bottom of the reservoir. Hydrostatic pressure pushes down on the particle, proportional to the depth of the particle below the suspension surface. These forces are all still at work in the next two steps.

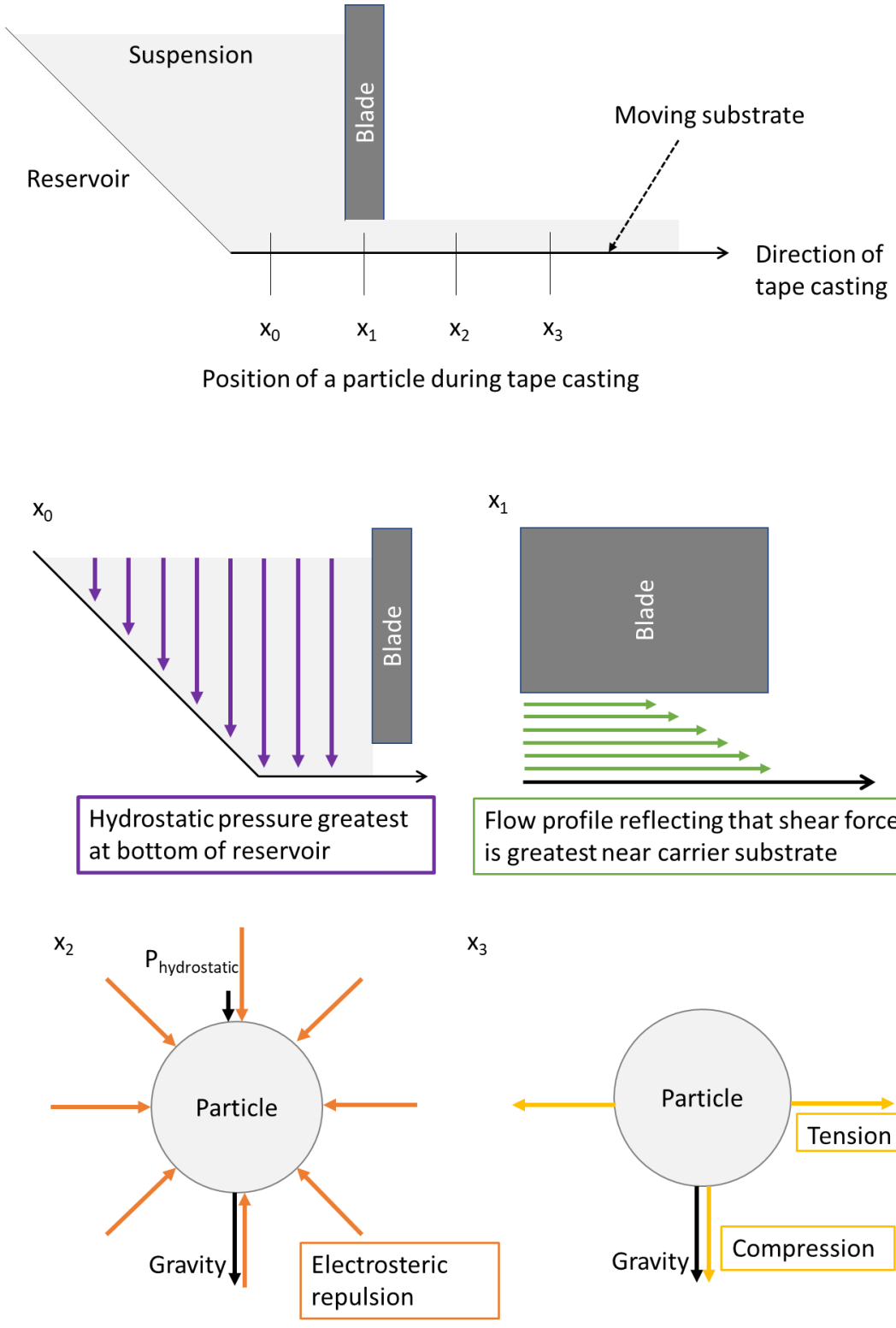

Figure 19: Schematic describing the phenomena experienced by a particle during tape casting based on position within the casting apparatus.

Once the tape casting process begins, the substrate pulls the particle to position x_1, under the doctor blade. The gradient flow profile in this region is greatest near the substrate. Hydrostatic pressure from the suspension in the reservoir is also pushing the particle out from under the doctor blade, but the shear force of tape casting dominates, which is what ensures that anisotropic particles will rotate. In comparison to the literature, the blade gap of 250 μm is relatively low, ensuring that the shear force imparted by the doctor blade on the slurry should dominate over any hydrostatic forces.[9,135] Multiple sources agree that as long as the velocity of casting is sufficiently high (10-250 mm/s[9]; 2.5-60 mm/s[135]; 0.42 mm/s[136]; 5-100 mm/s[129]; 10 mm/s[124]; 2-50 mm/s[132]) and the blade gap sufficiently low (<450 μm[9]), the casting parameters do not impact the orientation of particles; that is, as long as the shear rate is sufficiently high.[9,129,135,136] These sources report shear rates as low as 1.38 s^{-1},[136] and in this study, the shear rates range from 0.4-4 s^{-1}. The alignment of the particles in the slurry is independent of the viscosity of the slurry because the changes in shear rate driving the particle motion and the resistance to that motion associated with different viscosities cancel each other out.[9] It has been suggested that increased solids loading increases the amount of alignment[121,128] and that water-soluble binders added proportionally to increasing solids loading tend to segregate normal to the z-direction, which can mitigate the strength of alignment.[121] However, increased solids loading will naturally reduce the amount of shrinkage, so without orientation measurements, it is difficult to conclude only from less anisotropic shrinkage that more alignment has occurred.

At x_3, with the particle on the other side of the doctor blade, motion continues as the substrate pulls the remaining suspension out of the reservoir, but the particle under study is no longer exposed to the shear force of the doctor blade. The angular momentum allows the particle to continue rotating continuously with non-uniform velocity. The greatest rotational velocity occurs when the longest axis of the particles is perpendicular to the direction of tape casting and the inverse is true, giving a probability of alignment in the casting direction proportional to the anisotropy of the particle. Just as the amount of alignment is independent of the casting speed, the rotational speed of a particle is independent of the suspension viscosity, because the shear force driving rotation and the associated resistance offset each other.[9,129]

Finally, as the tape begins to dry on the casting bed, evaporation causes tensile forces in plane and compressive forces through the plane of the tape. Alignment in the casting direction causes the tape to shrink less in this direction than in the y-direction.[9,137]

In cases of normal operating parameters (sufficiently high casting speed and low blade gap discussed above), there should be grain alignment: sufficiently high velocity, low blade gap, thick blade, and low reservoir filling height ensure that the shear rate will rotate anisotropic particles in suspension.[9] The parameters explored in this study remain well within acceptable ranges. While theoretically, any particle with aspect ratio > 1 should experience nonuniform rotation resulting in measurable alignment, if the aspect ratio is not large enough, the effects will not be pronounced.

Although the results of this study show 56.6% of the TiB_2 grains are aligned instead of the predicted 63%, this is still considered good agreement with the prediction,[9] especially considering that SEM images are only 2-dimensional surface representations of the specimens which may not perfectly reflect the entire structure. 100% of the HAR particles are aligned with the casting direction, which is even higher than the predicted amounts: 87% of grains with aspect ratio of 5, 94% of grains with aspect ratio of 10.

Although there is weak alignment of the TiB_2 grains, there is no discernable alignment of the pore network. The interparticle porosity is homogenously distributed, as expected for partial sintering. Tortuosity depends on the size, orientation, and distribution of pores. Previously, measurement of this dimensionless quantity required painstaking and time-consuming 3D visualization through X-ray tomographic microscopy or focused ion beam scanning electron microscopy (FIB/SEM), but recently a software tool has been introduced to estimate tortuosity using only SEM images.[148]

For the sintered TiB_2 tape with 64%, the Bruggeman exponent in the x and y directions is 0.53 and in the z direction is 0.54. The tortuosity in all directions then is 1.27. With more anisotropic particles, the anisotropy of the tortuosity would be more pronounced. For near-spherical particles such as here, even after sintering, there will not be very much difference in tortuosity in the z direction. For application in a lithium air battery electrode, for example, nominal tortuosity values have been reported in the range of 1.5-2.4.[77]

The hardness and fracture toughness values of the sintered tapes were also measured (Figure 20). Mechanical testing was performed on sintered samples cut parallel and perpendicular to the casting direction. TiB_2tapes had higher hardness values than TiB_2+HAR (0.73 GPa vs 0.30 GPa). For comparison, fully dense TiB_2 has been reported to have values between 15-45 GPa.[20,24,25] There was no difference in fracture toughness measured in different directions for TiB_2tapes (0.17 GPa$\sqrt{m}$); the reported value for fully dense TiB_2 is 6-8 MPa.[20,25] With the inclusion of HAR, the fracture toughness was reduced to below 0.10 GPa $\sqrt{m}$. Furthermore, TiB_2+HAR tapes exhibit directional differences in fracture toughness. The parallel direction is 0.016 GPa $\sqrt{m}$ lower than the perpendicular direction.

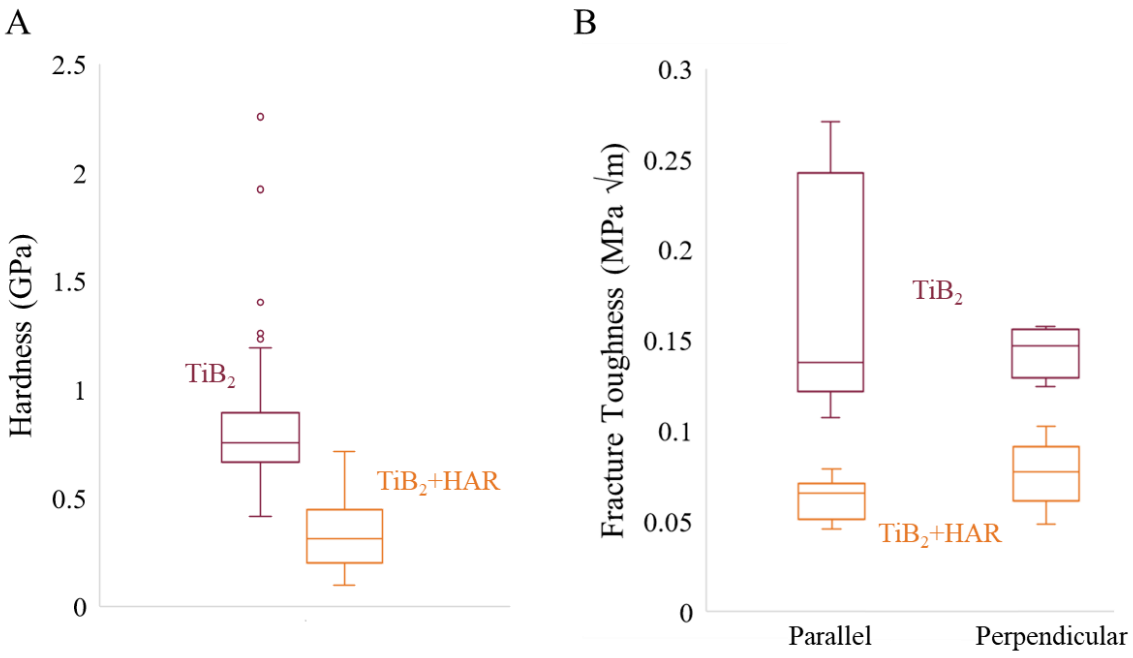

Figure 20: Box and whisker plots comparing Hardness (A) and fracture toughness (B) for TiB_2 and TiB_2+HAR tapes.

The average stress/strain curves obtained for sintered tapes cast at each speed are shown in Figure 21A, and for each cut, TiB_2 and TiB_2+HAR in Figure 21B. The stress/strain curves are typical for brittle ceramic materials. There is some variation between the Young's Moduli of samples cast at different speeds, but there is not a statistically significant difference (Table 5). The average Young's Modulus for these 62% dense tape cast TiB_2 is 95.2 GPa. Sintered TiB_2 tapes do not show a significant difference in Young's Modulus based on the cutting direction, either (Figure 21B).

Table 5: Mechanical property values.

Sample	Fracture toughness (MPa √m)	Hardness (GPa)	Average Young's Modulus (GPa)
1.0 cm/s	0.19	0.57	87.0
0.55 cm/s	0.12	0.80	102.5
0.11 cm/s	0.17	0.74	83.6
TiB_2, parallel	0.17	0.61	93.1
TiB_2, perpendicular	0.14	0.80	88.8
TiB_2+HAR, parallel	0.06	0.36	68.5
TiB_2+HAR, perpendicular	0.08	0.22	68.4

TiB_2+HAR tapes have a lower Young's Modulus than those without (68.9 GPa) and exhibit a difference in the amount of strain to failure. Those cut perpendicular to the cast direction have a lower strain to failure (.009%) than those cut parallel (.011%).

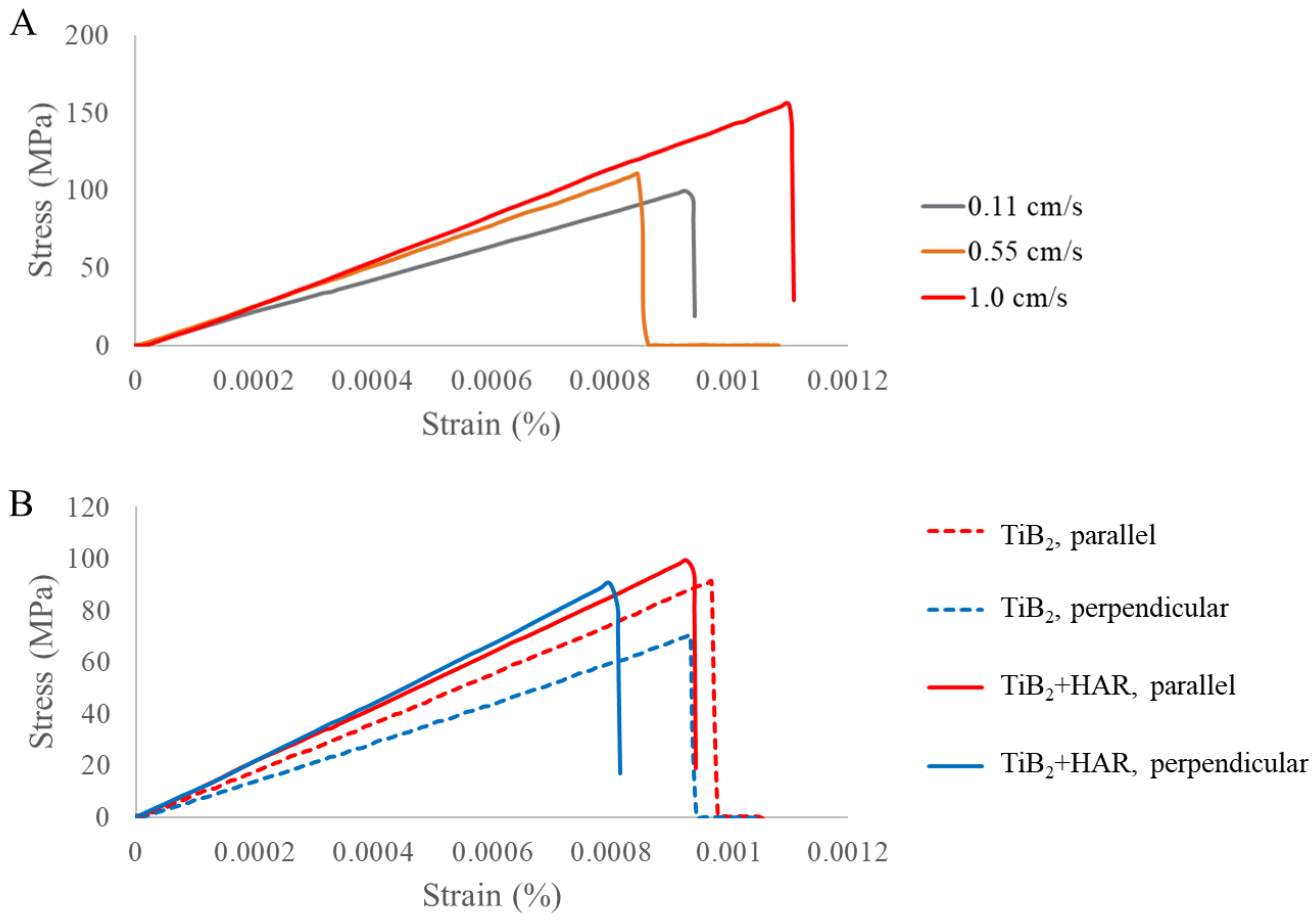

Figure 21: A) Stress/strain curves for samples cast at 0.11, 0.55, and 1.0 cm/s and cut parallel to the casting direction. B) Stress/strain curves for samples cast with and without MOFs, cut parallel and perpendicular to cast direction.

The presence of porosity in ceramic bodies lowers the Young's modulus, hardness, and fracture toughness in comparison to dense counterparts.[4,226] While there are some reports of how much the porosity affects these values for some materials, the relationship depends strongly of the actual porous microstructure. Most of the models cannot capture the complexity of the different porous microstructures, especially for high porosity materials (<80% theoretical density). The assumption of spherical pore shapes in absence of more detailed information is common but fails to provide a realistic model of most pore networks.[220] For example. minimum solid area models have been used to describe property dependence on simple pore networks in bodies of at least 80% theoretical density,[219] but even this association of porosity with a simple exponential relation to properties does not capture the actual porous microstructures.[221]It is also worth mentioning that there is not much literature for porous titanium diboride specifically.

The nominal Young's modulus for dense TiB_2 is 510-575 GPa.[25] The measured Young's modulus is significantly lower than the Young's modulus expected for dense TiB_2 (Figure 22). By the rule

of mixtures, for a TiB_2 sample with 62% density, the Young's modulus would be expected to reach 350 GPa, whereas the samples in this study had an average Young's Modulus of 95.2 GPa. Clearly, the rule of mixtures does not always capture the behavior of a porous body because it does not consider the complex topology and geometry of the pore network,[227,228] or the load paths and different damage mechanisms.[229] There has been work published on determining the relationship between porosity and Young's modulus in ceramic materials, but again, data on the topological properties of the pore networks of ceramics are difficult to find.[220,228]

Arato et al. use the coordination number of grains, the interparticle neck radius, and the sintered density to predict the Young's Modulus.[230] Boonyongmaneerat applies Arato's work to hardness and fracture toughness as well, supporting experimentally that interparticle neck size was the most critical property affecting these mechanical properties in a partially sintered body because cracks propagate through one neck at a time in a partially sintered body.[226] Applying this approach to the tapes in this work, the predicted Young's Modulus is 284 GPa (almost 3 times higher than measured in this study).

Lam, Lange, and Evans assert that there is a linear relationship between the mechanical properties and the relative green and sintered densities, as in Equation 6.

$$\frac{p-p_0}{1-p_0} \qquad \text{[Equation 6]}^{231}$$

where p is the current relative density (after partial sintering) and p_0 is the green density before sintering.[231] Using this equation to scale the predicted Young's Modulus from the fully dense value, the theoretical value for the sintered TiB_2 tapes would be 160 GPa (over 1.6 times higher than measured in this study).

Most previous published work has required the use of fitting parameters, but Boccaccini and Fan[228] present an equation for the effective Young's modulus of a porous ceramic based on a similar calculation for two-phase materials, with utmost importance on accurate measurement of the ratio of the pore to particulate (or grain) size:[227,228]

$$E_p = E_M \frac{(1-P)^2 R}{P+(1-P)R} \qquad \text{[Equation 7]}^{228}$$

where E_P is the effective Young's modulus of the porous material, E_M is the Young's modulus of the pore-free matrix, P is the amount of porosity, and R is the ratio of the pore size to the grain size. Based on these approximations, the Young's Modulus of the 62% dense TiB_2 tape in this work should be about 15% of that of a dense body, or 84 GPa. This value is much closer to the measured value of our tapes (95.2 ± 37 GPa) than the rule of mixtures and other prediction models would suggest it should be.

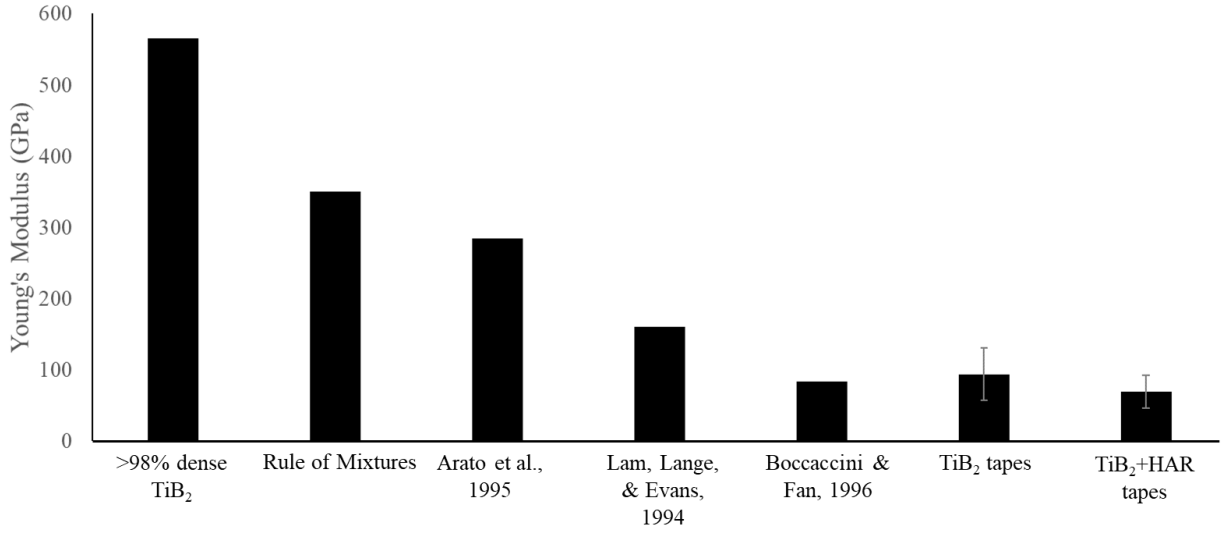

Figure 22: A) Comparison between fully dense, predicted, and measured values of Young's Modulus.

Young's Modulus of the porous, sintered TiB_2 can accurately be predicted using Boccaccini and Fan's equation, which is based on the amount and size of porosity with respect to grain sizes. Therefore, at this high level of porosity and very low level of alignment, porosity is the dominating factor in affecting the Young's Modulus of the material. This is also why there is no directionality to this property, as the porosity is not a directional property. With less porosity or stronger alignment, the Young's modulus dependence may be different. TiB_2 cast with 2wt% of PCN-222 exhibits lower Young's Modulus than without, but still within the range predicted by the Bocccaccini and Fan equation. The density is also slightly lower for the composites (58%), indicating that the inclusion of PCN-222 may deter densification somewhat. This is likely due to the additional organic content evacuating the body during pyrolysis, during transformation of the PCN-222 into the glassy carbon rod with ZrC crystals.

This difference in density is also likely the cause of the lower hardness and fracture toughness of the composites. The fracture toughness exhibits directionality in the composites, with the perpendicularly cut samples having higher values than the parallel samples. This is the opposite of the expectation, as anisotropic particles should increase the fracture toughness in the direction of alignment. Instead, it seems that the alignment of anisotropic particles weakens the component in the parallel direction. It is possible that this is brought on by residual stresses caused by anisotropic shrinkage, but measurements of the components' dimensions before and after sintering reveal a negligible effect of alignment on the shrinkage. The components shrink the same amount in the parallel and perpendicular directions. The inclusion of the HAR may cause slightly more porosity due to its decomposition during sintering. Furthermore, 2 wt% is a very low amount of additives, and the HAR's mass is reduced by about 60% during heating to 2000°C, so the final amount of glass-like carbon rods with ZrC crystallites is less than 1 wt% compared to the TiB_2. With so few anisotropic particles, the effects of the significant porosity dominate.

Research is limited on the mechanical properties of ceramics in the initial stage of sintering.[226] Models for describing the fracture toughness of ceramics with open porosity containing disconnections have been developed and compared to experimental data of cold-pressed and pressureless sintered TiB_2.[232–234] This model depends on the amount of porosity P and the amount of disconnected ligaments n, and is independent of the size and shape of the pores or grains. It seems that the model compares the value of fracture toughness for different porosity amounts to the lowest porosity amount achieved experimentally, rather than the theoretical value of fracture toughness for fully dense TiB_2. This model's boundary conditions cannot be used to accurately represent our data, since the porous network is significantly different and cannot be approximated by the proposed topology in the model.

5.3 Conclusions

TiB_2 has been aqueously tape cast and sintered to 62% density. The alignment of the particles along the tape casting direction was found to be 57%, which is in good agreement with the theoretical value of 63% for an aspect ratio of 1.47. This alignment is independent of the casting speed. The directional differences in tortuosity are small (1.2668 in x and y vs 1.2725 in z directions) because of the relative isotropy of the particles but would be increased with increasing particle anisotropy. Future work in tailoring the tortuosity of ceramic body will rely on the relationship between aspect ratio of the particles and degree of alignment. At these levels of porosity and alignment, the porosity is the dominating factor in affecting the mechanical properties of the TiB_2. The Young's modulus requires a more complex prediction model based on the size of the pores in relation to the grains. The model proposed by Boccaccini and Fan in 1996 provided a reasonably good match to our experimental data.[228] To further investigate alignment of particles under tape casting, TiB_2 suspensions were prepared with 2wt% of the metal organic framework PCN-222, which has a high aspect ratio (5-10). 100% of these particles were aligned along the casting direction. The Boccaccini and Fan model held true for these composites as well. For other mechanical properties such as hardness and fracture toughness, additional research into accurate prediction models are required. As each property describes a different mode of failure, each prediction must be based on different relevant properties of the pore network. Such properties might include the connectivity, openness, etc. in addition to simply the amount of porosity present. The composites exhibited lower fracture toughness and hardness than the monolithic TiB_2, likely due to their lower relative densities. Future work should focus on the amount of alignment and the relative density of the tape cast ceramic to understand more about each's role on the mechanical properties, such as how much alignment would be necessary at each porosity level to observe toughening mechanisms.

Chapter 6: Conclusions and Future work

6.1 Conclusions

TiB_2 is usually used for dense, structural components, but to make the most of this material's great potential, more must be understood about its capabilities for production in other architectures and microstructures and how this affects its properties. This thesis has focused on understanding how the processing-microstructure-properties paradigm can be shifted towards new applications by using tape casting.

The main outcomes of this thesis are the following:

1. An extensive literature review about TiB_2 uses and applications as a function of microstructure has been conducted, identifying potential applications that would benefit from introduction of different microstructural features such as porosity, and different architectures, such as tapes. Some of the potential applications include lithium air batteries, aluminum smelting cells, and active cooling for thermal protection systems.

2. For the first time, TiB_2 has been tape cast. This was accomplished by careful tailoring of the suspension formulation for stability and shear thinning behavior, using lower additive content than is state of the art for tape casting. The process of this formulation optimization can be adapted to other material systems, such as accomplishing tape cast TiB_2 in organic solvent.

   Another advantage of the suspension formulation is reusability. Due in part to the success of the two-step mixing method described in Chapter 2, the green bodies may be ball milled into powder form and need only the addition of water to become a castable suspension once more. Once cast these specimens retain flexibility, uniformity, and the ability to peel. TiB_2 suspensions have been reused twice in this manner without affecting any of these properties.

3. The MOF PCN-222 was utilized to generate high aspect ratio high temperature particles to understand the alignment under tape casting and explore its potential role as reinforcing agent for high temperature applications. The initial MOF was treated at 2000°C to create the high aspect ratio particles, and extensive characterization confirmed that the resulting composition is a glass-like carbon matrix embedded with zirconium carbide crystallites, which is ideal to be used in high temperature applications. The high aspect ratio of this anisotropic, rod-shaped particle is maintained after heat treatment. This is the first time that such structures have been used to generate UHTC particles. Future work may include

efforts to synthesize a metal organic framework with a titanium ion that may form TiB_2 after heat treatment.

4. The final chapter of this work establishes that porous TiB_2 tapes can be created. The porous, sintered tape cast TiB_2 exhibits near the theoretical value of grain alignment caused by tape casting and a large amount (38%) of connected interparticle porosity retained by partial sintering. Values for the elastic modulus are established for these ~60% dense specimens and compared to predictions from the literature. It is found that Boccaccini and Fan's model, taking into account the size ratio of grains and pores, is the most accurate description of the way that porosity in this case affects the elastic modulus. Furthermore, suspensions containing the MOF-derived high aspect ratio particles (TiB_2+HAR) were investigated for the amount of alignment present and the effects of this inclusion on the hardness and fracture toughness of the specimens. While 100% of these HAR particles are shown to be aligned through image manipulation, this low concentration does not affect the mechanical properties. The porosity's effects dominate the mechanical behavior of the sintered tapes.

   It is worth noting that the suspension formulation developed in Chapter 2 is so robust that the addition of 2 wt% of the MOF PCN-222 does not affect the stability of the suspension. This suspension can be tape cast and preserves the flexibility and uniformity of the formulation, as described in Chapter 3. These specimens can be peeled from the substrate and exhibit similarly homogenous microstructures to those without the addition of PCN-222.

In summary, this work has explored the production of new architectures in TiB_2 through tape casting and provided promising groundwork for future study. The suspension formulation developed here is a novel contribution to the field and the process of that development can be applied to other material systems. Tape cast TiB_2 has been described for the first time, and the porosity and alignment within the samples characterized. The inclusion of a high aspect ratio, glass-like carbon and ZrC-based particle was utilized to further understand the process of alignment during tape casting, and there is a clear path forward for future work seeking to quantify the amount of such a high aspect ratio particle needed to create anisotropy in the material properties. Other avenues of future work can push the complexity of the architectures developed here even further, toward curved tapes or layered structures. By taking full advantage of these shaping and microstructural opportunities, state of the art applications for TiB_2 can push past the intersection of dense and structural materials toward porous and functional components that could revolutionize thermal protection systems for hypersonic flight or Li-air batteries. In other words, the culmination of this work is grounded in a scientific contribution to the field of materials, with eyes toward branching into the exciting applications of tomorrow.

6.2 Future Work

Future work for this project could focus on a variety of other directions. These are some of the directions and the preliminary results obtained during this dissertation:

1. **Higher number of anisotropic particles.**
    a. **Preparing a suspension with a greater amount of PCN-222** to see how much is needed to improve the fracture toughness of the samples or to cause anisotropic shrinkage during sintering. Availability of this particle was prohibitive during the completion of this dissertation, but it would be worthwhile to cast a suspension containing 5-10 wt%. Similarly, if higher aspect ratio TiB_2 was available, it would be interesting to find the smallest aspect ratio of TiB_2 particle needed to exhibit anisotropic mechanical behavior in the sintered component and further investigating the balance between the porosity and alignment of particles and their effects on material properties. It would also be interesting to see if TiB_2 could be synthesized from MOFs as in Chapter 2.

    Carbon nanotubes (CNT) were investigated as another option for a high aspect ratio additive, but the hydrophobicity of these particles proved too strong for the aqueous suspension formulation developed here. Again, using the first chapter of this dissertation as a framework, a suspension could be formulated such that a stable TiB_2+CNT suspension could be tape cast. There is potential for crack bridging and deflection behavior if a more significant amount of high aspect ratio particle could be included in the suspension, and the determination of the minimum concentration required would also be an interesting study.

    b. **Comparing electrical resistivity and thermal conductivity** of the porous body to fully dense and isotropic samples would be helpful in further understanding how porosity affects the material in extreme environments and how anisotropy of these properties may be achieved with the inclusion of enough anisotropic particles. In this study, we have measured electrical resistivity of the porous TiB_2 tapes and found that the value follows the rule of mixtures, giving an electrical resistivity of about 50 μ ohm cm (Figure 23). At the time of the defense of this dissertation, thermal conductivity values have not yet been obtained, but the HAR particle has highly conductive components (glass-like carbon and ZrC) which may allow for directional control of the thermal conductivity even within the highly porous body.

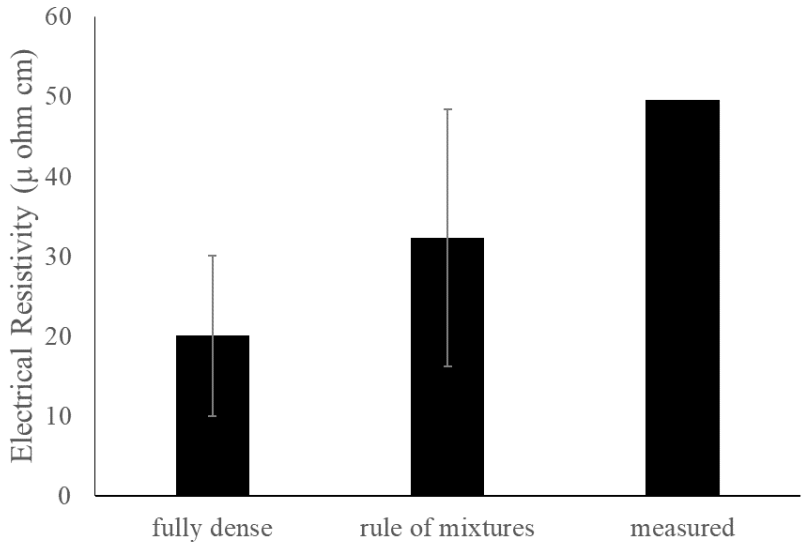

Figure 23: Comparison of the electrical resistivity of fully dense TiB_2 with the rule of mixtures and the measured value for 62% dense samples.

2. **Tapes as building blocks for more complex microstructures**.
    a. **High curvature architectures**. Figure 24A-C shows TiB_2 samples which were rolled in green and subsequently sintered into the curled shape. These samples can be created in a variety of sizes and with varying numbers of full rolls. Samples were also rolled inside the molds for ice templating and then filled with suspension. The tape cast specimens were unaffected by the freezing and sublimation steps of ice templating (Figure 24D-F).

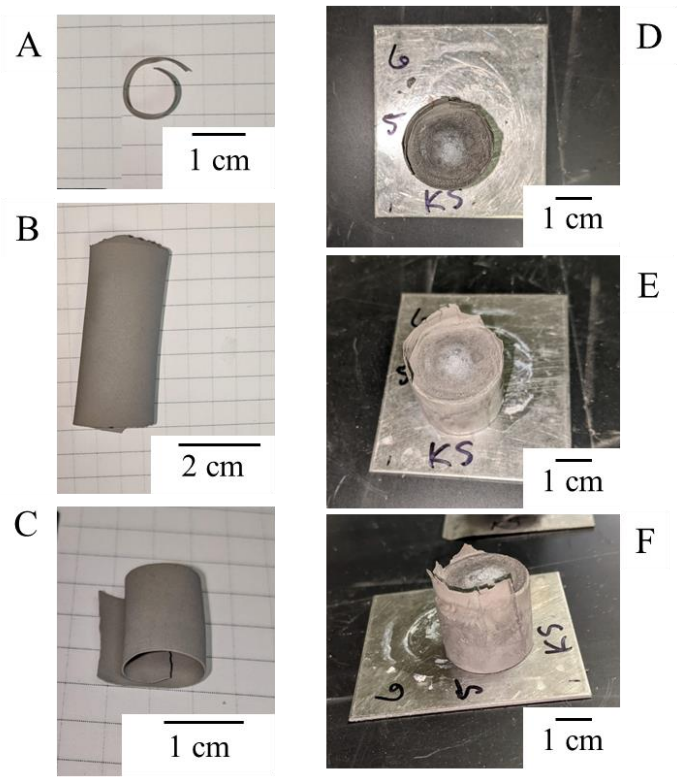

Figure 24: Photographs of tape cast TiB_2 after curling and sintering (A-C), and curled around ice templated cylinders in green (D-F).

b. **Building blocks for ice templating**. Including a green tape cast specimen of TiB_2 in a sandwich between ice templated layers can redirect the ice growth during freezing (Figure 25). The SEM image in Figure 25C-D shows how dendritic pores formed by ice run parallel to the tape after growing upward from the metal mold. Figure 25D provides a closer view of the interface between the tape cast and freeze cast TiB_2. Such a redirection of the aligned pore network is not well documented in the literature.

   The TiB_2 tapes themselves may be ice templated to design a dendritic pore network. Figure 26 shows SEM images of a green body after freezing and freeze drying, showing the macropore structure from the top and bottom of the sample, which themselves show a great difference in pore scale even though the entire thickness is less than 250 μm. Including both interparticle and dendritic porosity in a sample achieves the dual-scale pore network suggested for many Li-air cathode structures and allows for greater complexity in the design of the tortuosity in different directions.

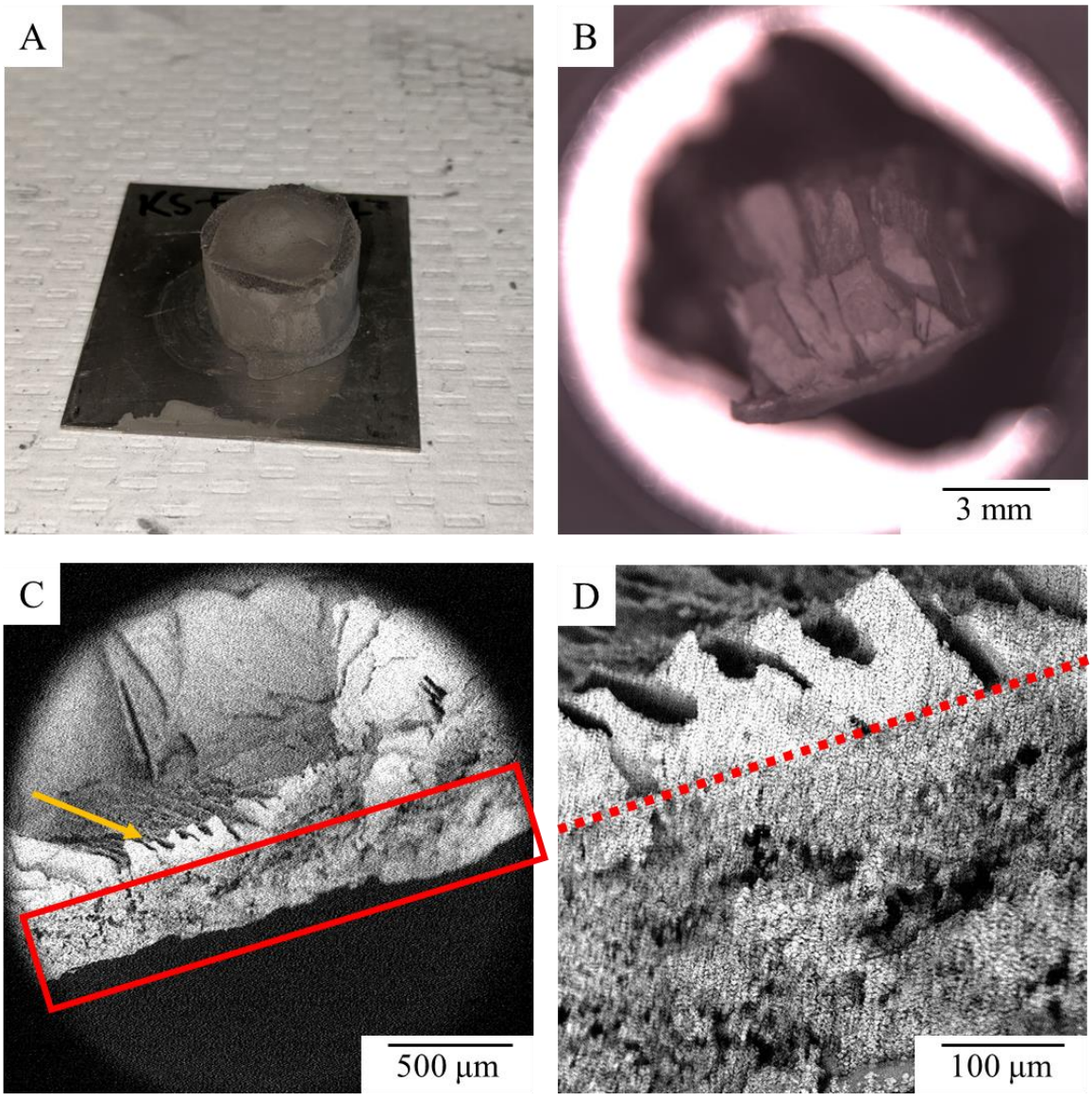

Figure 25: (A) Photograph of ice templated sample created with tape specimen on top. (B) Optical microscope image of fracture surface of specimen, with tape sample on bottom. (C) SEM image of sample. Yellow arrow indicates direction change in the dendritic pore network when the ice front reaches the tape, outlined in red. (D) SEM image of the interface between tape cast and ice templated TiB_2, dotted line indicating the border.

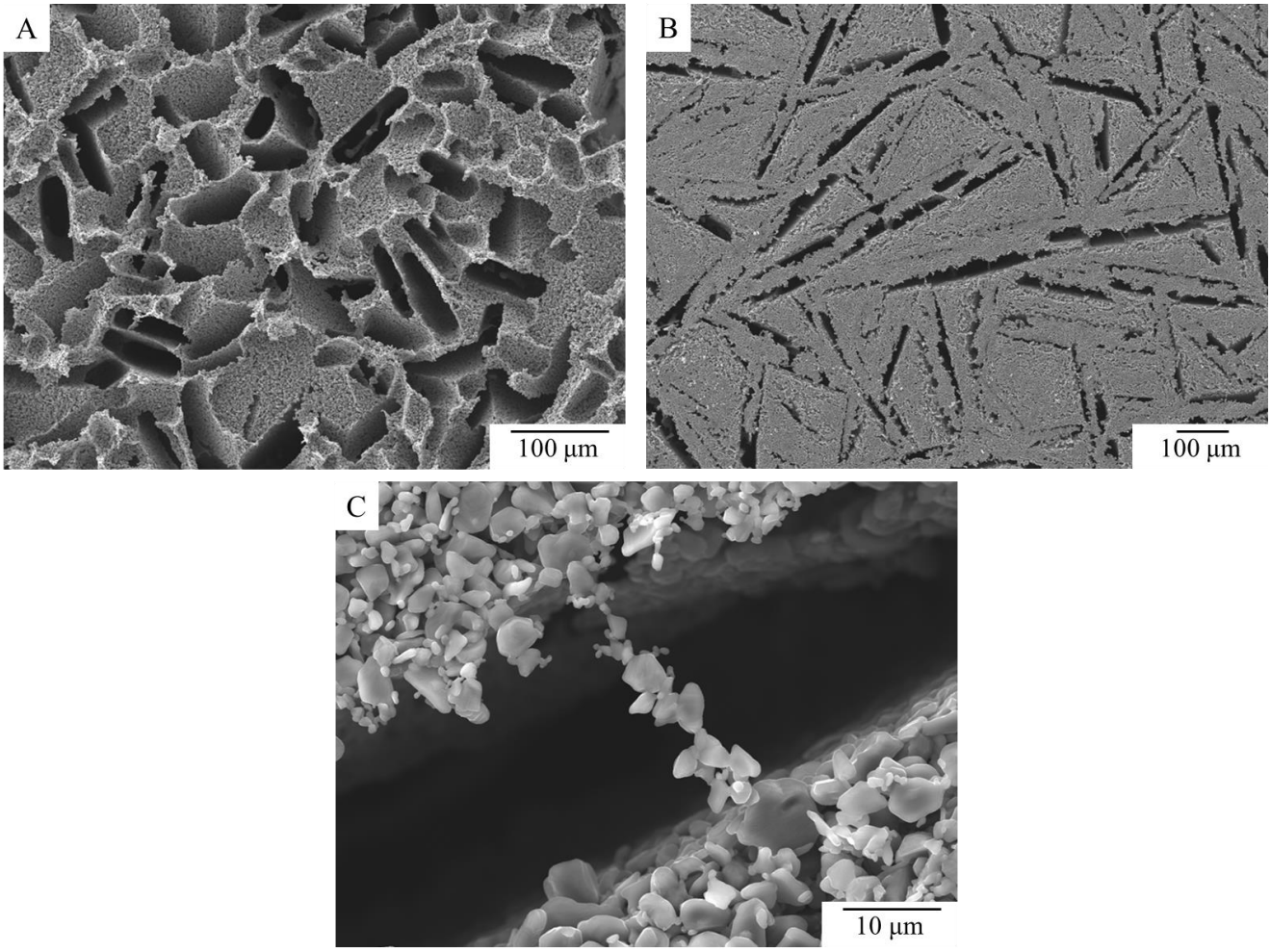

Figure 26: SEM images of (A) the bottom of freeze cast TiB_2 tape, (B) the top of the sample, and (C) a bridge of TiB_2 particles within the dendritic pore, probably formed by a chain of binder.

c. **Building blocks for multilayered structures.** Finally, samples may be stacked on top of each other in green to produce layered bodies. Layered ceramic bodies are attractive for improving fracture toughness, for example.[235] This has been accomplished by simply layering green bodies in the crucible before sintering. An example microstructure of these samples is shown in Figure 27. Stacks may also be laminated together with the assistance of pressure and heat, although careful attention must be paid to the balance of these forces to prevent damage to the fragile specimens during lamination.

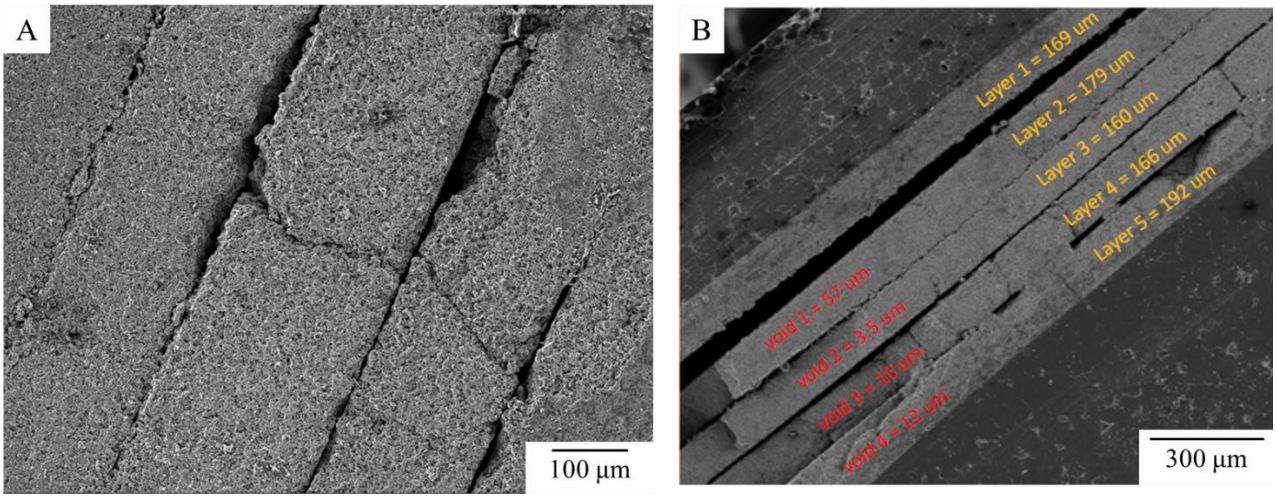

Figure 27: SEM images of TiB_2 tapes sintered into a layered structure (A); (B) layers and voids between them labelled with their thicknesses.

Chapter 7: References

(1) Park, J.; Lee, Y.; Koh, Y.; Kim, H. Effect of Hot-Pressing Temperature on Densification and Mechanical Properties of Titanium Diboride with Silicon Nitride as a Sintering Aid. *Journal of the American Ceramic Society* **2000**, *44*, 1542–1544.

(2) Bakhit, B.; Palisaitis, J.; Thörnberg, J.; Rosen, J.; Persson, P. O. Å.; Hultman, L.; Petrov, I.; Greene, J. E.; Greczynski, G. Improving the High-Temperature Oxidation Resistance of TiB_2 Thin Films by Alloying with Al. *Acta Mater* **2020**, *196*, 677–689. https://doi.org/10.1016/j.actamat.2020.07.025.

(3) Balcı, Ö.; Burkhardt, U.; Schmidt, M.; Hennicke, J.; Barış Yağcı, M.; Somer, M. Densification, Microstructure and Properties of TiB_2 Ceramics Fabricated by Spark Plasma Sintering. *Mater Charact* **2018**, *145* (September), 435–443. https://doi.org/10.1016/j.matchar.2018.09.010.

(4) Nishihora, R. K.; Rachadel, P. L.; Quadri, M. G. N.; Hotza, D. Manufacturing Porous Ceramic Materials by Tape Casting—A Review. *Journal of the European Ceramic Society*. Elsevier Ltd April 1, 2018, pp 988–1001. https://doi.org/10.1016/j.jeurceramsoc.2017.11.047.

(5) Hicks, D. C.; Zhou, Z.; Liu, G.; Tallon, C. Aligned Continuous Cylindrical Pores Derived from Electrospun Polymer Fibers in Titanium Diboride. *Int J Appl Ceram Technol* **2019**, *16* (2), 802–813. https://doi.org/10.1111/ijac.13122.

(6) Demirskyi, D.; Cheng, J.; Agrawal, D.; Ragulya, A. Densification and Grain Growth during Microwave Sintering of Titanium Diboride. *Scr Mater* **2013**, *69* (8), 610–613. https://doi.org/10.1016/j.scriptamat.2013.07.012.

(7) Lim, C. S.; Sofer, Z.; Mazánek, V.; Pumera, M. Layered Titanium Diboride: Towards Exfoliation and Electrochemical Applications. *Nanoscale* **2015**, *7* (29), 12527–12534. https://doi.org/10.1039/c5nr02692j.

(8) Osburn, C. M.; Wang, Q. E.; Ruggles, G. A.; Shah, A. S. Electrical Characteristics of TiB_2 for ULSI Applications. *IEEE Trans Electron Devices* **1992**, *39* (10), 2341–2345. https://doi.org/10.1109/16.158806.

(9) Dellert, A.; Heunisch, A.; Roosen, A. The Origin of Anisotropic Shrinkage in Tape-Cast Green Tapes. *Applied Ceramic Technology* **2011**, *1319*, 8–15. https://doi.org/10.1111/j.1744-7402.2011.02665.x.

(10) Franks, G. V. Colloids and Fine Particles. In *Introduction to Particle Technology: Second Edition*; 2008; pp 117–152. https://doi.org/10.1002/9780470727102.ch5.

(11) Tallon, C.; Franks, G. V. Exploring Inexpensive Processing Routes to Prepare Dense TiB_2 Components. *Advances in Applied Ceramics* **2016**, *115* (7), 403–410. https://doi.org/10.1080/17436753.2016.1172166.

(12) *Ultra-High Temperature Ceramics: Materials for Extreme Environment Applications*; Fahrenholtz, W. G., Wuchina, E. J., Lee, W. E., Zhou, Y., Eds.; Wiley, 2014.

(13) *Carbide, Nitride, and Boride Materials Synthesis and Processing*; Weimer, A., Ed.; Springer, 1997.

(14) Cao, X.; Xue, X.; Li, Z.; Jiang, T.; Zhang, an. Structure and Capability of TIB2/UHMWPE Composite Shielding Material for Nuclear Radiation. In *Materials Characterization, Computation, Modeling, and Energy*; The Minerals, Metals & Materials Society, 2010; pp 123–128.

(15) Dai, W.; Gao, X.; Li, X.; Wang, Q. Influence of Carbon Incorporation on Microstructure and Properties of Titanium Diboride Coatings Deposited by Combining Ion Beam with Magnetron Sputtering. *Ceram Int* **2019**, *45* (17), 22498–22505. https://doi.org/10.1016/j.ceramint.2019.07.273.

(16) Huang, X.; Sun, S.; Tu, G. Investigation of Mechanical Properties and Oxidation Resistance of CVD TiB2 Ceramic Coating on Molybdenum. *Journal of Materials Research and Technology* **2020**, *9* (1), 282–290. https://doi.org/10.1016/j.jmrt.2019.10.056.

(17) Vance, M. W. *Low Cost Sintering of Titanium Diboride for Armor*; 1988.

(18) Wu, N.; Xue, F.; Yang, H.; Li, G.; Luo, F.; Ruan, J. Effects of TiB2 Particle Size on the Microstructure and Mechanical Properties of TiB2-Based Composites. *Ceram Int* **2019**, *45* (1), 1370–1378. https://doi.org/10.1016/j.ceramint.2018.08.270.

(19) Golla, B. R.; Bhandari, T.; Mukhopadhyay, A.; Basu, B. Titanium Diboride. In *Ultra-High Temperature Ceramics: Materials for Extreme Envionment Applications*; Fahrenholtz, W. G., Wuchina, E. J., Lee, W. E., Zhou, Y., Eds.; John Wiley & Sons: Hoboken, New Jersey, 2014; pp 316–360.

(20) Munro, R. G. Material Properties of Titanium Diboride. *J. Res. Natl. Inst. Stand. Technol* **2000**, *105* (5), 709–720.

(21) Liang, H.; Chen, H.; Peng, F.; Liu, L.; Li, X.; Liu, K.; Liu, C.; Li, X. High-Pressure Strength and Compressibility of Titanium Diboride (TiB2) Studied under Non-Hydrostatic Compression. *Journal of Physics and Chemistry of Solids* **2018**, *121*, 256–260. https://doi.org/10.1016/j.jpcs.2018.05.042.

(22) Basu, B.; Kalin, Mitjan. Table 9.3. Summary of Important Physical and Mechanical Properties of Titanium Diboride, TiB_2 and the Other Important Ceramics. In *Tribology of Ceramics and Composites - A Materials Science Perspective*; John Wiley and sons, 2011; p 135.

(23) Munro, R. G. Material Properties of Titanium Diboride. *J Res Natl Inst Stand Technol* **2000**, *105* (5), 709.

(24) Sundaram, V.; Logan, K. V.; Speyer, R. F. Reaction Path in the Magnesium Thermite Reaction to Synthesize Titanium Diboride. *J Mater Res* **1997**, *12* (10), 2657–2664. https://doi.org/10.1557/JMR.1997.0355.

(25) *ASM Handbook, Volume 20 - Materials Selection and Design - Table 2. Properties of Ceramics - Knovel*. https://app-knovel-com.ezproxy.lib.vt.edu/web/view/itable/show.v/rcid:kpASMHVMS2/cid:kt008XDOF3/viewerType:itble//root_slug:table-2-properties-of-ceramics/url_slug:table-2-properties-ceramics?b-q=material_or_substance_name%3A%20TiB2%20AND%20density_mf%3A% (accessed 2021-12-02).

(26) Malik, I.; Banerjee, S.; Gayner, C.; Chowdhuri, A.; Kar, K. K. Synthesis and Thermoelectric Performance of Titanium Diboride and Its Composites with Lead Selenide and Carbon. *Ceram Int* **2018**, *44* (9), 10685–10692. https://doi.org/10.1016/j.ceramint.2018.03.100.

(27) Ban, Y.; Wang, Z.; Shi, Z.; Kim, H.; Yang, S.; Cao, X.; Qiu, Z. Preparation of TiB_2 Inert Cathode on Graphite by Electrodeposition Process for Aluminum Electrolysis. *Light Metals* **2007**, No. 1996, 1055–1059. https://doi.org/10.1073/pnas.0709640104.

(28) Matkovich, I.; Board, E. *Boron and Refractory Borides*; 1977. https://doi.org/10.1007/978-3-642-66620-9.

(29) Baumgartner, H. R.; Steiger, R. A. Sintering and Properties of Titanium Diboride Made from Powder Synthesized in a Plasma-Arc Heater. *Journal of the American Ceramic Society* **1984**, *67* (3), 207–212. https://doi.org/10.1111/j.1151-2916.1984.tb19744.x.

(30) Ricceri, R.; Matteazzi, P. A Fast and Low-Cost Room Temperature Process for TiB2 Formation by Mechanosynthesis. *Materials Science and Engineering A* **2004**, *379* (1–2), 341–346. https://doi.org/10.1016/j.msea.2004.02.064.

(31) Kang, S. H.; Kim, D. J. Synthesis of Nano-Titanium Diboride Powders by Carbothermal Reduction. *J Eur Ceram Soc* **2007**, *27* (2–3), 715–718. https://doi.org/10.1016/j.jeurceramsoc.2006.04.053.

(32) Ghanbari, A.; Sakaki, M.; Faeghinia, A.; Bafghi, M. S.; Yanagisawa, K. Synthesis of Nanocrystalline TiB2 Powder from TiO2, B2O3 and Mg Reactants through Microwave-Assisted Self-Propagating High-Temperature Synthesis Method. *Bulletin of Materials Science* **2016**, *39* (4), 925–933. https://doi.org/10.1007/s12034-016-1229-4.

(33) Kim, J. W.; Shim, J. H.; Ahn, J. P.; Cho, Y. W.; Kim, J. H.; Oh, K. H. Mechanochemical Synthesis and Characterization of TiB2 and VB2 Nanopowders. *Mater Lett* **2008**, *62* (16), 2461–2464. https://doi.org/10.1016/j.matlet.2007.12.022.

(34) Radev, D. D.; Marinov, M. Properties of Tianium and Zirconium Diborides Obtained by Self-Propagated High-Temperature Synthesis. *Journal of Alloys and Compounds1* **1996**, *244*, 48–51.

(35) Radev, D. D.; Marinov, M. Properties of Titanium and Zirconium Diborides Obtained by Self-Propagated High-Temperature Synthesis. *J Alloys Compd* **1996**, *244* (1–2), 48–51. https://doi.org/10.1016/S0925-8388(96)02406-1.

(36) Wang, L.; Wixom, M. R.; Thompson, L. T. Structural and Mechanical Properties of TiB2 and TiC Prepared by Self-Propagating High-Temperature Synthesis/Dynamic Compaction. *J Mater Sci* **1994**, *29*, 534–543.

(37) Gu, Y.; Qian, Y.; Chen, L.; Zhou, F. A Mild Solvothermal Route to Nanocrystalline Titanium Diboride. *J Alloys Compd* **2003**, *352* (1–2), 325–327. https://doi.org/10.1016/S0925-8388(02)01173-8.

(38) Vallauri, D.; Atías Adrián, I. C.; Chrysanthou, A. TiC-TiB_2 Composites: A Review of Phase Relationships, Processing and Properties. *J Eur Ceram Soc* **2008**, *28* (8), 1697–1713. https://doi.org/10.1016/j.jeurceramsoc.2007.11.011.

(39) Sani, E.; Meucci, M.; Mercatelli, L.; Balbo, A.; Musa, C.; Licheri, R.; Orrù, R.; Cao, G. Titanium Diboride Ceramics for Solar Thermal Absorbers. *Solar Energy Materials and Solar Cells* **2017**, *169* (March), 313–319. https://doi.org/10.1016/j.solmat.2017.05.038.

(40) Fu, Z.; Koc, R. Pressureless Sintering of TiB2 with Low Concentration of Co Binder to Achieve Enhanced Mechanical Properties. *Materials Science and Engineering A* **2018**, *721* (February), 22–27. https://doi.org/10.1016/j.msea.2018.02.068.

(41) Wu, N.; Xue, F.; Yang, Q.; Yang, H.; Ruan, J. Microstructure and Mechanical Properties of TiB2-Based Composites with High Volume Fraction of Fe-Ni Additives Prepared by Vacuum Pressureless Sintering. *Ceram Int* **2017**, *43* (1), 1394–1401. https://doi.org/10.1016/j.ceramint.2016.10.100.

(42) Zhang, B.; Zhong, Z.; Ye, J.; Liu, Q.; Hou, Z.; Jin, Y.; Zhang, H.; Wang, Y.; Zhang, Z.; Ye, F. Microstructure and Anti-Penetration Performance of Continuous Gradient Ti/TiB–TiB2 Composite Fabricated by Spark Plasma Sintering Combined with Tape Casting. *Ceram Int* **2020**, *46* (7), 9957–9961. https://doi.org/10.1016/j.ceramint.2019.12.125.

(43) Telle, R. Analysis of Pressureless Sintering of Titanium Diboride Ceramics with Nickel, Cobalt, and Tungsten Carbide Additives. *J Eur Ceram Soc* **2019**, *39* (7), 2266–2276. https://doi.org/10.1016/j.jeurceramsoc.2019.02.036.

(44) Basu, B.; Raju, G. B.; Suri, A. K. Processing and Properties of Monolithic TiB2 Based Materials. *International Materials Reviews* **2006**, *51* (6), 352–374. https://doi.org/10.1179/174328006X102529.

(45) Liu, A. D.; Qiao, Y. J.; Liu, Y. Y. Pressureless Sintering and Properties of Boron Carbide-Titanium Diboride Composites by in-Situ Reaction. *Key Eng Mater* **2012**, *525–526* (ii), 321–324. https://doi.org/10.4028/www.scientific.net/KEM.525-526.321.

(46) Kartal, G.; Timur, S.; Urgen, M.; Erdemir, A. Electrochemical Boriding of Titanium for Improved Mechanical Properties. *Surf Coat Technol* **2010**, *204* (23), 3935–3939. https://doi.org/10.1016/j.surfcoat.2010.05.021.

(47) Martin, C.; Vivier, R.; Mathieu, R. Electrical Discharge Machinable Ceramic Composites. *Materials Science and Engineering, A* **1989**, *109*, 351–356.

(48) Fu, Z.; Koc, R. Synthesis of TiB2 from a Carbon-Coated Precursors Method. *Journal of the American Ceramic Society* **2017**, *100* (6), 2471–2481. https://doi.org/10.1111/jace.14794.

(49) Rahaman, M. N. *Ceramic Processing*, 2nd ed.; 2017. https://doi.org/10.1017/CBO9781107415324.004.

(50) Mukhopadhyay, A.; Raju, G. B.; Basu, B.; Suri, A. K. Correlation between Phase Evolution, Mechanical Properties and Instrumented Indentation Response of TiB2-Based Ceramics. *J Eur Ceram Soc* **2009**, *29* (3), 505–516. https://doi.org/10.1016/j.jeurceramsoc.2008.06.030.

(51) Murthy, T. S. R. C.; Basu, B.; Balasubramaniam, R.; Suri, A. K.; Subramanian, C.; Fotedar, R. K. Processing and Properties of TiB_2 with $MoSi_2$ Sinter-Additive: A First Report. In *Journal of the American Ceramic Society*; 2006; Vol. 89, pp 131–138. https://doi.org/10.1111/j.1551-2916.2005.00652.x.

(52) Akin, I.; Ocak, B. C.; Akarsu, M. K.; Yucel, O.; Sahin, F.; Goller, G. Comparative Investigation of the Properties of Graphene Nanoplatelet Reinforced Titanium Diboride and Niobium Diboride Ceramics. *Int J Refract Metals Hard Mater* **2022**, *103*. https://doi.org/10.1016/j.ijrmhm.2021.105761.

(53) Li, J.; Lü, X.; Lai, Y.; Li, Q.; Liu, Y. Research Progress in TiB_2 Wettable Cathode for Aluminum Reduction. *JOM* **2008**, 32–37.

(54) Clark, D. E.; Sutton, W. H. Microwave Processing. *Annual Review Materials Science* **1996**, 299–331. https://doi.org/10.1002/9781444355321.ch15.

(55) Holcombe, C. E.; Dykes, N. L. Microwave Sintering of Titanium Diboride. *J Mater Sci* **1991**, *26*, 3730–3738.

(56) Leo, S.; Tallon, C.; Franks, G. v. Pressureless Sintering of ZrB_2 Prepared by Colloidal Processing: Particle Packing, Sintering Conditions, and Additives. *Journal of the American Ceramic Society* **2016**, *99* (12), 3883–3892. https://doi.org/10.1111/jace.14433.

(57) Subramanian, C.; Murthy, T. S. R. C.; Suri, A. K. Synthesis and Consolidation of Titanium Diboride. *Int J Refract Metals Hard Mater* **2007**, *25* (4), 345–350. https://doi.org/10.1016/j.ijrmhm.2006.09.003.

(58) Dulera, I. V.; Sinha, R. K. High Temperature Reactors. *Journal of Nuclear Materials* **2008**, *383* (1–2), 183–188.

(59) Buyuk, B.; Tugrul, A. B.; Aktop, S.; Addemir, A. O. Investigation on the Effects of Boron Carbide Particle Size on Radiation Shielding Properties of Boron Carbide-Titanium Diboride Composites. In *Acta Physica Polonica A*; 2013; Vol. 123, pp 177–179. https://doi.org/10.12693/APhysPolA.123.177.

(60) Buyuk, B.; Tugrul, A. B.; Akarsu, A. C.; Addemir, A. O. *Investigation of Behaviour of Titanium Diboride Reinforced Boron Carbide-Silicon Carbide Composites against Cs-137 Gamma Radioisotope Source by Using Gamma Transmission Technique*; 2012; Vol. 121. http://www.nist.gov/pml/data/xcom/index.cfm.

(61) Mishra, R. *The Temperature Ratings Of Electronic Parts*. Electronics-Cooling.

(62) Wu, C.; Lin, F.; Pan, X.; He, Y.; Chen, G.; Cui, Z.; Liu, X.; Sun, D.; Hai, Z. TiB_2-Modified PDC Electrical Solder Joints for Electrical Interconnection in Extreme Environments. *Ceram Int* **2022**, *48* (17), 25578–25586. https://doi.org/10.1016/j.ceramint.2022.05.237.

(63) Cai, K. F.; Mueller, E.; Drasar, C.; Mrotzek, A. Sol-Gel Processing of ZnO-Coated TiB_2 Composite Powders. *Mater Lett* **2003**, *57* (26–27), 4251–4255. https://doi.org/10.1016/S0167-577X(03)00299-4.

(64) Kelly, J. P.; Finkenauer, L. R.; Roy, P.; Stolaroff, J. K.; Nguyen, D. T.; Ross, M. S.; Hoff, A. T.; Haslam, J. J. Binder Jet Additive Manufacturing of Ceramic Heat Exchangers for Concentrating Solar Power Applications with Thermal Energy Storage in Molten Chlorides. *Addit Manuf* **2022**, *56*. https://doi.org/10.1016/j.addma.2022.102937.

(65) Wu, Q.; Liang, X.; Chen, H.; Yang, L.; Xie, T.; Zou, X. Surface-Oxidized Titanium Diboride as Cocatalyst on Hematite Photoanode for Solar Water Splitting. *CrystEngComm* **2022**, *24* (12), 2251–2257. https://doi.org/10.1039/d2ce00122e.

(66) Kirshenbaum, M. J.; Richter, M. H.; Dasog, M. Electrochemical Water Oxidation in Acidic Solution Using Titanium Diboride (TiB_2) Catalyst. *ChemCatChem* **2019**, *11* (16), 3877–3881. https://doi.org/10.1002/cctc.201801736.

(67) Xue, J.; Liu, Q.; Ou, W.; Beijing, T. Sodium Expansion in Carbon/TiB_2 Cathodes during Aluminum Electrolysis. *Light Metals* **2007**, No. D, 1061–1066.

(68) Pawlek, R. P. Wettable Cathodes: An Update. In *Light Metals 2010; aluminum reduction technology*; 2010.

(69) Li, Q.; Lai, Y.; Liu, Y.; Li, J.; Yang, J.; Fang, J.; Liu, Y. Laboratory Test and Industrial Appliction of an Ambient Temperature Cured TiB2 Cathode Coating for Aluminum Electrolysis Cells. *Light Metals 2004* **2004**, 1–15.

(70) Guan, C.; Zhu, H. Theoretical Insights into the Behaviors of Sodium and Aluminum on the Cathode Titanium Diboride Surfaces. *Comput Mater Sci* **2022**, *211*. https://doi.org/10.1016/j.commatsci.2022.111535.

(71) Chen, X. J.; Shellikeri, A.; Wu, Q.; Zheng, J. P.; Hendrickson, M.; Plichta, E. J. A High-Rate Rechargeable Li-Air Flow Battery. *J Electrochem Soc* **2013**, *160* (10), A1619–A1623. https://doi.org/10.1149/2.012310jes.

(72) Yang, Y.; Sun, Q.; Li, Y.-S.; Li, H.; Fu, Z.-W. Nanostructured Diamond Like Carbon Thin Film Electrodes for Lithium Air Batteries. *J Electrochem Soc* **2011**, *158* (10), B1211. https://doi.org/10.1149/1.3623431.

(73) Williford, R. E.; Zhang, J. G. Air Electrode Design for Sustained High Power Operation of Li/Air Batteries. *J Power Sources* **2009**, *194* (2), 1164–1170. https://doi.org/10.1016/j.jpowsour.2009.06.005.

(74) Yang, X. hui; He, P.; Xia, Y. yao. Preparation of Mesocellular Carbon Foam and Its Application for Lithium/Oxygen Battery. *Electrochem commun* **2009**, *11* (6), 1127–1130. https://doi.org/10.1016/j.elecom.2009.03.029.

(75) Amine, K.; Kanno, R.; Tzeng, Y. Rechargeable Lithium Batteries and beyond: Progress, Challenges, and Future Directions. *MRS Bull* **2014**, *39* (5), 395–401. https://doi.org/10.1557/mrs.2014.62.

(76) Cheng, F.; Chen, J. Metal-Air Batteries: From Oxygen Reduction Electrochemistry to Cathode Catalysts. *Chem Soc Rev* **2012**, *41* (6), 2172–2192. https://doi.org/10.1039/c1cs15228a.

(77) Wang, Y.; Cho, S. C. Analysis of Air Cathode Perfomance for Lithium-Air Batteries. *J Electrochem Soc* **2013**, *160* (10), A1847–A1855. https://doi.org/10.1149/2.092310jes.

(78) Bae, C. J.; Erdonmez, C. K.; Halloran, J. W.; Chiang, Y. M. Design of Battery Electrodes with Dual-Scale Porosity to Minimize Tortuosity and Maximize Performance. *Advanced Materials* **2013**, *25* (9), 1254–1258. https://doi.org/10.1002/adma.201204055.

(79) Ebner, M.; Chung, D. W.; García, R. E.; Wood, V. Tortuosity Anisotropy in Lithium-Ion Battery Electrodes. *Adv Energy Mater* **2014**, *4* (5), 1–6. https://doi.org/10.1002/aenm.201301278.

(80) Wang, J.; Li, Y.; Ã, X. S. Challenges and Opportunities of Nanostructured Materials for Aprotic Rechargeable Lithium – Air Batteries. *Nano Energy* **2013**, *2* (4), 443–467. https://doi.org/10.1016/j.nanoen.2012.11.014.

(81) Mirzaeian, M.; Hall, P. J. Preparation of Controlled Porosity Carbon Aerogels for Energy Storage in Rechargeable Lithium Oxygen Batteries. *Electrochim Acta* **2009**, *54* (28), 7444–7451. https://doi.org/10.1016/j.electacta.2009.07.079.

(82) Mirzaeian, M.; Hall, P. J. Characterizing Capacity Loss of Lithium Oxygen Batteries by Impedance Spectroscopy. *J Power Sources* **2010**, *195* (19), 6817–6824. https://doi.org/10.1016/j.jpowsour.2010.04.064.

(83) Xiao, J.; Wang, D.; Xu, W.; Wang, D.; Williford, R. E.; Liu, J.; Zhang, J.-G. Optimization of Air Electrode for Li/Air Batteries. *J Electrochem Soc* **2010**, *157* (4), A487. https://doi.org/10.1149/1.3314375.

(84) Torres, A. E.; Balbuena, P. B. Exploring the LiOH Formation Reaction Mechanism in Lithium-Air Batteries. *Chemistry of Materials* **2018**, *30* (3), 708–717. https://doi.org/10.1021/acs.chemmater.7b04018.

(85) Martinez, O. A.; Sharma, A.; Sankar, B. V.; Haftka, R. T.; Blosser, M. L. Thermal Force and Moment Determination of an Integrated Thermal Protection System. *AIAA Journal* **2010**, *48* (1), 119–128. https://doi.org/10.2514/1.40678.

(86) Hidrovo, C. H.; Goodson, K. E. Active Mircofluidic Cooling of Integrated Circuits. In *Integrated Interconnect Technologies for 3D Nanoelectronic Systems*; Bakir, M. S., Meindl, J. D., Eds.; Artech House Books: Norwood, 2009; pp 293–330.

(87) McKinney, D.; Sigmund, W. Colloidal Processing Fundamentals. In *Handbook of Advanced Ceramics: Materials, Applications, Processing, and Properties: Second Edition*; Elsevier Inc., 2013; pp 911–926. https://doi.org/10.1016/B978-0-12-385469-8.00049-6.

(88) Chen, X.; Liu, C.; Chen, H.; Cui, Y.; Liu, J.; Chen, Z.; Wang, L.; Wu, Y.; Wang, H. Enhanced Strength and Ductility of TiB2/AA7034 Composite by Accumulative Orthogonal Extrusion Process. *Materials Science and Engineering A* **2022**, *848*. https://doi.org/10.1016/j.msea.2022.143413.

(89) Leo, S.; Tallon, C.; Franks, G. v. Aqueous and Nonaqueous Colloidal Processing of Difficult-to-Densify Ceramics: Suspension Rheology and Particle Packing. *Journal of the American Ceramic Society* **2014**, *97* (12), 3807–3817. https://doi.org/10.1111/jace.13220.

(90) Israelachvili, J. N. *Intermolecular and Surface Forces*, third.; Elsevier: Santa Barbara, 2011.

(91) Rahaman, M. N. Science of Colloidal Processing. *Ceramic Processing* **2018**, 141–191. https://doi.org/10.1201/9781315276045-4.

(92) Leo, S.; Tallon, C.; Stone, N.; Franks, G. v. Near-Net-Shaping Methods for Ceramic Elements of (Body) Armor Systems. *Journal of the American Ceramic Society* **2014**, *97* (10), 3013–3033. https://doi.org/10.1111/jace.13192.

(93) TALLON, C.; FRANKS, G. v. Recent Trends in Shape Forming from Colloidal Processing: A Review. *Journal of the Ceramic Society of Japan* **2011**, *119* (1387), 147–160. https://doi.org/10.2109/jcersj2.119.147.

(94) Moreno, R. Colloidal Processing of Ceramics and Composites. *Advances in Applied Ceramics* **2012**, *111* (5–6), 246–253. https://doi.org/10.1179/1743676111Y.0000000075.

(95) Franks, G. v.; Tallon, C.; Studart, A. R.; Sesso, M. L.; Leo, S. Colloidal Processing: Enabling Complex Shaped Ceramics with Unique Multiscale Structures. *Journal of the American Ceramic Society* **2017**, *100* (2), 458–490. https://doi.org/10.1111/jace.14705.

(96) Qiao, Y.; Liu, Y.; Liu, A.; Wang, Y. Boron Carbide Green Sheet Processed by Environmental Friendly Non-Aqueous Tape Casting. *Ceram Int* **2012**, *38* (3), 2319–2324. https://doi.org/10.1016/j.ceramint.2011.10.083.

(97) Krishnan, B.; Natarajan, R. Dispersion and Tape Casting of Silicon Carbide through Aqueous Route. *J Mater Sci* **2005**, *40* (20), 5511–5516. https://doi.org/10.1007/s10853-005-1917-8.

(98) Luo, Z.; Lv, Z.; Jiang, D.; Zhang, J. Aqueous Tape Casting of Boron Carbide Ceramic. *Ceram Int* **2013**, *39* (2), 2123–2126. https://doi.org/10.1016/j.ceramint.2012.07.048.

(99) Lü, Z.; Jiang, D.; Zhang, J.; Lin, Q. Aqueous Tape Casting of Zirconium Diboride. *Journal of the American Ceramic Society* **2009**, *92* (10), 2212–2217. https://doi.org/10.1111/j.1551-2916.2009.03222.x.

(100) Coronas, J.; Santamaria, J. Catalytic Reactors Based on Porous Ceramic Membranes. *Catal Today* **1999**, 377–389.

(101) Benfer, S.; Árki, P.; Tomandl, G. Ceramic Membranes for Filtration Applications - Preparation and Characterization. *Advanced Engineering Materials*. July 2004, pp 495–500. https://doi.org/10.1002/adem.200400577.

(102) Sánchez-Herencia, A. J.; Gurauskis, J.; Baudín, C. Processing of Al_2O_3/Y-TZP Laminates from Water-Based Cast Tapes. *Compos B Eng* **2006**, *37* (6), 499–508. https://doi.org/10.1016/j.compositesb.2006.02.002.

(103) Chartier, T.; Merle, D.; Besson, J. L. Laminar Ceramic Composites. *J Eur Ceram Soc* **1995**, *15* (2), 101–107. https://doi.org/10.1016/0955-2219(95)93055-8.

(104) Bitter, J. G. A. Types of Membrane Separation Processes, Mechanisms of Separation. In *Transport Mechanisms in Membrane Separation Processes*; Luss, D., Ed.; Springer Science+Business Media, LLC, 1991; pp 3–9.

(105) Heunisch, A.; Dellert, A.; Roosen, A. Effect of Powder, Binder and Process Parameters on Anisotropic Shrinkage in Tape Cast Ceramic Products. *J Eur Ceram Soc* **2010**, *30* (16), 3397–3406. https://doi.org/10.1016/j.jeurceramsoc.2010.08.012.

(106) Nishihora, R. K.; Rachadel, P. L.; Quadri, M. G. N.; Hotza, D. Manufacturing Porous Ceramic Materials by Tape Casting—A Review. *J Eur Ceram Soc* **2018**, *38* (4), 988–1001. https://doi.org/10.1016/j.jeurceramsoc.2017.11.047.

(107) Schafbauer, W.; Schulze-Küppers, F.; Baumann, S.; Meulenberg, W. A.; Menzler, N. H.; Buchkremer, H. P.; Stöver, D. Tape Casting as a Multi Purpose Shaping Technology for Different Applications in Energy Issues. *Materials Science Forum* **2012**, *706–709*, 1035–1040. https://doi.org/10.4028/www.scientific.net/msf.706-709.1035.

(108) Fu, Y. P.; Liu, Y. C.; Hu, S. H. Aqueous Tape Casting and Crystallization Behavior of Gadolinium-Doped Ceria. *Ceram Int* **2009**, *35* (8), 3153–3159. https://doi.org/10.1016/j.ceramint.2009.05.002.

(109) Nishihora, R. K.; Quadri, M. G. N.; Hotza, D.; Rezwan, K.; Wilhelm, M. Tape Casting of Polysiloxane-Derived Ceramic with Controlled Porosity and Surface Properties. *J Eur Ceram Soc* **2018**, *38* (15), 4899–4905. https://doi.org/10.1016/j.jeurceramsoc.2018.07.016.

(110) Jia, Y.; Mehta, S. T.; Li, R.; Rahman Chowdhury, M. A.; Horn, T.; Xu, C. Additive Manufacturing of ZrB2–ZrSi2 Ultra-High Temperature Ceramic Composites Using an Electron Beam Melting Process. *Ceram Int* **2021**, *47* (2), 2397–2405. https://doi.org/10.1016/j.ceramint.2020.09.082.

(111) Anokhin, A.; Strelnikova, S.; Ermakova, E.; Chuvikina, M.; Potyomkina, E.; Fefelov, M. Investigation of Polymer Materials Properties to Use for Additive Manufacturing. *J Phys Conf Ser* **2021**, *1758* (1). https://doi.org/10.1088/1742-6596/1758/1/012001.

(112) Li, Z.; Chen, Q.; Jiao, B.; Wang, Q.; Zhang, H.; Jia, Q.; Zhang, S.; Liu, J. Direct Laser Powder-Bed Fusion Additive Manufacturing of Complex-Shaped TiB_2-B_4C Composite with Ultra-Fine Eutectic Microstructure and Outstanding Mechanical Performances. *J Eur Ceram Soc* **2023**, *43* (3), 1230–1236. https://doi.org/10.1016/j.jeurceramsoc.2022.10.071.

(113) Peters, A. B.; Zhang, D.; Nagle, D. C.; Spicer, J. B. Reactive Two-Step Additive Manufacturing of Ultra-High Temperature Carbide Ceramics. *Addit Manuf* **2023**, *61*. https://doi.org/10.1016/j.addma.2022.103318.

(114) Yang, Q.; Xia, C.; Wang, H.; Zhou, M.; Gao, S.; Li, B.; Liu, S. Microstructure and Mechanical Properties of TiB_2/$AlSi_7Mg_{0.6}$ Composites Fabricated by Wire and Arc Additive Manufacturing Based on Cold Metal Transfer (WAAM-CMT). *Materials* **2022**, *15* (7). https://doi.org/10.3390/ma15072440.

(115) Promakhov, V.; Matveev, A.; Klimova-Korsmik, O.; Schulz, N.; Bakhmat, V.; Babaev, A.; Vorozhtsov, A. Structure and Properties of Metal-Matrix Composites Based on an Inconel 625–TiB2System Fabricated by Additive Manufacturing. *Metals (Basel)* **2022**, *12* (3). https://doi.org/10.3390/met12030525.

(116) Lu, Y.; Jiang, L.; Shi, L.; Gao, M. Microstructure and Mechanical Properties of TiB_2 Reinforced Al2319 Matrix Composites Produced Using Laser-Arc Hybrid Additive Manufacturing; SPIE-Intl Soc Optical Eng, 2022; p 37. https://doi.org/10.1117/12.2656059.

(117) Liu, G.; Yan, C.; Jin, H. Colloidal Processing of Complex-Shaped ZrB_2-Based Ultra-High-Temperature Ceramics: Progress and Prospects. *Materials*. MDPI April 1, 2022. https://doi.org/10.3390/ma15082886.

(118) Kim, S. Y.; Sesso, M. L.; Franks, G. V. Effect of Internal Lattice Structure on the Flexural Strength of 3D Printed Hierarchical Porous Ultra-High Temperature Ceramic (ZrB2). *J Eur Ceram Soc* **2023**, *43* (5), 1762–1776. https://doi.org/10.1016/j.jeurceramsoc.2022.12.027.

(119) Xu, X.; Zhang, J.; Jiang, P.; Liu, D.; Jia, X.; Wang, X.; Zhou, F. Direct Ink Writing of Aluminum-Phosphate-Bonded Al_2O_3 Ceramic with Ultra-Low Dimensional Shrinkage. *Ceram Int* **2022**, *48* (1), 864–871. https://doi.org/10.1016/j.ceramint.2021.09.168.

(120) Sesso, M. L.; Slater, S.; Thornton, J.; Franks, G. V. Direct Ink Writing of Hierarchical Porous Ultra-High Temperature Ceramics (ZrB2). *Journal of the American Ceramic Society* **2021**, *104* (10), 4977–4990. https://doi.org/10.1111/jace.17911.

(121) Patwardhan, J. S.; Cannon, W. R. Factors Influencing Anisotropic Sintering Shrinkage in Tape-Cast Alumina: Effect of Processing Variables. *Journal of the American Ceramic Society* **2006**, *89* (10), 3019–3026. https://doi.org/10.1111/j.1551-2916.2006.01169.x.

(122) Bargardi, F. L.; Le Ferrand, H.; Libanori, R.; Studart, A. R. Bio-Inspired Self-Shaping Ceramics. *Nat Commun* **2016**, *7*. https://doi.org/10.1038/ncomms13912.

(123) Richerson, D. W. *Modern Ceramic Engineering : Properties, Processing, and Use in Design*; CRC Taylor & Francis,: Boca Raton, FL :, 2006.

(124) Wu, M.; Messing, G. L. Fabrication of Oriented SiC-Whisker-Reinforced Mullite Matrix Composites by Tape Casting. *Journal of the American Ceramic Society* **1994**, *77* (10), 2586–2592. https://doi.org/10.1111/j.1151-2916.1994.tb04646.x.

(125) Sciti, D.; Pienti, L.; Fabbriche, D. D.; Guicciardi, S.; Silvestroni, L. Combined Effect of SiC Chopped Fibers and SiC Whiskers on the Toughening of ZrB_2. *Ceram Int* **2014**, *40* (3), 4819–4826. https://doi.org/10.1016/j.ceramint.2013.09.031.

(126) Liang Xu, Chuanzhen Huang, Hanlian Liu, Bin Zou, Hongtao Zhu, Guolong Zhao, J. W. Study on In-Situ Synthesis of ZrB_2 Whiskers in ZrB_2–ZrC Matrix Powder for Ceramic Cutting Tools. *Int J Refract Metals Hard Mater* **2013**, *37*, 98–105.

(127) Liu, B.; Huang, C.; Gu, M.; Zhu, H.; Liu, H. Preparation and Mechanical Properties of in Situ Growth TiC Whiskers Toughening Al_2O_3 Ceramic Matrix Composite. *Materials Science and Engineering A* **2007**, *460–461*, 146–148. https://doi.org/10.1016/j.msea.2007.01.009.

(128) Bhattacharyya, D. S. Orientation of Mineral Lineation along the Flow Direction in Rocks. *Tectonphysics* **1965**, *3* (1), 29–33.

(129) Watanabe, H.; Kimura, T.; Yamaguchi, T. Particle Orientation During Tape Casting in the Fabrication of Grain-Oriented Bismuth Titanate. *Journal of the American Ceramic Society* **1989**, *72* (2), 289–293. https://doi.org/10.1111/j.1151-2916.1989.tb06116.x.

(130) Fu, X.; Liu, M.; Xu, K.; Chen, S.; Shi, Y.; Fu, Z.; Huang, Y.; Chen, H.; Yao, R. The In-Situ Observation of Grain Rotation and Microstructure Evolution Induced by Electromigration in Sn-3.0Ag-0.5Cu Solder Joints. *Materials* **2020**, *13* (23), 1–10. https://doi.org/10.3390/ma13235497.

(131) Guilmeau, E.; Itahara, H.; Tani, T.; Chateigner, D.; Grebille, D. Quantitative Texture Analysis of Grain-Aligned [Ca2 Co O3] 0.62 [Co O2] Ceramics Processed by the Reactive-Templated Grain Growth Method. *J Appl Phys* **2005**, *97* (6). https://doi.org/10.1063/1.1829398.

(132) Walton, R. L.; Vaudin, M. D.; Hofer, A. K.; Kupp, E. R.; Meyer, R. J.; Messing, G. L. Tailoring Particle Alignment and Grain Orientation during Tape Casting and Templated Grain Growth. *Journal of the American Ceramic Society* **2019**, *102* (5), 2405–2414. https://doi.org/10.1111/jace.16144.

(133) Polfer, P.; Fu, Z.; Breinlinger, T.; Roosen, A.; Kraft, T. Influence of the Doctor Blade Shape on Tape Casting—Comparison Between Analytical, Numerical, and Experimental Results. *Journal of the American Ceramic Society* **2016**, *99* (10), 3233–3240. https://doi.org/10.1111/jace.14343.

(134) Shi, Z.; Zhang, P.; Lou, Z.; Qin, M.; Xu, J.; Yan, H.; Gao, F. Grain Orientation Evolution and Thermoelectric Properties of Textured (Ca0.87Ag0.1La0.03)3Co4O9 Ceramics Prepared by Tape Casting. *Ceram Int* **2021**, *47* (6), 8365–8374. https://doi.org/10.1016/j.ceramint.2020.11.199.

(135) Raj, P. M.; Cannon, W. R. Anisotropic Shrinkage in Tape-Cast Alumina: Role of Processing Parameters and Particle Shape. *Journal of the American Ceramic Society* **1999**, *82* (10), 2619–2625. https://doi.org/10.1111/j.1151-2916.1999.tb02132.x.

(136) Chantaramee, N.; Tanaka, S.; Uemasu, K. Development of Packing Structure of Powder Particles in Tape Casting. *Journal of the Ceramic Society of Japan* **2007**, *115* (2), 136–140.

(137) Raj, P. M. Origin of Anisotropic Shrinkage in Tape Cast Ceramics. dissertation, Rutgers, The State University of New Jersey, New Brunswick, 1999.

(138) Shaler, S. M.; Mi, H. *Comparing Two Measures of Flake Alignment*; 1991; Vol. 26.

(139) Chu, K.; Wang, X. hu; Wang, F.; Li, Y. biao; Huang, D. jian; Liu, H.; Ma, W. lin; Liu, F. xia; Zhang, H. Largely Enhanced Thermal Conductivity of Graphene/Copper Composites with Highly Aligned Graphene Network. *Carbon N Y* **2018**, *127*, 102–112. https://doi.org/10.1016/j.carbon.2017.10.099.

(140) Feng, G.; Qiao, R.; Huang, J.; Dai, S.; Sumpter, B. G.; Meunier, V. The Importance of Ion Size and Electrode Curvature on Electrical Double Layers in Ionic Liquids. *Physical Chemistry Chemical Physics* **2011**, *13* (3), 1152–1161. https://doi.org/10.1039/c0cp02077j.

(141) Cetinkaya, S. Synthesis of Fine Zirconium Carbide Powder by Carbothermal Reaction of Carbon-Coated Zirconia Particles. **2017**, No. July, 5444–5449. https://doi.org/10.1111/jace.15118.

(142) Anubhav, J.; Sacks, M. D.; Wang, C.-A.; Middlemas, M.; Cheng, Z. Processing of Nanocrystalline Zirconium Carbide Powders.

(143) Park, D. S.; Hahn, B. D.; Baik, D. J. Microstructure and Properties of Sintered Reaction Bonded Silicon Nitride with Aligned Whisker Seeds. *Key Eng Mater* **2005**, *287*, 271–276. https://doi.org/10.4028/www.scientific.net/KEM.287.271.

(144) Park, D.-S.; Kim, C.-W. *A Modification of Tape Casting for Aligning the Whiskers*.

(145) Xu, L.; Huang, C.; Liu, H.; Zou, B.; Zhu, H.; Zhao, G.; Wang, J. Study on the Synthesis and Growth Mechanisms of the Refractory ZrC Whiskers. *Int J Refract Metals Hard Mater* **2014**, *42*, 116–119. https://doi.org/10.1016/j.ijrmhm.2013.08.011.

(146) Lotgering, F. K. Topotactical Reactions with Ferrimagnetic Oxides Having Hexagonal Crystal Structures. *Journal of Inorganic Nuclear Chemistry* **1959**, *9*, 113–123.

(147) Chung, D. W.; Ebner, M.; Ely, D. R.; Wood, V.; Edwin García, R. Validity of the Bruggeman Relation for Porous Electrodes. *Model Simul Mat Sci Eng* **2013**, *21* (7). https://doi.org/10.1088/0965-0393/21/7/074009.

(148) Ebner, M.; Wood, V. Tool for Tortuosity Estimation in Lithium Ion Battery Porous Electrodes. *J Electrochem Soc* **2015**, *162* (2), A3064–A3070. https://doi.org/10.1149/2.0111502jes.

(149) *Standard Test Methods for Determination of Fracture Toughness of Advanced Ceramics at Ambient Temperature 1*. https://doi.org/10.1520/C1421-18.

(150) Jabbari, M.; Bulatova, R.; Tok, A. I. Y.; Bahl, C. R. H.; Mitsoulis, E.; Hattel, J. H. Ceramic Tape Casting: A Review of Current Methods and Trends with Emphasis on Rheological Behaviour and Flow Analysis. *Mater Sci Eng B Solid State Mater Adv Technol* **2016**, *212*, 39–61. https://doi.org/10.1016/j.mseb.2016.07.011.

(151) Fu, Z.; Eckstein, U.; Dellert, A.; Roosen, A. In Situ Study of Mass Loss, Shrinkage and Stress Development during Drying of Cast Colloidal Films. *J Eur Ceram Soc* **2015**, *35* (10), 2883–2893. https://doi.org/10.1016/j.jeurceramsoc.2015.03.029.

(152) Akbari-Fakhrabadi, A.; Mangalaraja, R. V.; Sanhueza, F. A.; Avila, R. E.; Ananthakumar, S.; Chan, S. H. Nanostructured Gd-CeO_2 Electrolyte for Solid Oxide Fuel Cell by Aqueous Tape Casting. *J Power Sources* **2012**, *218*, 307–312. https://doi.org/10.1016/j.jpowsour.2012.07.005.

(153) Lyklema, J. *Fundamentals of Interface and Colloid Science Volume II: Solid-Liquid Interfaces*; Academic Press: San Diego, 1995.

(154) Wu, H. H.; Hsu, K. C. Effect of PH on the Properties of Barium Titanate Slurries with an Anionic Dispersant. *J Appl Polym Sci* **2006**, *101* (2), 1082–1088. https://doi.org/10.1002/app.23815.

(155) Bitterlich, B.; Lutz, C.; Roosen, A. Rheological Characterization of Water-Based Slurries for the Tape Casting Process. *Ceram Int* **2002**, *28* (6), 675–683. https://doi.org/10.1016/S0272-8842(02)00027-5.

(156) Belon, R.; Boulesteix, R.; Geffroy, P.-M.; Maître, A.; Sallé, C.; Chartier, T. Tape Casting of Multilayer YAG-Nd:YAG Transparent Ceramics for Laser Applications: Study of Green Tapes Properties. *J Eur Ceram Soc* **2019**.

(157) Yu, M.; Zhang, J.; Li, X.; Liang, H.; Zhong, H.; Li, Y.; Duan, Y.; Jiang, D. L.; Liu, X.; Huang, Z. Optimization of the Tape Casting Process for Development of High Performance

Alumina Ceramics. *Ceram Int* **2015**, *41* (10), 14845–14853. https://doi.org/10.1016/j.ceramint.2015.08.010.

(158) Sacks, M. D.; Wang, C. A.; Yang, Z.; Jain, A. Carbothermal Reduction Synthesis of Nanocrystalline Zirconium Carbide and Hafnium Carbide Powders Using Solution-Derived Precursors. *J Mater Sci* **2004**, *39* (19), 6057–6066. https://doi.org/10.1023/B:JMSC.0000041702.76858.a7.

(159) Cetinkaya, S. Synthesis of Fine Zirconium Carbide Powder by Carbothermal Reaction of Carbon-Coated Zirconia Particles. **2017**, No. July, 5444–5449. https://doi.org/10.1111/jace.15118.

(160) Yan, N.; Fu, Q.; Li, K.; Hu, D.; Xie, W.; Wang, W.; Zhang, Y.; Zhuang, L.; Zhou, L.; Zhang, J.; Shi, X. Catalyst-Free in Situ Synthesis of ZrC Nanowires with Excellent Thermal Stability. *Journal of the American Ceramic Society* **2020**, *103* (10), 5825–5836. https://doi.org/10.1111/jace.17206.

(161) Yan, N.; Fu, Q.; Li, K.; Hu, D.; Xie, W.; Wang, W.; Zhang, Y.; Zhuang, L.; Zhou, L.; Zhang, J.; Shi, X. Catalyst-Free in Situ Synthesis of ZrC Nanowires with Excellent Thermal Stability. *Journal of the American Ceramic Society* **2020**, *103* (10), 5825–5836. https://doi.org/10.1111/jace.17206.

(162) Kim, J. G.; Park, S. J.; Park, J. Y.; Choi, D. J. The Effect of Temperature on the Growth and Properties of Chemical Vapor Deposited ZrC Films on SiC-Coated Graphite Substrates. *Ceram Int* **2015**, *41* (1, Part A), 211–216. https://doi.org/https://doi.org/10.1016/j.ceramint.2014.08.060.

(163) Li, K.; Zhou, X.; Zhao, Z.; Chen, C.; Wang, C.; Ren, B.; Zhang, L. Synthesis of Zirconium Carbide Whiskers by a Combination of Microwave Hydrothermal and Carbothermal Reduction. *J Solid State Chem* **2018**, *258*, 383–390. https://doi.org/https://doi.org/10.1016/j.jssc.2017.11.002.

(164) Yaghi, O. M.; O'Keeffe, M.; Ockwig, N. W.; Chae, H. K.; Eddaoudi, M.; Kim, J. Reticular Synthesis and the Design of New Materials. *Nature* **2003**, *423* (6941), 705–714. https://doi.org/10.1038/nature01650.

(165) Kitagawa, S.; Kitaura, R.; Noro, S. I. Functional Porous Coordination Polymers. *Angewandte Chemie - International Edition* **2004**, *43* (18), 2334–2375. https://doi.org/10.1002/anie.200300610.

(166) MacGillivray, L. R. *Metal-Organic Frameworks : Design and Application*; Wiley, 2010.

(167) Tranchemontagne, D. J.; Mendoza-Cortés, J. L.; O'Keeffe, M.; Yaghi, O. M. Secondary Building Units, Nets and Bonding in the Chemistry of Metal-Organic Frameworks. *Chem Soc Rev* **2009**, *38* (5), 1257–1283. https://doi.org/10.1039/b817735j.

(168) Furukawa, H.; Cordova, K. E.; O'Keeffe, M.; Yaghi, O. M. The Chemistry and Applications of Metal-Organic Frameworks. *Science (1979)* **2013**, *341* (6149). https://doi.org/10.1126/science.1230444.

(169) Huelsenbeck, L.; Westendorff, K. S.; Gu, Y.; Marino, S.; Jung, S.; Epling, W. S.; Giri, G. Modulating and Orienting an Anisotropic Zn-Based Metal Organic Framework for Selective CH_4/CO_2 Gas Separation. *Crystals (Basel)* **2019**, *9* (1), 20. https://doi.org/10.3390/cryst9010020.

(170) Bloch, E. D.; Queen, W. L.; Hudson, M. R.; Mason, J. A.; Xiao, D. J.; Murray, L. J.; Flacau, R.; Brown, C. M.; Long, J. R. Hydrogen Storage and Selective, Reversible O2Adsorption in a Metal–Organic Framework with Open Chromium(II) Sites. *Angewandte Chemie - International Edition* **2016**, *55* (30), 8605–8609. https://doi.org/10.1002/anie.201602950.

(171) Hu, Y. H.; Zhang, L. Hydrogen Storage in Metal-Organic Frameworks. *Advanced Materials*. John Wiley & Sons, Ltd May 2010, pp E117–E130. https://doi.org/10.1002/adma.200902096.

(172) Rowsell, J. L. C.; Spencer, E. C.; Eckert, J.; Howard, J. A. K.; Yaghi, O. M. Chemistry: Gas Adsorption Sites in a Large-Pore Metal-Organic Framework. *Science (1979)* **2005**, *309* (5739), 1350–1354. https://doi.org/10.1126/science.1113247.

(173) Horcajada, P.; Serre, C.; Vallet-Regí, M.; Sebban, M.; Taulelle, F.; Férey, G. Metal-Organic Frameworks as Efficient Materials for Drug Delivery. *Angewandte Chemie - International Edition* **2006**, *45* (36), 5974–5978. https://doi.org/10.1002/anie.200601878.

(174) Della Rocca, J.; Liu, D.; Lin, W. Nanoscale Metal-Organic Frameworks for Biomedical Imaging and Drug Delivery. *Acc Chem Res* **2011**, *44* (10), 957–968. https://doi.org/10.1021/ar200028a.

(175) Ricco, R.; Pfeiffer, C.; Sumida, K.; Sumby, C. J.; Falcaro, P.; Furukawa, S.; Champness, N. R.; Doonan, C. J. Emerging Applications of Metal-Organic Frameworks. *CrystEngComm* **2016**, *18*, 6532–6542. https://doi.org/10.1039/c6ce01030j.

(176) Ma, L.; Abney, C.; Lin, W. Enantioselective Catalysis with Homochiral Metal-Organic Frameworks. *Chem Soc Rev* **2009**, *38* (5), 1248–1256. https://doi.org/10.1039/b807083k.

(177) Lee, J.; Farha, O. K.; Roberts, J.; Scheidt, K. A.; Nguyen, S. T.; Hupp, J. T. Metal-Organic Framework Materials as Catalysts. *Chem Soc Rev* **2009**, *38* (5), 1450–1459. https://doi.org/10.1039/b807080f.

(178) Farha, O. K.; Shultz, A. M.; Sarjeant, A. A.; Nguyen, S. T.; Hupp, J. T. Active-Site-Accessible, Porphyrinic Metal-Organic Framework Materials. *J Am Chem Soc* **2011**, *133* (15), 5652–5655. https://doi.org/10.1021/ja111042f.

(179) Wu, P.; Guo, X.; Cheng, L.; He, C.; Wang, J.; Duan, C. Photoactive Metal-Organic Framework and Its Film for Light-Driven Hydrogen Production and Carbon Dioxide Reduction. *Inorg Chem* **2016**, *55* (16), 8153–8159. https://doi.org/10.1021/acs.inorgchem.6b01267.

(180) Dhakshinamoorthy, A.; Asiri, A. M.; García, H. Metal-Organic Framework (MOF) Compounds: Photocatalysts for Redox Reactions and Solar Fuel Production. *Angewandte Chemie - International Edition*. Wiley-Blackwell April 2016, pp 5414–5445. https://doi.org/10.1002/anie.201505581.

(181) Kent, C. A.; Mehl, B. P.; Ma, L.; Papanikolas, J. M.; Meyer, T. J.; Lin, W. Energy Transfer Dynamics in Metal-Organic Frameworks. *J Am Chem Soc* **2010**, *132* (37), 12767–12769. https://doi.org/10.1021/ja102804s.

(182) Shekhah, O.; Belmabkhout, Y.; Chen, Z.; Guillerm, V.; Cairns, A.; Adil, K.; Eddaoudi, M. Made-to-Order Metal-Organic Frameworks for Trace Carbon Dioxide Removal and Air Capture. *Nat Commun* **2014**, *5* (1), 1–7. https://doi.org/10.1038/ncomms5228.

(183) McDonald, T. M.; Lee, W. R.; Mason, J. A.; Wiers, B. M.; Hong, C. S.; Long, J. R. Capture of Carbon Dioxide from Air and Flue Gas in the Alkylamine-Appended Metal-Organic Framework Mmen-Mg 2(Dobpdc). *J Am Chem Soc* **2012**, *134* (16), 7056–7065. https://doi.org/10.1021/ja300034j.

(184) Liu, J.; Wei, Y.; Zhao, Y. Trace Carbon Dioxide Capture by Metal-Organic Frameworks. *ACS Sustain Chem Eng* **2019**, *7* (1), 82–93. https://doi.org/10.1021/acssuschemeng.8b05590.

(185) Mason, J. A.; Sumida, K.; Herm, Z. R.; Krishna, R.; Long, J. R. Evaluating Metal-Organic Frameworks for Post-Combustion Carbon Dioxide Capture via Temperature Swing Adsorption. *Energy Environ Sci* **2011**, *4* (8), 3030–3040. https://doi.org/10.1039/c1ee01720a.

(186) Yap, M. H.; Fow, K. L.; Chen, G. Z. Synthesis and Applications of MOF-Derived Porous Nanostructures. *Green Energy and Environment* **2017**, *2* (3), 218–245. https://doi.org/10.1016/j.gee.2017.05.003.

(187) Liu, B.; Shioyama, H.; Akita, T.; Xu, Q. Metal-Organic Framework as a Template for Porous Carbon Synthesis. *J Am Chem Soc* **2008**, *130* (16), 5390–5391. https://doi.org/10.1021/ja7106146.

(188) Zhang, J.; An, B.; Hong, Y.; Meng, Y.; Hu, X.; Wang, C.; Lin, J.; Lin, W.; Wang, Y. Pyrolysis of Metal-Organic Frameworks to Hierarchical Porous Cu/Zn-Nanoparticle@carbon Materials for Efficient CO2 Hydrogenation. *Mater Chem Front* **2017**, *1* (11), 2405–2409. https://doi.org/10.1039/c7qm00328e.

(189) Nakatsuka, K.; Yoshii, T.; Kuwahara, Y.; Mori, K.; Yamashita, H. Controlled Pyrolysis of Ni-MOF-74 as a Promising Precursor for the Creation of Highly Active Ni Nanocatalysts in Size-Selective Hydrogenation. *Chemistry - A European Journal* **2018**, *24* (4), 898–905. https://doi.org/10.1002/chem.201704341.

(190) Li, A.; Qian, B.; Zhong, M.; Liu, Y.; Chang, Z.; Bu, X. H. An Insight into the Pyrolysis Process of Metal-Organic Framework Templates/Precursors to Construct Metal Oxide Anode Materials for Lithium-Ion Batteries. *Mater Chem Front* **2019**, *3* (7), 1398–1405. https://doi.org/10.1039/c9qm00098d.

(191) Xia, W.; Mahmood, A.; Zou, R.; Xu, Q. Metal-Organic Frameworks and Their Derived Nanostructures for Electrochemical Energy Storage and Conversion. *Energy Environ Sci* **2015**, *8* (7), 1837–1866. https://doi.org/10.1039/c5ee00762c.

(192) Wang, Y. C.; Li, W. B.; Zhao, L.; Xu, B. Q. MOF-Derived Binary Mixed Metal/Metal Oxide @carbon Nanoporous Materials and Their Novel Supercapacitive Performances. *Physical Chemistry Chemical Physics* **2016**, *18* (27), 17941–17948. https://doi.org/10.1039/c6cp02374f.

(193) Zeng, G.; Chen, Y.; Chen, L.; Xiong, P.; Wei, M. Hierarchical Cerium Oxide Derived from Metal-Organic Frameworks for High Performance Supercapacitor Electrodes. *Electrochim Acta* **2016**, *222*, 773–780. https://doi.org/10.1016/j.electacta.2016.11.035.

(194) Ren, J.; Langmi, H. W.; North, B. C.; Mathe, M.; Bessarabov, D. Modulated Synthesis of Zirconium-Metal Organic Framework (Zr-MOF) for Hydrogen Storage Applications. *Int J Hydrogen Energy* **2014**, *39* (2), 890–895. https://doi.org/10.1016/j.ijhydene.2013.10.087.

(195) Cai, M.; Loague, Q. R.; Zhu, J.; Lin, S.; Usov, P. M.; Morris, A. J. Ruthenium-Polypyridyl Doped Zirconium Metal–Organic Frameworks for Solid-State Electrochemiluminescence. *Dalton Transactions* **2018**, *47* (46), 16807–16812. https://doi.org/10.1039/C8DT03906B.

(196) Carrasco, S.; Sanz-Marco, A.; Martín-Matute, B. Fast and Robust Synthesis of Metalated PCN-222 and Their Catalytic Performance in Cycloaddition Reactions with CO_2. *Organometallics* **2019**, *38* (18), 3429–3435. https://doi.org/10.1021/acs.organomet.9b00273.

(197) Jeong, E. Y.; Burri, A.; Lee, S. Y.; Park, S. E. Synthesis and Catalytic Behavior of Tetrakis(4-Carboxyphenyl) Porphyrin-Periodic Mesoporous Organosilica. *J Mater Chem* **2010**, *20* (48), 10869–10875. https://doi.org/10.1039/c0jm02591g.

(198) Sacks, M. D.; Wang, C. A.; Yang, Z.; Jain, A. Carbothermal Reduction Synthesis of Nanocrystalline Zirconium Carbide and Hafnium Carbide Powders Using Solution-Derived Precursors. *J Mater Sci* **2004**, *39* (19), 6057–6066. https://doi.org/10.1023/B:JMSC.0000041702.76858.a7.

(199) Anubhav, J.; Sacks, M. D.; Wang, C.-A.; Middlemas, M.; Cheng, Z. Processing of Nanocrystalline Zirconium Carbide Powders.

(200) Fernández Guillermet, A. Analysis of Thermochemical Properties and Phase Stability in the Zirconium-Carbon System. *J Alloys Compd* **1995**, *217* (1), 69–89. https://doi.org/10.1016/0925-8388(94)01310-E.

(201) Pierson, H. O. Carbides of Group IV: Titanium, Zirconium, and Hafnium Carbides. *Handbook of Refractory Carbides and Nitrides* **1996**, *0*, 55–80. https://doi.org/10.1016/B978-081551392-6.50005-2.

(202) Korklan, N.; Hilmas, G. E.; Fahrenholtz, W. G. Processing and Room Temperature Mechanical Properties of a Zirconium Carbide Ceramic. **2020**, No. April, 1–6. https://doi.org/10.1111/jace.17442.

(203) Gasparrini, C.; Rana, D. sham; Le Brun, N.; Horlait, D.; Markides, C. N.; Farnan, I.; Lee, W. E. On the Stoichiometry of Zirconium Carbide. *Sci Rep* **2020**, *10* (1), 1–12. https://doi.org/10.1038/s41598-020-63037-0.

(204) Wang, L.; Zhang, F.; Dai, W.; Cheng, Q.; Zhang, K.; Wu, Y.; Xiong, Y.; Lu, Y.; Wu, Q.; He, X. The Synthesis of Zirconium Carbide Nanoparticles by Lithium Thermal Reduction of Zirconium Dioxide and Waste Plastic. *Chem Lett* **2019**, *48* (6), 604–606. https://doi.org/10.1246/cl.190075.

(205) Chen, L.; Iwamoto, C.; Omurzak, E.; Takebe, S.; Okudera, H.; Yoshiasa, A.; Sulaimankulova, S.; Mashimo, T. Synthesis of Zirconium Carbide (ZrC) Nanoparticles Covered with Graphitic "Windows" by Pulsed Plasma in Liquid. *RSC Adv* **2011**, *1* (6), 1083–1088. https://doi.org/10.1039/c1ra00194a.

(206) Epley, C. C.; Roth, K. L.; Lin, S.; Ahrenholtz, S. R.; Grove, T. Z.; Morris, A. J. Cargo Delivery on Demand from Photodegradable MOF Nano-Cages. *Dalton Transactions* **2017**, *46* (15), 4917–4922. https://doi.org/10.1039/C6DT04787D.

(207) Wang, L.; Si, L.; Zhu, Y.; Qian, Y. Solid-State Reaction Synthesis of ZrC from Zirconium Oxide at Low Temperature. *Int J Refract Metals Hard Mater* **2013**, *38*, 134–136. https://doi.org/10.1016/j.ijrmhm.2012.12.001.

(208) Korklan, N.; Hilmas, G. E.; Fahrenholtz, W. G. Processing and Room Temperature Mechanical Properties of a Zirconium Carbide Ceramic. **2020**, No. April, 1–6. https://doi.org/10.1111/jace.17442.

(209) Koval, Y.; Geworski, A.; Gieb, K.; Lazareva, I.; Müller, P. Fabrication and Characterization of Glassy Carbon Membranes. *Journal of Vacuum Science & Technology B, Nanotechnology and Microelectronics: Materials, Processing, Measurement, and Phenomena* **2014**, *32* (4), 042001. https://doi.org/10.1116/1.4890008.

(210) Inagaki, M.; Kang, F. Fundamental Science of Carbon Materials. In *Materials Science and Engineering of Carbon: Fundamentals*; 2014; pp 17–217. https://doi.org/10.1016/b978-0-12-800858-4.00002-4.

(211) Wang, X.; Zhang, G. M.; Zhang, Y. L.; Li, F. Y.; Yu, R. C.; Jin, C. Q.; Zou, G. T. Graphitization of Glassy Carbon Prepared under High Temperatures and High Pressures. *Carbon N Y* **2003**, *41* (1), 188–191. https://doi.org/10.1016/S0008-6223(02)00319-6.

(212) Noda, T.; Inagaki, M.; Yamada, S. Glass-like Carbons. *J Non Cryst Solids* **1969**, *1* (4), 285–302. https://doi.org/10.1016/0022-3093(69)90026-X.

(213) *Applications for Glassy Carbon*. SPI Supplies. https://www.2spi.com/catalog/documents/Glassy-Vitreous-Carbon-Info.pdf.

(214) Inagaki, M.; Kang, F. Fundamental Science of Carbon Materials. In *Materials Science and Engineering of Carbon: Fundamentals*; 2014; pp 17–217. https://doi.org/10.1016/b978-0-12-800858-4.00002-4.

(215) Jurkiewicz, K.; Pawlyta, M.; Zygadło, D.; Chrobak, D.; Duber, S.; Wrzalik, R.; Ratuszna, A.; Burian, A. Evolution of Glassy Carbon under Heat Treatment: Correlation Structure–

Mechanical Properties. *J Mater Sci* **2018**, *53* (5), 3509–3523. https://doi.org/10.1007/s10853-017-1753-7.

(216) Wang, X.; Zhang, G. M.; Zhang, Y. L.; Li, F. Y.; Yu, R. C.; Jin, C. Q.; Zou, G. T. Graphitization of Glassy Carbon Prepared under High Temperatures and High Pressures. *Carbon N Y* **2003**, *41* (1), 188–191. https://doi.org/10.1016/S0008-6223(02)00319-6.

(217) Mezzi, A.; Kaciulis, S. Surface Investigation of Carbon Films: From Diamond to Graphite. *Surface and Interface Analysis* **2010**, *42* (6–7), 1082–1084. https://doi.org/10.1002/sia.3348.

(218) Carlson, T. *Photoelectron and Auger Spectroscopy*; Plenum Press: New York, 1975.

(219) Reynaud, C.; Thevenot, F. Porosity Dependence of Mechanical Properties of Porous Sintered SiC. Verification of the Minimum Solid Area Model. *J Mater Sci Lett* **2000**, *19*, 871–874.

(220) Rice, R. W. *Evaluation and Extension of Physical Property-Porosity Models Based on Minimum Solid Area*; 1996; Vol. 31.

(221) Pabst, W.; Gregorová, E. Minimum Solid Area Models for the Effective Properties of Porous Materials - A Refutation. *Ceramics-Silikáty* **2015**, *59* (3), 244–249.

(222) Pitchumani, R.; Karbhari, V. M. Generalized Fluid Flow Model for Ceramic Tape Casting. *Journal of the American Ceramic Society* **1995**, *78* (9), 2497–2503. https://doi.org/10.1111/j.1151-2916.1995.tb08691.x.

(223) Wonisch, A.; Polfer, P.; Kraft, T.; Dellert, A.; Heunisch, A.; Roosen, A. A Comprehensive Simulation Scheme for Tape Casting: From Flow Behavior to Anisotropy Development. *Journal of the American Ceramic Society* **2011**, *94* (7), 2053–2060. https://doi.org/10.1111/j.1551-2916.2010.04358.x.

(224) Chou, Y. T.; Ko, Y. T.; Yan, M. F. Fluid Flow Model for Ceramic Tape Casting. *Journal of the American Ceramic Society* **1987**, *70* (10), C-280-C-282. https://doi.org/10.1111/j.1151-2916.1987.tb04900.x.

(225) Jeffrey, G. B. The Motion of Ellipsoidal Particles Immersed a Viscous Fluid. *Proceedings of the Royal Society of London* **1922**, *102*, 161–179.

(226) Boonyongmaneerat, Y. Mechanical Properties of Partially Sintered Materials. *Materials Science and Engineering A* **2007**, *452–453*, 773–780. https://doi.org/10.1016/j.msea.2006.11.043.

(227) Fan, Z.; Miodownik, A. P.; Tsakiropoulos, P. Microstructural Characterisation of Two Phase Materials. *Materials Science and Technology* **1993**, *9* (12).

(228) Boccaccini, A. R.; Fan, Z. A New Approach for the Young's Modulus-Porosity Correlation of Ceramic Materials. *Ceram Int* **1997**, 239–245.

(229) Povolny, S. J.; Seidel, G. D.; Tallon, C. Numerical Investigation of Thermomechanical Response of Multiscale Porous Ultra-High Temperature Ceramics. *Ceram Int* **2022**. https://doi.org/10.1016/j.ceramint.2022.01.006.

(230) Arato, P.; Besenyei, E.; Kele, A.; Weber, F. Mechanical Properties in the Initial Stage of Sintering. *J Mater Sci* **1995**, *30*, 1863–1871.

(231) Lam, D. C. C.; Lange, F. F.; Evans, A. G. Mechanical Properties of Partially Dense Alumina Produced from Powder Compacts. *Journal of the American Ceramic Society* **1994**.

(232) Jelitto, H.; Schneider, G. A. Fracture Toughness of Porous Materials – Experimental Methods and Data. *Data Brief* **2019**, *23*. https://doi.org/10.1016/j.dib.2019.103709.

(233) Jelitto, H.; Schneider, G. A. A Geometric Model for the Fracture Toughness of Porous Materials. *Acta Mater* **2018**, *151*, 443–453. https://doi.org/10.1016/j.actamat.2018.03.018.

(234) Hong, C.; Zhang, X.; Han, J.; Wang, B. Fabrication and Mechanical Properties of Porous TiB_2 Ceramic. *J Mater Sci* **2006**, *41* (15), 4790–4794. https://doi.org/10.1007/s10853-006-0040-9.

(235) Li, Y.; Li, Q.; Wang, Z.; Huang, S.; Cheng, X. Fabrication of Laminated ZrB_2SiC Ceramics via Tape Casting and Vacuum Hot-Pressing Sintering and Their Mechanical Properties. *Ceram Int* **2015**, *41* (9), 11555–11561.

Supplementary Materials: Chapter 4

S1: EDS mapping of carbon (red) and zirconium (green) of heat-treated PCN-222.

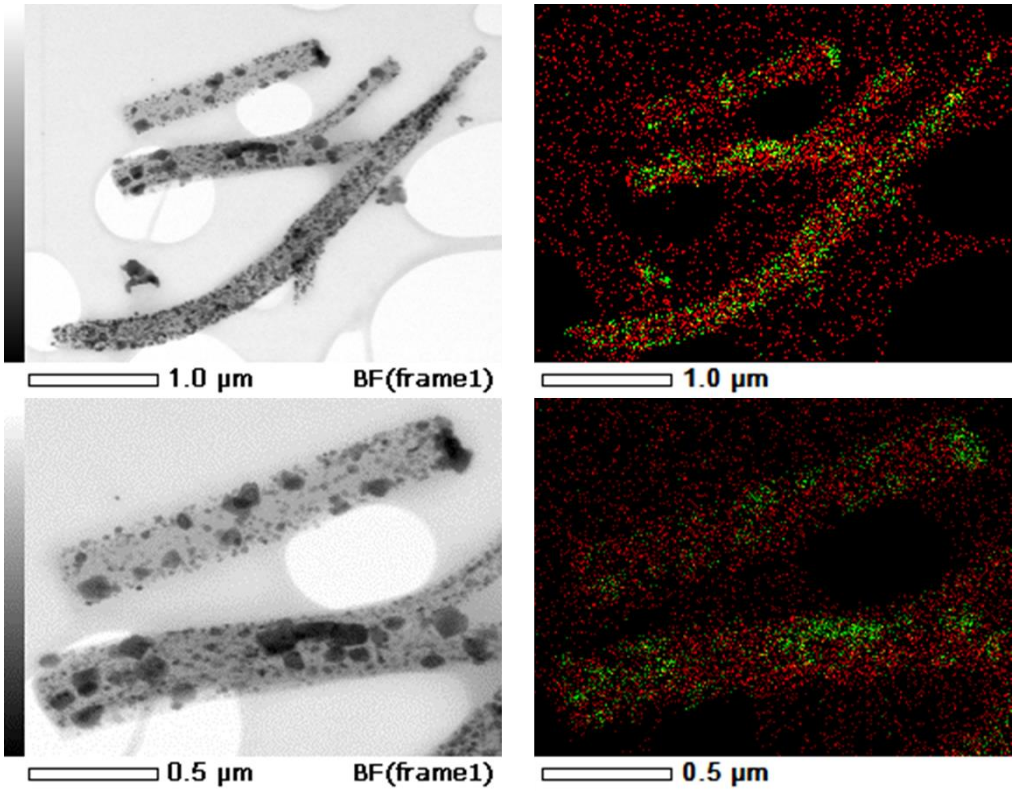

S2: Overall XPS spectra, Cl2p, O1s, and Zr3d spectra for the as-synthesized PCN-222 (A-D) and the heat-treated PCN-222 (E-H).

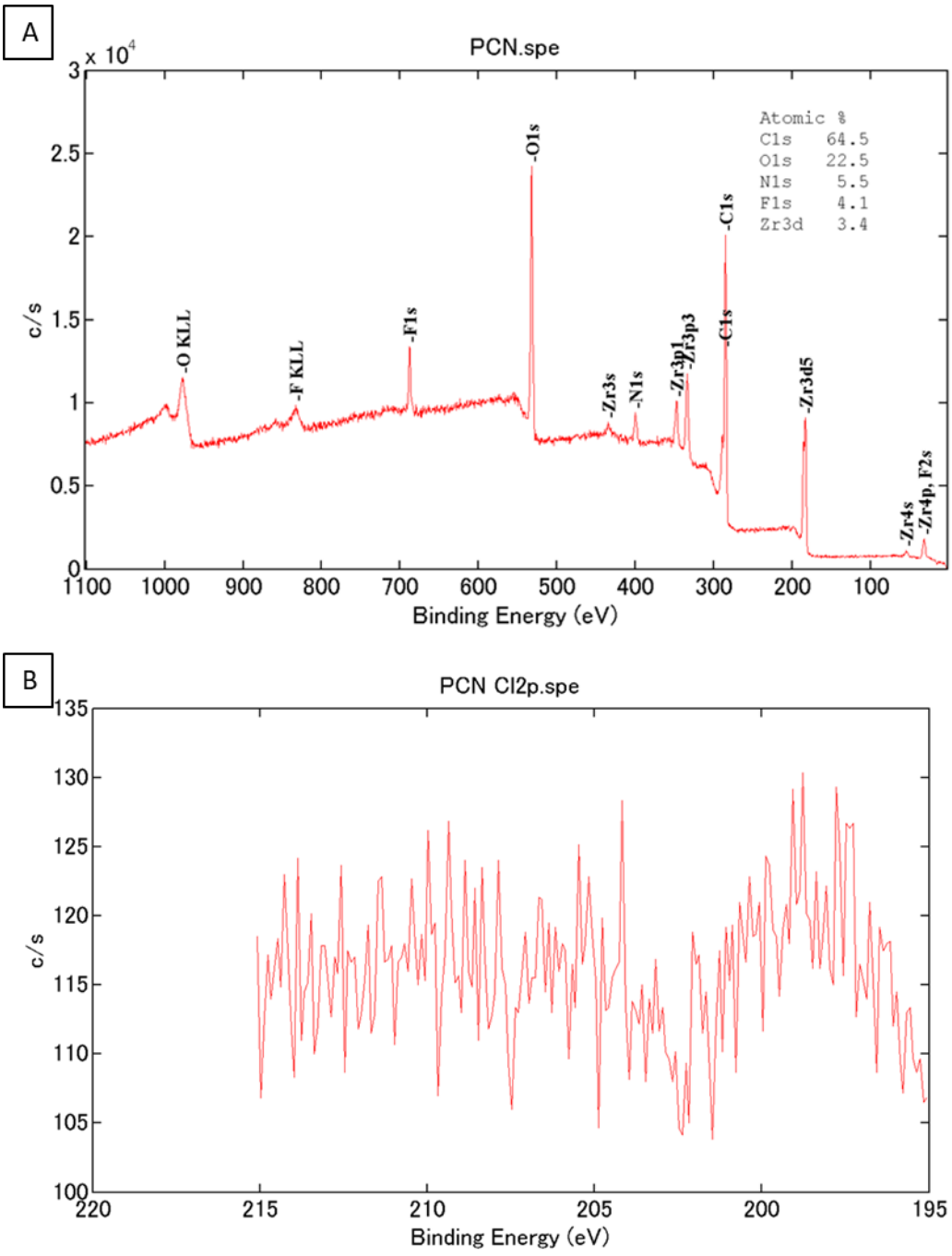

C

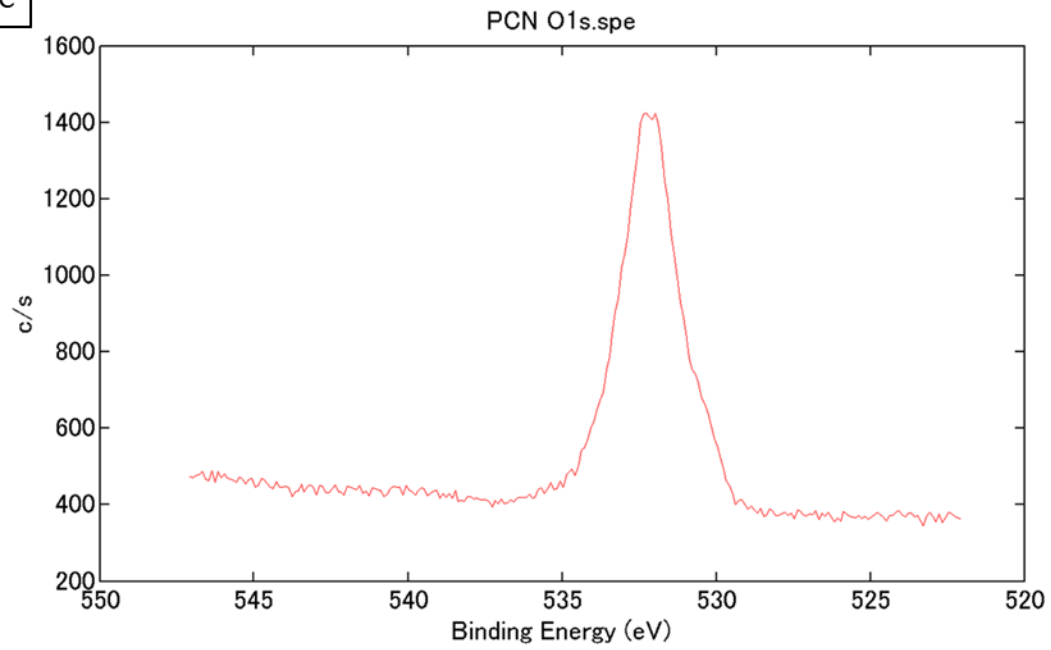
PCN O1s.spe
1600
1400
1200
1000
800
600
400
200
c/s
550
545
540
535
530
525
520
Binding Energy (eV)

D

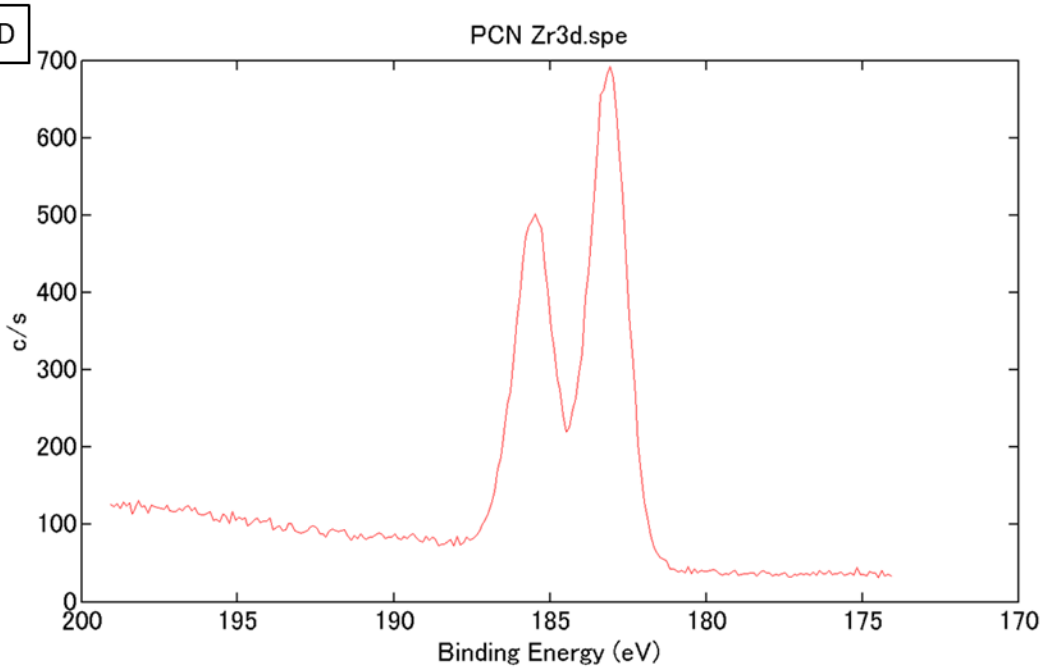
PCN Zr3d.spe
700
600
500
400
300
200
100
0
c/s
200
195
190
185
180
175
170
Binding Energy (eV)

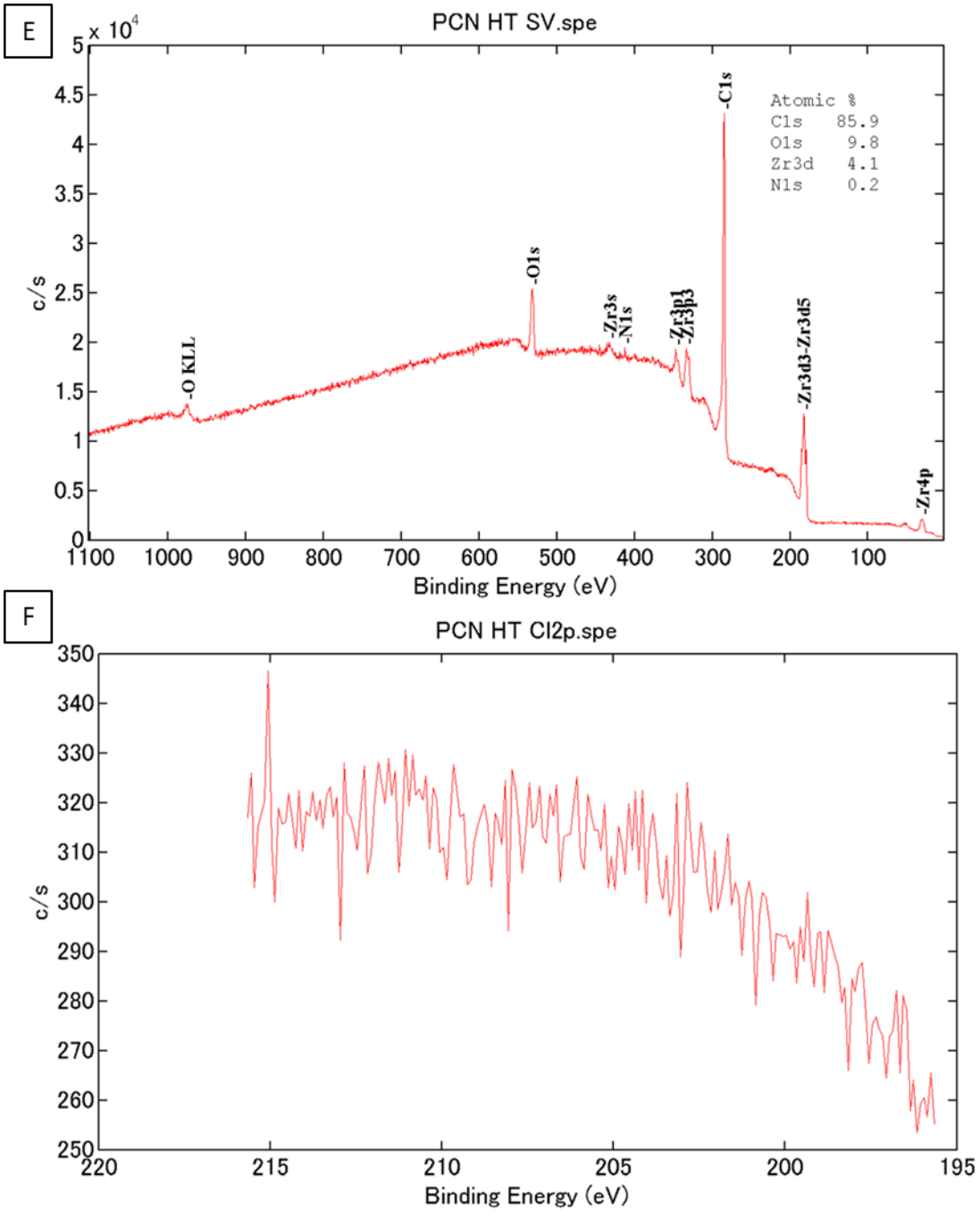
E
PCN HT SV.spe
x 10^4
c/s
Binding Energy (eV)
-O KLL
-O1s
-Zr3s
-N1s
-Zr3p1
-Zr3p3
-C1s
-Zr3d3-Zr3d5
-Zr4p
Atomic %
C1s 85.9
O1s 9.8
Zr3d 4.1
N1s 0.2
F
PCN HT Cl2p.spe
c/s
Binding Energy (eV)

G

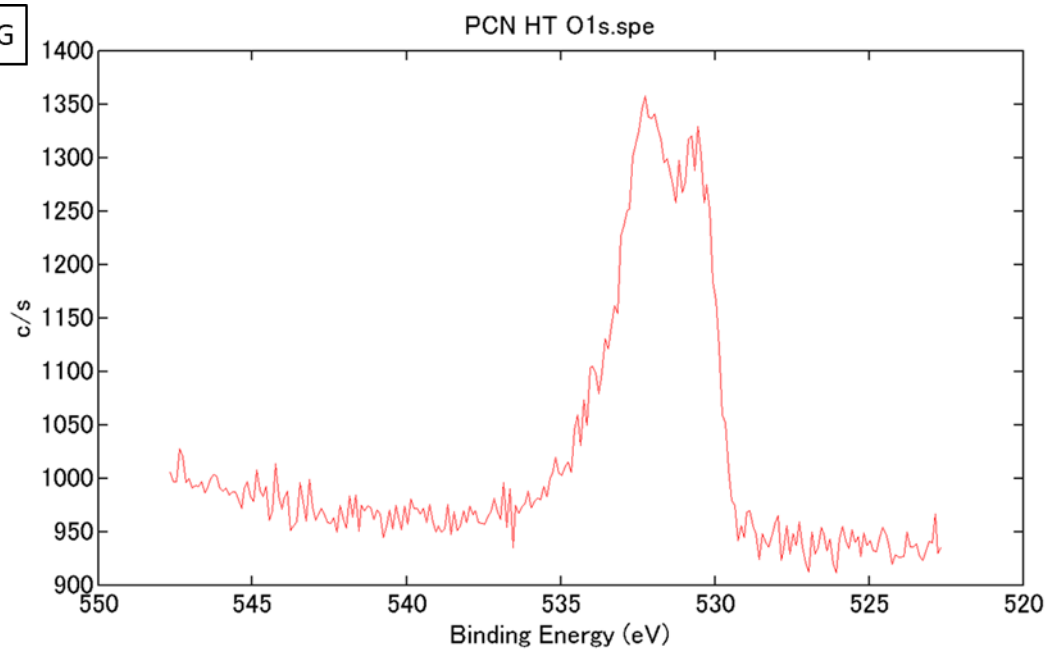
PCN HT O1s.spe
c/s
1400
1350
1300
1250
1200
1150
1100
1050
1000
950
900
550
545
540
535
530
525
520
Binding Energy (eV)

H

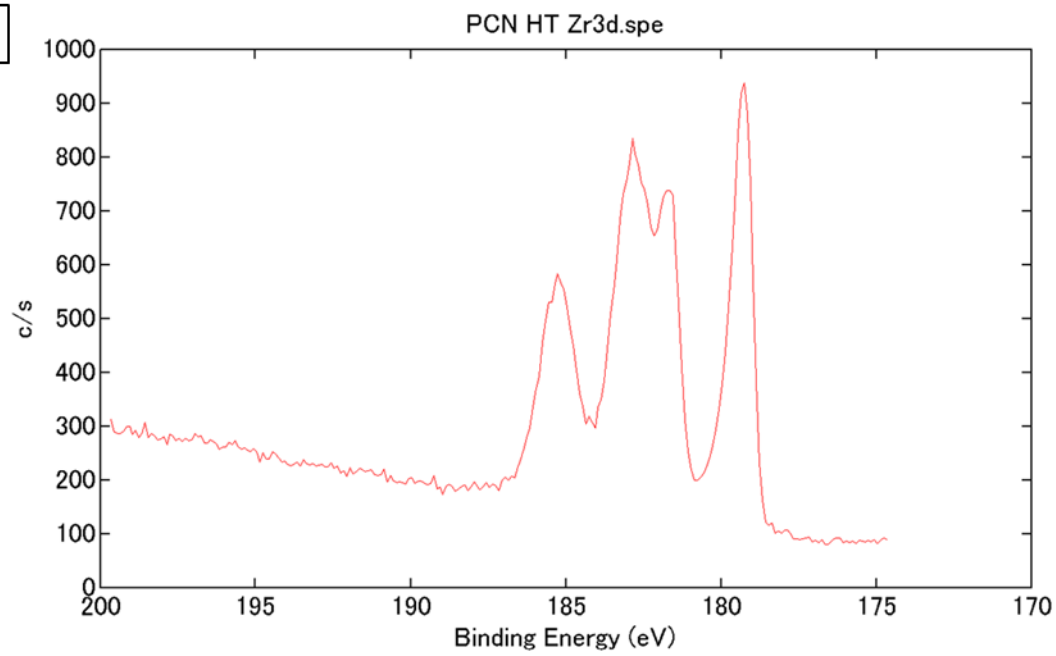
PCN HT Zr3d.spe
c/s
1000
900
800
700
600
500
400
300
200
100
0
200
195
190
185
180
175
170
Binding Energy (eV)

S3: (A-C) TEM image of ZrC crystallite in heat-treated PCN-222, with red circles indicating location of selected area electron diffraction patterns seen in (D-F).

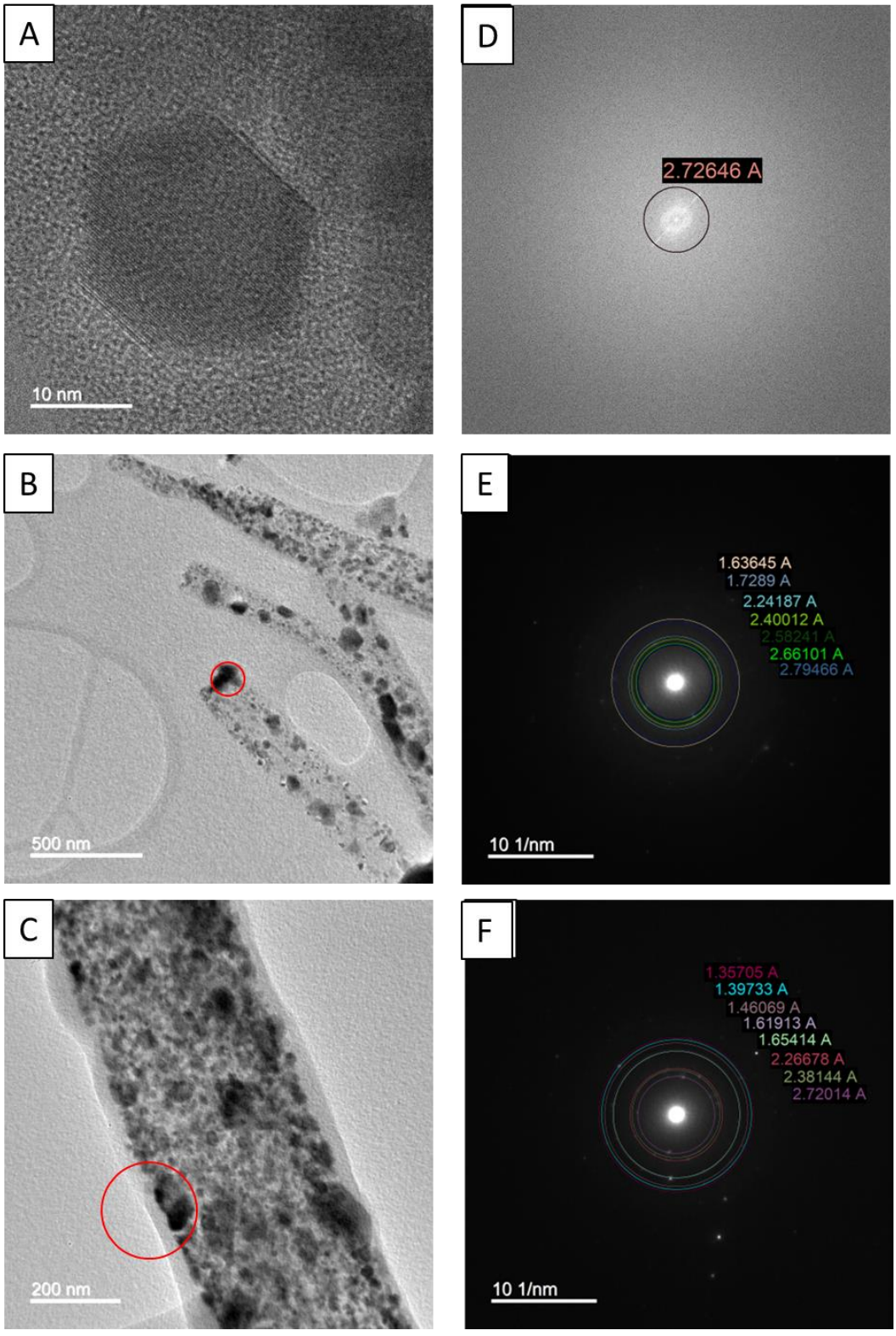

Table S3: Diffraction indexing for crystallites in Figure S3B-D, showing close matches to ZrC.

Pattern	Ring	d spacings (A)	Phase	hkl	d spacings (A)	I/Imax	%diff
Figure S3B	1	2.73	ZrC	1 1 1	2.70	100%	0.8
			Zr hcp	1 0 0	2.80	24%	2.6
Figure S3C	1	2.79	ZrC	1 1 1	2.70	100%	3.3
	2	2.66	ZrC	1 1 1	2.70	100%	1.6
	3	2.58	ZrC	1 1 1	2.70	100%	4.6
	4	2.40	ZrC	2 0 0	2.34	78%	2.5
	5	2.24	ZrC	2 0 0	2.34	78%	4.3
	6	1.73	ZrC	2 2 0	1.66	47%	4.3
	7	1.64	ZrC	2 2 0	1.66	47%	1.2
Figure S3D	1	2.72	ZrC	1 1 1	2.70	100%	0.6
	2	2.38	ZrC	2 0 0	2.34	78%	1.7
	3	2.27	ZrC	2 0 0	2.34	78%	3.2
	4	1.65	ZrC	2 2 0	1.66	47%	0.1
	5	1.62	ZrC	2 2 0	1.66	47%	2.2
	6	1.46	ZrC	3 1 1	1.41	35%	3.4
	7	1.40	ZrC	3 1 1	1.41	35%	1.0
	8	1.36	ZrC	2 2 2	1.35	14%	0.4

List of Author's Achievements

Conference Contributions

- Shirey, Kaitlyn and Tallon, Carolina. "Proof of alignment in tape cast, sintered, porous TiB_2." Nanoscale Characterization and Fabrication Lab Open House. March 15, 2023.
- Shirey, Kaitlyn and Tallon, Carolina. "The role of porosity on pressureless-sintered TiB_2 tapes." Ultra-High Temperature Materials for Extreme Environments Conference. Snowbird, Utah. Poster presentation. June 5-8, 2022.
- Shirey, Kaitlyn and Tallon, Carolina. "Cost-effective suspension formulation for flexible TiB_2 tapes." International Conference and Expo on Advanced Ceramics and Composites. Oral Presentation (Virtual). January 25, 2022.
- Shirey, Kaitlyn, Bonnett, Brittany, Yang, Xiaozhou, Morris, Amanda, and Tallon, Carolina. "Preparation of ZrC embedded glass-like carbon rods via thermal decomposition of metal organic frameworks." Materials Science and Technology Conference. Columbus, Ohio. Oral Presentation. October 20, 2021.

Honors and Awards

- Finalist in the 2023 Torgersen Graduate Student Research Excellence Awards
- Critical Needs funding from the Graduate and Professional Studies Office in the College of Engineering at Virginia Tech
- The Pratt Graduate Fellowship
- Institute for Critical Technology and Applied Sciences (ICTAS) Doctoral Scholar Fellowship (2018-2023)
- New Horizons Graduate Scholar

Publications

- Shirey, Kaitlyn, and Tallon, Carolina. "State of the Art and Emerging Applications of TiB_2." To be submitted to the Journal of the European Ceramic Society, June 2023.
- Shirey, Kaitlyn, and Tallon, Carolina. "Understanding grain and particle alignment in sintered, porous TiB_2 tapes." To be submitted to the Journal of the American Ceramic Society, May 2023.
- Shirey, Kaitlyn, and Tallon, Carolina. (2023). "Cost-effective suspension formulation for flexible TiB_2 tapes." *International Journal of Applied Ceramic Technology*. https://doi.org/10.1111/ijac.14322
- Shirey, Kaitlyn, Bonnett, Brittany, Yang, Morris, Amanda, and Tallon, Carolina. (2023). "Preparation of ZrC embedded glass-like carbon rods via thermal decomposition of metal organic frameworks." *Materialia, 28,* 101716. https://doi.org/10.1016/j.mtla.2023.101716